# STRUCTURE AND PROPERTIES STUDY ON ENERGY MATERIALS: THERMOELECTRIC MATERIAL TETRAHEDRITE AND LITHIUM ION CONDUCTOR LiPON

By

Junchao Li

## A DISSERTATION

Submitted to
Michigan State University
in partial fulfillment of the requirements
for the degree of

Materials Science and Engineering – Doctor of Philosophy

2020

#### **ABSTRACT**

# STRUCTURE AND PROPERTIES STUDY ON ENERGY MATERIALS: THERMOELECTRIC MATERIAL TETRAHEDRITE AND LITHIUM ION CONDUCTOR Lipon

By

#### Junchao Li

Development of efficient energy materials is critical in order to ease the energy demand and reduce our dependence of fossil fuel. Thermoelectric materials are promising due to their capability of generating electrical power by recovering waste heat. The performance of thermoelectric materials is quantified by a dimensionless figure of merit zT, which depends on their properties such as electrical conductivity, Seebeck coefficient and thermal conductivity. Tetrahedrites, a copper antimony sulfosalt mineral, typified by  $Cu_{12-x}M_xSb_4S_{13}$ , where M is a transition metal element such as Ni, Zn, Fe or Mn, have great potential for thermoelectric application due to their relatively high zT (close to 1 at 700 K), earth-abundance, environmental friendliness, favorable electrical properties, and most importantly intrinsic low lattice thermal conductivity (less than 1 W m<sup>-1</sup> K<sup>-1</sup>) in wide temperature.

In addition to energy recovery, reliable energy storage devices are also emerging to relieve the energy demand and improve the efficiency of consuming energy resources. Lithium-ion batteries are known to be reliable and successful electrochemical energy storage devices and appliable in various aspects, including laptops, smartphones and electrical vehicles. Lithium phosphorous oxynitride (LiPON) are widely used as thin-film solid-state electrolytes in Li-ion battery, which is the only demonstrated solid-state electrolyte that is quite stable in direct contact

with Li metal at potentials from 0-5 V. However, the structure of LiPON, the effects of N doping, and the origin of its good electrochemical stability remains inconclusive.

In this thesis, reliable modeling techniques accompanied with experimental tools, are applied to study the thermoelectric material tetrahedrite and the ionic conductor LiPON, in order to study their structural and dynamical properties. Accurate and efficient density-functional theory (DFT) and density-functional tight-binding (DFTB) methods, combined with molecular dynamics (MD) simulations are utilized in order to investigate the structures and properties of these energy materials. The incoherent and coherent atomic dynamics study of tetrahedrite Cu<sub>10.5</sub>NiZn<sub>0.5</sub>Sb<sub>4</sub>S<sub>13</sub> provides the origin of softening upon cooling by investigate the motion of Cu12e at different temperatures. The dynamic structure factors in the longitudinal and transverse direction will also be discussed. The Cu movement of Cu-rich tetrahedrite Cu<sub>14</sub>Sb<sub>4</sub>S<sub>13</sub> is revealed by Cu selfdiffusivity, nuclear density map and "nudged elastic band" (NEB). Moreover, we investigate the effect of simulation cell size and basis sets on the DFT-based MD simulation results using tetrahedrite Cu<sub>10</sub>Zn<sub>2</sub>Sb<sub>4</sub>S<sub>13</sub> thermoelectric as a model material, showing the advantage of larger cell by accessing smaller Q range. In addition, the low-temperature structural properties of Cu<sub>12</sub>Sb<sub>4</sub>S<sub>13</sub> is measured by neutron diffraction, which indicates that no cubic to tetragonal transition occurs at metal-semiconductor transition (MST) temperature. Thermoelectric properties such as Seebeck coefficient, electrical resistivity and electrical thermal conductivity will also be investigated. DFTB method is implemented to study the structure and transport properties of Li<sub>3</sub>PO<sub>4</sub> and LiPON, while the exploration of N doping effect is included. Lastly, the LiPON/Li interphase will be revealed in order to study the origin of electrochemical stability.

Dedicated to Families and friends

#### **ACKNOWLEDGEMENTS**

First and foremost, I would like to thank my advisor Dr. Wei Lai for his generous support throughout my path on pursuing doctorate degree. Over these years, He is not only my research advisor but also a spiritual mentor, with his valuable characteristics of hardworking, patience and intelligence. The most important things I've learned from him is self-motivation and the capability of critical thinking. The weekly research update and presentations in our group help me a lot in terms of oral presentation skill, as well as confidence. I want to show my great appreciation to Dr. Lai again for everything he did these years. I feel so lucky joining our group.

I also want to thank my committee members, Dr. Donald Morelli, Dr. Yue Qi and Dr. Xianglin Ke. Dr. Morelli's energy materials application course and Dr. Qi's computational course helped me a lot and inspired my research path. Dr. Ke, thank you for your valuable advice during our collaboration on thermoelectric materials and my comprehensive exam. Thank you all again for being my committee members.

I would like to acknowledge my former and current colleagues, Rengarajan Shanmugam, Matthew Klenk, Qian Chen, Jin Dai and Yue Jiang. Although it was only half a year working with Raj, he showed a good model as a hardworking PhD candidate. Matt helped me a lot with the computational setup and codes writing when I first joined the group. The discussion between us always kept me motivated and brought me new ideas. Qian and Jin, they are patient, unselfish and optimistic. Although we are working on different material systems, the works you did inspired me on my own research. I wish you will have successful career at MSU and in the future. Yue made a great effort on his experimental work and he is always accommodating. I hope you enjoy your time in our group.

I'm grateful to all my families and friends for their support over these years. Mom and dad, thank you for everything you did throughout the 28 years. Every time I felt frustrated, you always offer encouragement and confidence. Without your unconditional love, I wouldn't make this far. My grandmother, thank you for raising me up and kept me accompanied in my childhood. My aunts and uncles, thank you for your concerns and making me feel warm every time I come back home. You are all the greatest families. I would also like to acknowledge my friends at MSU. We spend many wonderful times together, playing basketball, swimming, traveling, etc. The great times we had, the difficulties we got over, and worthy suggestions you gave, those all provided me motivation on being a better person.

# TABLE OF CONTENTS

LIST OF TABLES	X
LIST OF FIGURES	xi
CHAPTER 1 : Introduction and motivation	1
1.1 Energy crisis	1
1.2 Thermoelectric materials and tetrahedrite Cu <sub>12</sub> Sb <sub>4</sub> S <sub>13</sub>	3
1.2.1 Thermoelectric effect and performance of thermoelectric materials	3
1.2.2 Applications of thermoelectric materials	6
1.2.3 Tetrahedrite Cu <sub>12</sub> Sb <sub>4</sub> S <sub>13</sub>	
1.3 Lithium-ion battery and electrolyte material LiPON	11
1.3.1 Introduction of lithium-ion battery	
1.3.2 Electrolyte material LiPON	
1.4 Modeling techniques on structural and dynamical properties of energy materials	
1.4.1 Introduction to DFT	
1.4.2 Introduction to DFTB	
1.4.3 Other computational techniques	
1.5 Dissertation outline	
low-temperature properties  2.1 Introduction  2.2 Computational and experimental details  2.3 Results and Discussion  2.3.1 Low temperature structure of Cu <sub>12</sub> Sb <sub>4</sub> S <sub>13</sub> 2.3.2 Sb-Cu 12e-Sb interaction  2.3.3 Vibrational Density of States  2.3.4 Thermoelectric properties  2.4 Conclusion	31 32 33 38 40
CHAPTER 3 : Incoherent and coherent atomic dynamics of Cu <sub>10.5</sub> NiZn <sub>0.5</sub> Sb <sub>4</sub> S <sub>13</sub>	
3.1 Introduction	
3.2 Computational and experimental details	
3.3 Results and discussion	
3.3.1 Incoherent atomic dynamics of Cu <sub>10.5</sub> NiZn <sub>0.5</sub> Sb <sub>4</sub> S <sub>13</sub>	
3.3.2 Coherent atomic dynamics of Cu <sub>10.5</sub> NiZn <sub>0.5</sub> Sb <sub>4</sub> S <sub>13</sub>	
3.4 Summary	33
CHAPTER 4 : Mobile Cu movement in Cu-rich tetrahedrite Cu <sub>14</sub> Sb <sub>4</sub> S <sub>13</sub>	55
4.1 Introduction	
4.2 Computational details	

4.3 Results and discussion	57
4.3.1 Lattice parameters	57
4.3.2 Incoherent density correlation and Cu self-diffusivity	58
4.3.3 Cu nuclear density map	
4.3.4 Energy barriers	
4.4 Summary	63
CHAPTER 5: Density-functional theory based molecular dynamics simulation of	tetrahedrite
thermoelectrics: effect of cell size and basis sets	
5.1 Introduction	65
5.2 Computational and experimental details	66
5.3 Results and discussion	
5.3.1 Average structure	67
5.3.2 Lattice parameters	68
5.3.3 Vibrational density of states	
5.3.4 Phonon dispersion.	
5.3.5 EXAFS spectra	
5.3.6 2x2x2 AO Simulation	
5.4 Summary	76
CHAPTER 6: Structure and ionic conduction study on Li <sub>3</sub> PO <sub>4</sub> and LiPON with do	ensity
functional tight binding (DFTB) method	
6.1 Introduction	
6.2 Computational details	
6.2.1 Generation of c-Li <sub>3</sub> PO <sub>4</sub> and c-LiPON models	
6.2.2 Generation of a-Li <sub>3</sub> PO <sub>4</sub> and a-LiPON models	
6.3 Results and discussion.	
6.3.1 Lattice parameters	
6.3.2 Exploration of LiPON structure	
6.3.3 Self-diffusivity of different atomic groups	
6.3.4 Ionic conductivity	
6.4 Summary	
5 · · · · · · · · · · · · · · · · · · ·	
CHAPTER 7: Preliminary study on LiPON/Li interphase	94
7.1 Introduction	
7.2 Computational details	
7.3 Results and discussion.	
7.3.1 Average structure	
7.3.2 Reaction at the interface	
7.3.3 Li charge distribution	
7.3.4 Projected density of states	
7.5.1. 1.10 Journal delibity of button infilmental manners and the second delibity of button infilment	
CHAPTER 8 : Future work and conclusions	101
8.1 Future work	
8.1.1 Further investigation on thermoelectric material tetrahedrite	
8.1.2 Understanding the origin of LiPON/Li interphase	

8.1.3 Exploration in cathode materials	
8.2 Conclusions	
BIBLIOGRAPHY	107

# LIST OF TABLES

Table 2.1:	Atomic parameters in the crystal structure of Cu <sub>12</sub> Sb <sub>4</sub> S <sub>13</sub> at 20 K.	37
Table 2.2:	Atomic parameters in the crystal structure of Cu <sub>12</sub> Sb <sub>4</sub> S <sub>13</sub> at 50 K.	37
Table 2.3:	Atomic parameters in the crystal structure of Cu <sub>12</sub> Sb <sub>4</sub> S <sub>13</sub> at 87.5 K.	37
Table 2.4:	Atomic parameters in the crystal structure of Cu <sub>12</sub> Sb <sub>4</sub> S <sub>13</sub> at 300 K.	37
	Number of rattling and locking Cu 12e, Cu 12e -Sb bond order and bond distance for at different temperatures.	
	Calculated lattice parameters (a, b, c) of c-Li <sub>3</sub> PO <sub>4</sub> and c-LiPON at 300 K comparing tents.	

# LIST OF FIGURES

Figure 1.1: Global energy consumption from 1993 to 2018 with the unit of mtoe (million tonnes oil equivalent) <sup>1</sup>
Figure 1.2: Global energy-related carbon dioxide emissions by source, 1990-2018 <sup>2</sup>
Figure 1.3: Schematic of thermoelectric device showing the direction of charge flow on both cooling and power generation <sup>11</sup>
Figure 1.4: (a) Optimizing $zT$ through carrier concentration tuning. (b) Benefits of reducing $\kappa l$ . 11
Figure 1.5: Crystal structure of tetrahedrite $Cu_{12}Sb_4S_{13}$ with two distinct $Cu$ sites
Figure 1.6: Electronic band structure and density of states of (a) $Cu_{12}Sb_4S_{13}$ and (b) $Cu_{10}Zn_2Sb_4S_{13}^{35}$ .
Figure 1.7: Schematic of working principles of Li <sub>x</sub> C <sub>6</sub> /Li <sub>1-x</sub> CoO <sub>2</sub> Li-ion battery <sup>10</sup>
Figure 1.8: Current electrode materials road map <sup>67</sup>
Figure 1.9: Temperature dependence of ionic conductivity of various electrolyte materials <sup>72</sup> 14
Figure 1.10: Composition diagram with starting materials of $\text{LiO}_{1/2}$ , $\text{LiN}_{1/3}$ , $\text{PO}_{5/2}$ and $\text{PN}_{5/3}$ . Natural and synthetic crystalline materials are labeled as dark (blue) circles, thin-film compositions as light (turquoise) circles, and examples of stable and meta-stables nitride phosphate materials as black square <sup>83</sup>
Figure 1.11: Current-potential curve of a LiPON/Pt half-cell with respect to Li/Li <sup>+</sup> reference <sup>91</sup> . 17
Figure 1.12: Popular computational techniques for different length and time scales
Figure 1.13: The number of DFT citations from 1995 to 2013 <sup>102</sup>
Figure 2.1: Neutron diffraction data for $Cu_{12}Sb_4S_{13}$ at 20, 50, 87.5 and 300 K, synchrontron x-ray data by Nasonova el al. are shown for comparison. No peak splitting can be identified below MST temperature.
Figure 2.2: Neutron diffraction data collected for tetrahedrite sample at $87.5 \text{ K}$ using (a, b) $\text{Cu}_{12}\text{Sb}_4\text{S}_{13}$ and (c,d) $\text{Cu}_{13.2}\text{Sb}_4\text{S}_{13}$ as model structures. Block 1 contains 80% of the data and block 2 has the rest 20%.
Figure 2.3: Neutron diffraction data collected for tetrahedrite sample at (a, b) 20 K, (c, d) at 50 K and (e, f) at 300 K using Cu <sub>12</sub> Sb <sub>4</sub> S <sub>13</sub> structure as model. Block 1 contains 80% of the data and block 2 has the rest 20%

Figure 2.4: Lattice parameters of Cu <sub>12</sub> Sb <sub>4</sub> S <sub>13</sub> obtained by DFT-MD NPT simulation and neutron diffraction refinement. Lattice parameters proposed by Nasonova using synchrontron x-ray are shown here for comparison
Figure 2.5: Schematic of Cu-Sb interaction at 20 K and 300 K (a) and potential energy landscape based on Sb-Cu12e-Sb cluster at (b) 20 K and (c) 300 K
Figure 2.6: Partial vibration density of states (VDOS) of each atomic group for Cu <sub>12</sub> Sb <sub>4</sub> S <sub>13</sub> at different temperatures
Figure 2.7: DOS calculation for Cu <sub>12</sub> Sb <sub>4</sub> S <sub>13</sub> and partial contribution from each atomic group at different temperatures. Fermi energy is marked by dashed line
Figure 2.8: Temperature dependencies of calculated (a) electrical resistivity, (b) Seebeck coefficient and (c) electrical thermal conductivity for Cu <sub>12</sub> Sb <sub>4</sub> S <sub>13</sub> . Experimental data from Nasonova el al. are shown here for comparison.
Figure 3.1: (a)Comparison of VDOS from MD simulation and INS experiment. (b) Partial VDOS for each atom group and total VDOS from MD simulation at 300K
Figure 3.2: Partial VDOS of Cu12e atoms at different temperatures. Shape was fitted to sum of two Lorentzian functions.
Figure 3.3: Potential energy landscape based on Sb-Cu12e-Sb cluster at 50 K (a) and 300 K (b), and correlated VDOS spectra of Cu12e at 50 K (c) and 300 K (d). Cu12e-Sb interaction are shown in (e)
Figure 3.4: Calculated dynamic structure factors based on the momentum correlation function (a) longitudinal and (b) transverse direction.
Figure 4.1: Initial crystal structure of Cu-rich tetrahedrite Cu <sub>14</sub> Sb <sub>4</sub> S <sub>13</sub> with three distinct Cu sites.  Cu24g atoms are displayed as black
Figure 4.2: Cu24g local environment for better visualization
Figure 4.3: Lattice parameters (a, b, c) as function of time in NPT simulation 57
Figure 4.4: Incoherent density correlation for (a) diffusing Cu atoms and (b) vibrating Cu atoms for three small Q values.
Figure 4.5: HWHM ( $\Gamma$ ) as a function of $Q2$ . Red line is fitted to Fickian model and blue line is fitted to Singwi-Sjolander model.
Figure 4.6: Nuclear density may of Cu atom showing the diffusion pathway: (a) $12d - 24g$ path; (b) $12d - 12d$ path; (c) $12e - 24g$ path. Brown atom is Sb and yellow is S. Isosurface level of 0.12 Å <sup>-3</sup>

Figure 4.7: Diffusion paths schematic of (a) $24g - 12d$ and (b) $24g - 12e$ extracted from the actual MD trajectory and migration energy barriers of (c) $24g - 12d$ and (d) $24g - 12e$ from NEB calculations.
Figure 5.1: Average structure after 1x1x1 PW NVE simulation showing the crystal structure of Cu <sub>10</sub> Zn <sub>2</sub> Sb <sub>4</sub> S <sub>13</sub>
Figure 5.2: Lattice parameters (a, b, c) of (a) 1x1x1 PW and (b) 1x1x1 AO cell as a function of time in NPT simulation
Figure 5.3: Partial and total vibrational density of states (VDOS) of each atom group (a-e: Cu12e, Cu12d, Zn12d, Sb, and S; f: total) for three simulations (1x1x1 PW, 1x1x1 AO, and 2x2x2 AO).
Figure 5.4: Heat capacity per atom for three simulations (1x1x1 PW, 1x1x1 AO, and 2x2x2 AO). Experimental data from Lu et al. <sup>7</sup> and Lara-Curzio et al. <sup>33</sup> are also shown for comparison.
Figure 5.5: Longitudinal phonon dispersion for (a) Q=0.60 A <sup>-1</sup> , (c) Q=0.84 A <sup>-1</sup> and transverse phonon dispersion for (b) Q=0.60 A <sup>-1</sup> , (d) Q=0.84 A <sup>-1</sup>
Figure 5.6: k²-weighted Cu EXAFS spectrum obtained by experiment (black circle) and simulations (solid lines)
Figure 5.7: Longitudinal (a) and transverse (b) response of the momentum correlation. (c) Dispersion of longitudinal (L) and transverse (T) sound modes. Peak energy for each Q value (red dots: longitudinal; blue dots: transverse) and their linear regression have been shown 75
Figure 5.8: Longitudinal (a) and transverse (b) response of the coherent velocity correlation. Longitudinal acoustic (LA) and quasi-localized (QL) modes are marked in a. The dotted lines have the same energy between a and b
Figure 6.1: Flowchart of generation of amorphous a-Li <sub>3</sub> PO <sub>4</sub> and a-LiPON
Figure 6.2: Schematic of a-LiPON structure at 1200 K from NVT run
Figure 6.3: Bond order as a function of bond distance of P-N, P-O and Li-X pairs
Figure 6.4: ELF maps of (a) Li-N <sub>a</sub> , (b) Li-N <sub>d</sub> and (c) Li-O units (isosurface level of 0.82) 84
Figure 6.5: Statistical results of Li coordination number around N <sub>a</sub> , N <sub>d</sub> and O
Figure 6.6: An example of $\Gamma$ as a function of $Q^2$ in Li diffusing at 1200 K for a-LiPON 85
Figure 6.7: <i>IQ</i> , <i>t</i> of P and O for c-Li <sub>3</sub> PO <sub>4</sub> and c-LiPON at 1400 K and 1500 K
Figure 6.8: Self-diffusivity of P/O/N atomic groups from Li <sub>3</sub> PO <sub>4</sub> and LiPON as a function of temperature.

Figure 6.9: Li self-diffusivity of various structures as a function of temperature comparing to experimental results.	89
Figure 6.10: Residence time (a) and jump length (b) of Li diffusion.	89
Figure 6.11: (a) Time and (b) frequency domain for the transverse component of coherent chargeurent density function for three smallest Q at 1400 K for a-LiPON	_
Figure 6.12: Calculated ionic conductivity of various structures as a function of temperature comparing to experimental data	92
Figure 7.1: Initial supercell of LiPON/Li interface.	95
Figure 7.2: Average structure over 10 to 80 ps during the NVT run.	96
Figure 7.3: Snapshots of LiPON/Li interphase at (a) 10 ps, (b) 20 ps and (c) 80 ps	97
Figure 7.4: Variation of Li charge from DDEC charge calculation along the c axis	98
Figure 7.5: (a) A snapshot from MD at 20 ps with 3 selected layers (thickness of 6 Å) and two chosen Li atoms from metallic Li phase. (b) Projected density of states at selected layers and atoms. Fermi energy level is located at zero energy.	

#### **CHAPTER 1: Introduction and motivation**

## 1.1 Energy crisis

Energy crisis is a global issue in the recent decades due to the decreasing supply and increasing demand of fossil fuels. According to the BP Statistical Review of World Energy Report<sup>1</sup>, the overall energy consumption keeps increasing for the past years, as shown in Figure 1.1, due to the express industrial development and robust global economy. It can be noticed from the recent 2018 data that the non-renewable energy sources such as natural gas, coal and oil, were still playing an important role in the energy demand, while the application of renewable energy resources contributed only 9.5% to the overall energy consumption, which was still limited and inadequate.

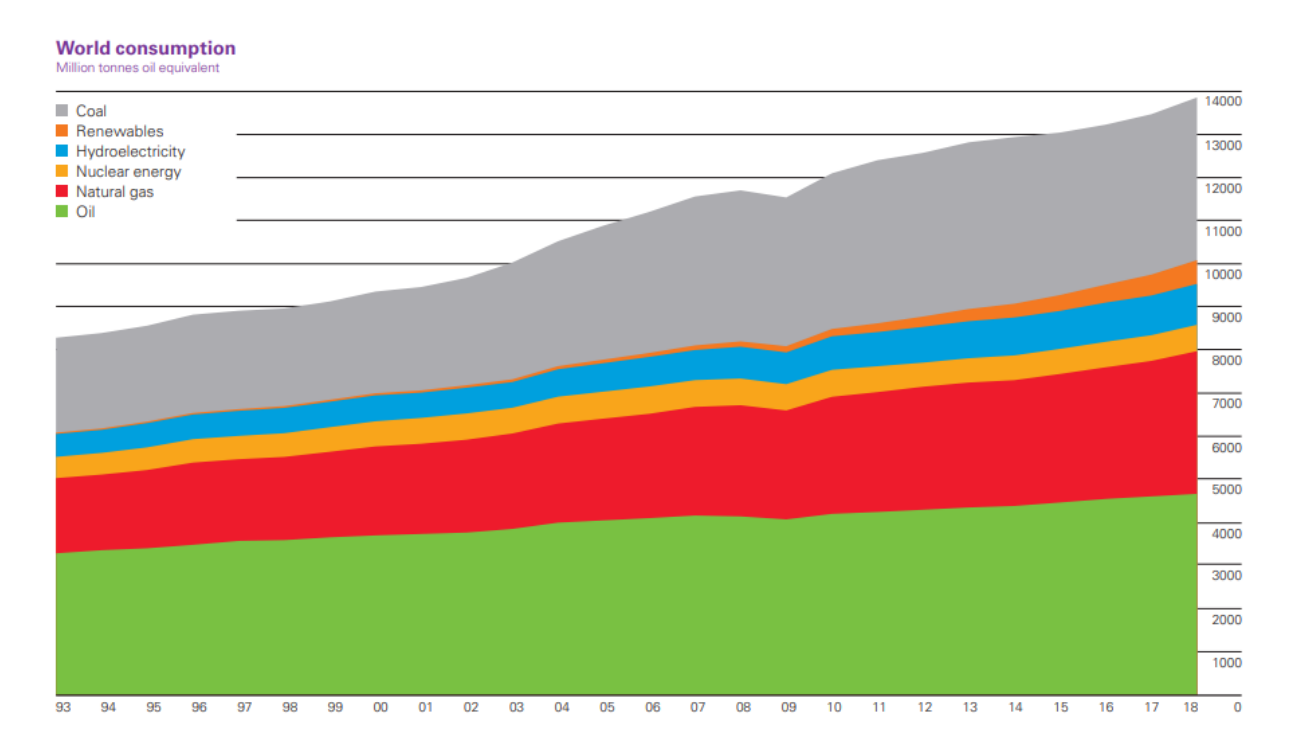


Figure 1.1: Global energy consumption from 1993 to 2018 with the unit of mtoe (million tonnes oil equivalent)<sup>1</sup>.

In addition, driven by the higher energy demand, the energy-related CO<sub>2</sub> emission has continually increased over the past 20 years and reaches a historic high of 33.1 Gt in 2018 as revealed in Figure 1.2<sup>2-3</sup>. The increase of CO<sub>2</sub> content in the atmosphere have been accused to be one of the main reasons of the global climate change and thus lead to numbers of negative effects such as global warming<sup>4-7</sup>.

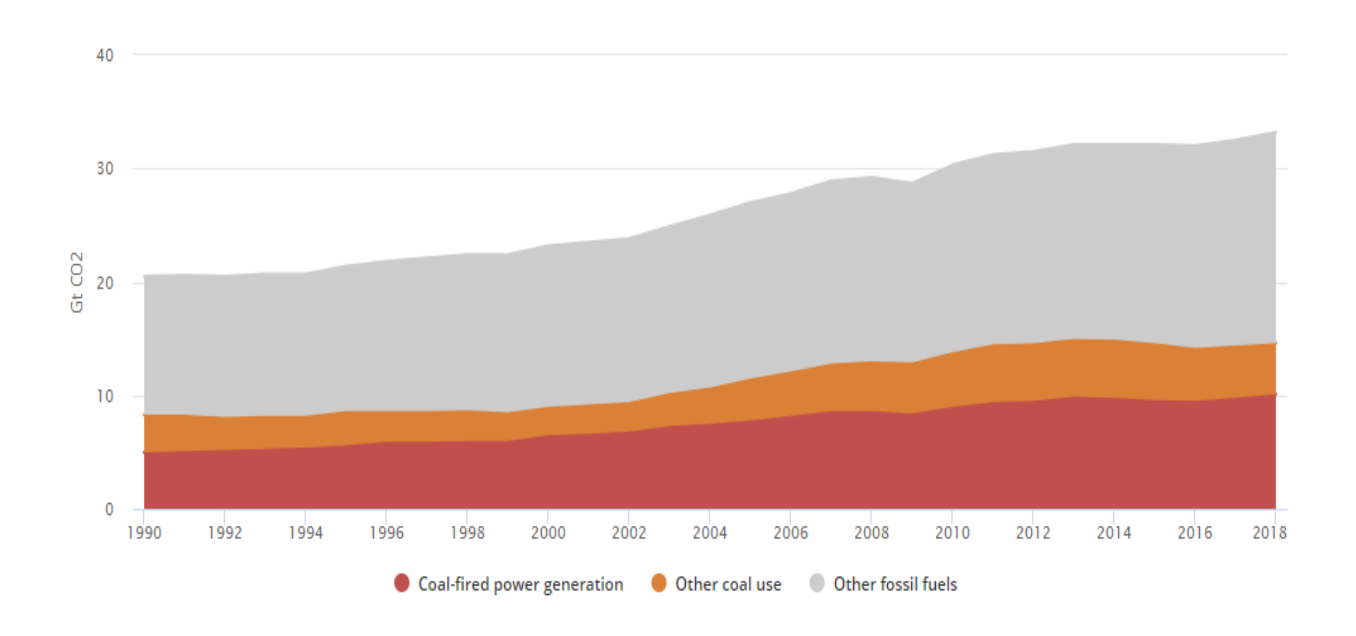


Figure 1.2: Global energy-related carbon dioxide emissions by source, 1990-2018<sup>2</sup>.

The causes of the energy crisis are complex and can be summarized as overconsumption of natural resources, overpopulation, undeveloped infrastructures, unexplored renewable energy options, waste of energy, etc. Considering the enormous amount of waste energy, recovery of those can reduce our energy consumption and improve the energy efficiency. According to statistical analysis from Forman et al.<sup>8</sup>, about 72% of the energy consumed from primary energy sources were wasted as rejected energy, mainly in the form of heat, while thermoelectric can help to recover those waste heat by converting thermal energy to electrical energy. Another solution is moving towards renewable resources. However, the renewable resources, such as solar energy,

wind power and tide power, are intermittent, limiting their large-scale application. Thus, energy storage devices are necessary to store the excess energy. Lithium-ion battery is currently one of the most successful and reliable energy storage devices, attracting many research interests<sup>10</sup>. In this thesis, two promising energy materials, tetrahedrite Cu<sub>12</sub>Sb<sub>4</sub>S<sub>13</sub> as thermoelectric and Lithium phosphorous oxynitride (LiPON) as solid-state electrolyte for Li-ion battery, will be discussed.

# 1.2 Thermoelectric materials and tetrahedrite Cu<sub>12</sub>Sb<sub>4</sub>S<sub>13</sub>

One effective way to ease the energy demand and reduce our dependence of fossil fuel, is to utilize the huge amount of unused waste heat and convert them to electrical energy. Thermoelectric materials are promising due to their ability of direction conversion between thermal and electrical energy, which can be used to recover waste heat or solid-state coolers<sup>11-13</sup>. It has been reported that there are 191 million vehicles in US, dissipating 66% of their consumed energy as wasted heat emission, producing about 36 TWh of waste process heat per year<sup>14</sup>. Considering the enormous wasted heats not only from automobiles, but also from industrial operations, human activities, etc., researchers are throwing their efforts to find high-efficient and reliable thermoelectric materials.

### 1.2.1 Thermoelectric effect and performance of thermoelectric materials

Thermoelectric effect is known as the direct conversion between temperature difference and electric voltage<sup>15</sup>. The phenomenon that thermoelectric devices can convert thermal energy into electrical power is known as "Seebeck effect", and was discovered in 1821 by Thomas Seeback<sup>16</sup>, while the reverse of the phenomenon is known as "Peltier effect" and was proposed in 1834<sup>17</sup>. Figure 1.3 shows the schematic of thermoelectric device which is the application of thermoelectric effect. Generally thermoelectric device contains a lot of thermoelectric couples wired electrically in series and thermally in parallel, while each of the couple consists of an n-type

(negative thermalpower and electron carriers) and a p-type (positive thermalpower and hole carriers) semiconductor. In the power generator case, the temperature difference ( $\Delta T$ ) provides the voltage (V) due to the Seebeck effect ( $V = S\Delta T$ ), where S is the Seebeck coefficient, and thus drives the electrical current and generates power output. In the cooling mode, the electrical current (I) supplied by external power source leads to a heat flow (Q) from top to bottom because of the Peltier effect (Q = STI) and thus cools the top panel<sup>11, 18</sup>.

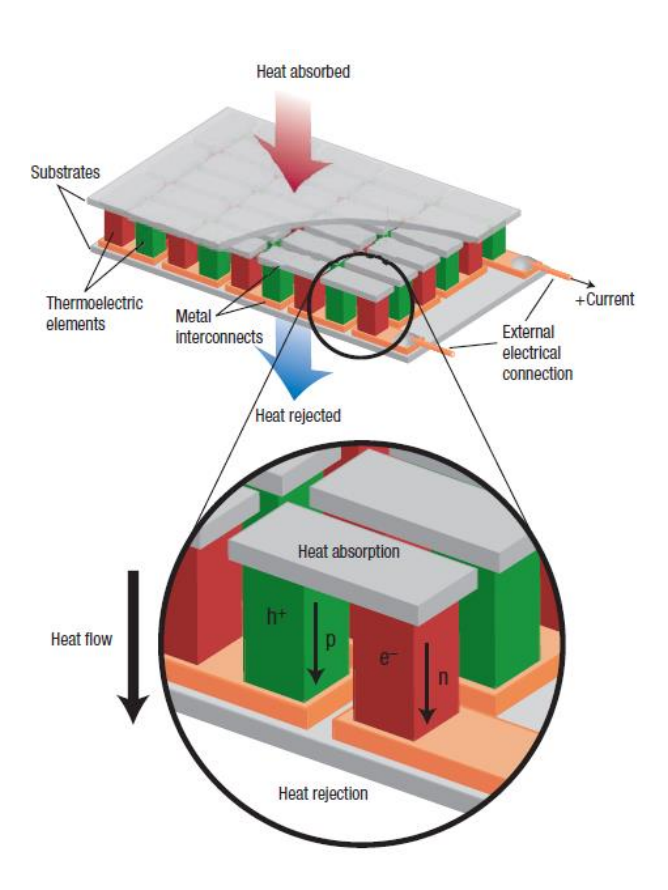


Figure 1.3: Schematic of thermoelectric device showing the direction of charge flow on both cooling and power generation<sup>11</sup>.

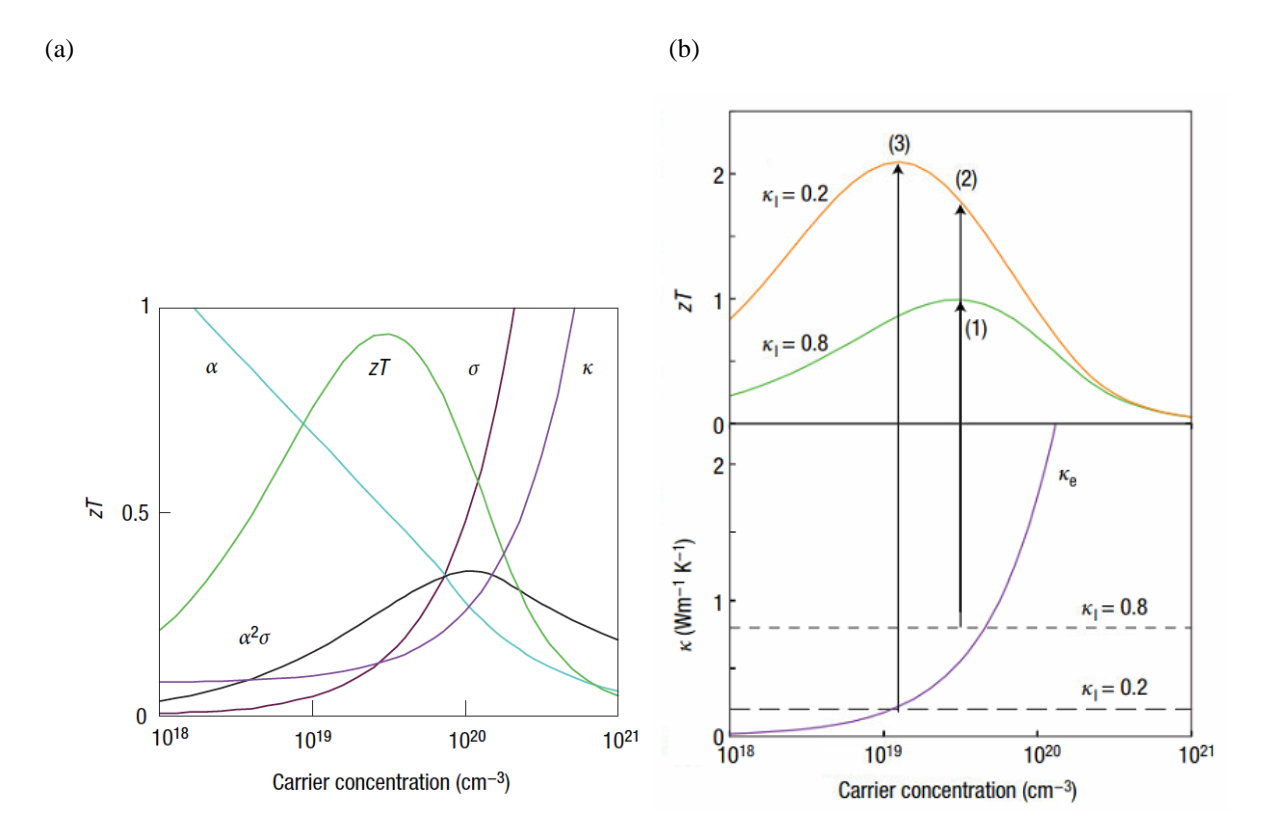


Figure 1.4: (a) Optimizing zT through carrier concentration tuning. (b) Benefits of reducing  $\kappa_l$ . 11

The performance of thermoelectric materials is quantified by a dimensionless figure of merit:

$$zT = \frac{S^2 \sigma T}{\kappa},\tag{1}$$

where  $\sigma$  the electrical conductivity, T the absolute temperature, and  $\kappa$  the thermal conductivity. Thermoelectric materials such as SnSe<sup>19</sup> and PbTe<sup>20</sup> could reach zT at or near the commercial threshold value of 2.5 at high temperatures, enabling the their application in the recovery of waste heat. Figure 1.4 illustrates the relationship between zT and these parameters with carrier concentration tuning. Figure 1.4(a) shows that the peak of zT locates between  $10^{19}$  to  $10^{20}$  carrier/cm<sup>3</sup>, representing heavily doped semiconductor. It can be noted that Seebeck coefficient S ( $\alpha$  in the referred figure) and electrical conductivity  $\sigma$  are inversely related. Moreover, low thermal

conductivity is necessary for thermoelectrics from zT equation. Thermal conductivity  $\kappa$  has two components, electronic thermal conductivity  $\kappa_e$  and lattice thermal conductivity  $\kappa_l$ . However,  $\kappa_e$  and  $\sigma$  are correlated by the Wiedemann-Franz law:

$$\kappa_e = L\sigma T = ne\mu LT,\tag{2}$$

where L is the Lorenz factor with 2.4 x  $10^{-8}$  J<sup>2</sup> K<sup>-2</sup> C<sup>-2</sup> for free electron. This equation suggests that simply increasing  $\sigma$  comes with the increase of  $\kappa_e$  and usually decrease of thermal power<sup>9</sup>. In terms of  $\kappa_l$ , Figure 4(b) shows the benefits of having a low  $\kappa_l$ , where point (1) is the optimized zT with  $\kappa_l = 0.8$  W m<sup>-1</sup> K<sup>-1</sup> and  $\kappa_e$  that is a function of carrier concentration for a model materials Bi<sub>2</sub>Te<sub>3</sub>. If we reduce  $\kappa_l$  to 0.2 W m<sup>-1</sup> K<sup>-1</sup>, zT will increase to point (2) while keeping  $\kappa_e$  unchanged. Furthermore, reducing  $\kappa_e$  by decreasing carrier concentration can reoptimized the value of zT and reach the maximum at point (3)<sup>11</sup>. Considering all the relations and conflicts among these parameters, a concept named "phonon-glass electron-crystal" (PGEC) had been introduced by Slack<sup>21</sup>, suggesting that the ideal thermoelectrics require a rather unusual material: a low lattice thermal conductivity as glass, and a high electrical conductivity as crystal.

## 1.2.2 Applications of thermoelectric materials

Advantages of using solid-state thermoelectric materials include compactness, quietness (no moving parts inside), and localized heating and cooling <sup>18</sup>. It has been mentioned above that thermoelectric materials have power generation mode and cooling mode, accompanied with considerable efficiency, thus the applications of thermoelectric materials can be everywhere in either industry or personal lives.

In terms of power generation, automobiles could be one of the main applications of thermoelectric materials since a lot of waste heat are generated during the exhaust of vehicles. By converting the waste heat into electrical energy using thermoelectrics, the efficiency of fuel can be improved and thus reduce the emission of greenhouse gases<sup>22-23</sup>. Furthermore, in the field of power-generating plants, about 67% of its available energy are wasted during the electrical production, while in manufacturing industries, about 33% of their energy are rejected to the atmosphere in the form of heat. These waste thermal energy are equivalent to the energy generated by more than 1 billion barrels of oil<sup>24-25</sup>. In these aspects, thermoelectrics have great potentials to recover the waste heat and reproduce enormous amounts of electrical power. In addition, thermoelectrics with high zT value can be applied in the case of converting solar thermal energy and replacing the currently used dynamic converter<sup>26</sup>.

Cooling applications of thermoelectrics are also emerging and can be widely used in different areas<sup>11</sup>. For instance, thermoelectrics cooling devices can be commercialized as portable refrigerator, beverage can cooler and picnic basket in the civil market<sup>27-29</sup>. Moreover, electronic devices like PC processors or cell phones generate a large amount of heat while stable performance of these microelectronics requires a relatively low temperature. In these cases, thermoelectric cooler attracts great attention due to their small size and quietness<sup>30</sup>. Besides, there has been great interests in automobile cooling applications, medical applications, air-conditioning applications and industrial temperature control applications of thermoelectric coolers<sup>31-33</sup>.

#### 1.2.3 Tetrahedrite Cu<sub>12</sub>Sb<sub>4</sub>S<sub>13</sub>

Having the background of the intrinsic relationships between thermoelectric properties, it's obvious that low thermal conductivity is critical for thermoelectric materials performance and thus offer the guideline of research and selection of optimal materials. Tetrahedrites, the copper antimony sulfosalt mineral, typified by Cu<sub>12-x</sub>M<sub>x</sub>Sb<sub>4</sub>S<sub>13</sub>, where M is a transition metal element such as Ni, Zn, Fe or Mn, have the potential for thermoelectric application due to their earthabundance, environmental friendliness, favorable electrical properties, and most importantly

intrinsic low lattice thermal conductivity (less than 1 W m<sup>-1</sup> K<sup>-1</sup>) in wide temperature range<sup>34-36</sup>. Lu et al reported Zn-doped tetrahedrite  $Cu_{12-x}Zn_xSb_4S_{13}$  reach low  $\kappa_l$  (< 0.5 W m<sup>-1</sup> K<sup>-1</sup>) close to the "minimal" thermal conductivity where the phonon mean free path equals to the interatomic spacing, and also obtain a high zT value ~ 1 at 720 K<sup>35</sup>.

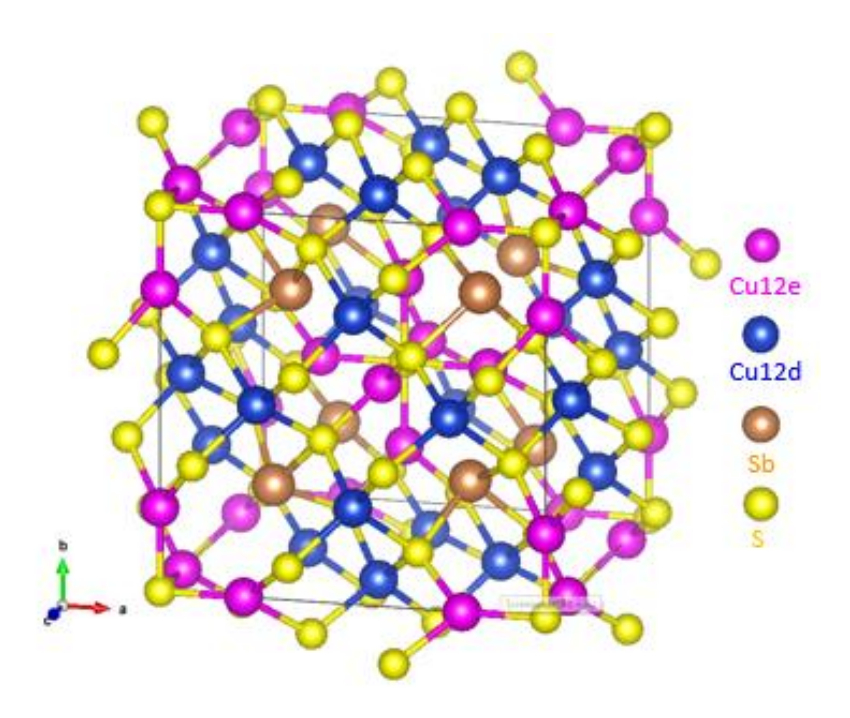


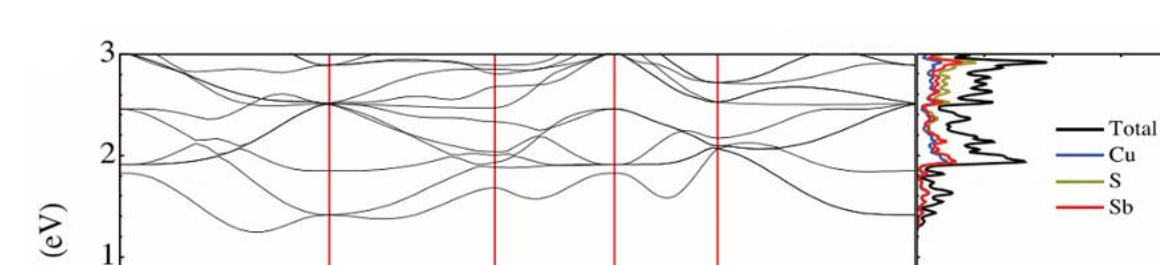
Figure 1.5: Crystal structure of tetrahedrite Cu<sub>12</sub>Sb<sub>4</sub>S<sub>13</sub> with two distinct Cu sites.

Crystal structure of tetrahedrite  $Cu_{12}Sb_4S_{13}$ , a body-centered cubic structure with  $\overline{14}3$  symmetry, has been revealed in Figure 1.5 by the software VESTA<sup>37</sup>. Two distinct Cu sites, identified as  $Cu_{12}d$  and  $Cu_{12}e$ , two S sites,  $S_24g$  and  $S_2a$ , and one Sb site,  $S_2b_3e$ , are the components in the system.  $Cu_{12}d$  atoms are surrounded by four  $S_24g$  atoms with tetrahedra coordination, while  $Cu_{12}e$  atoms coordinated by two  $S_24g$  atoms and one  $S_2a$  atom and form a triangular planar coordination, and also bonded to two Sb atoms and form a  $S_2b[Cu_{3}]S_3e$  trigonal bipyramid. All the transition metal will take the  $Cu_{12}d$  sites. Each  $S_24g$  is coordinated to two  $S_3e$  atom, whereas each  $S_3e$  is bonded to six  $S_3e$   $S_3e$ 

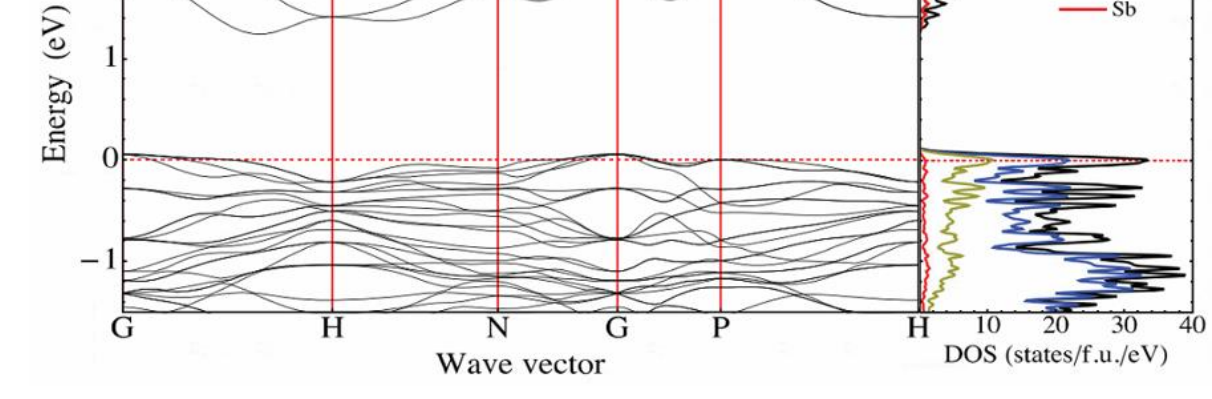
atoms in octahedral coordination. For the Sb site, each Sb8c is coordinated with three S24g atoms and three Cu12e atoms.

The origin of low lattice thermal conductivity is strongly related to the structure of tetrahedrite. The temperature dependent single crystal XRD results performed by Pfitzner et al.<sup>38</sup> indicated a large anharmonic displacement of Cu12e atom perpendicular to the plane of coordinating S atoms. Detailed study on the bonding environment, Cu12e out-of-plane movement and Sb lone pair was carried out by Lai et al.<sup>39</sup> by first-principle simulation and synchrotron diffraction experiments, and linked the anharmonic rattling to the local bonding asymmetry and thus leaded to low thermal conductivity.

Electronic behaviors of tetrahedrite is attracting many researchers. Lu et al.  $^{35}$  calculated the band structure and density of states of  $Cu_{12}Sb_4S_{13}$  and  $Cu_{10}Zn_2Sb_4S_{13}$  using density-functional theory (DFT), as shown in Figure 1.6. Results suggested that  $Cu_{12}Sb_4S_{13}$  is metal-like structure, with Fermi energy level located near a sharp perk at top of valence band, while a semiconducting bandgap of  $\sim 1.1$  eV can be identified. The valence bands are primarily formed by hybridization of S 3p and Cu 3d orbitals. When Zn was doped into the structure as  $Cu_{10}Zn_2Sb_4S_{13}$ , the Fermi energy level was pushed towards the gap. Hence, the Zn-doped tetrahedrite behaved as a true semiconductor, as shown in Figure 1.6 (b). Followed by this work, many researchers applied similar method on doping or substituting tetrahedrite in order to adjust the electronic properties  $^{40}$ 



(a)



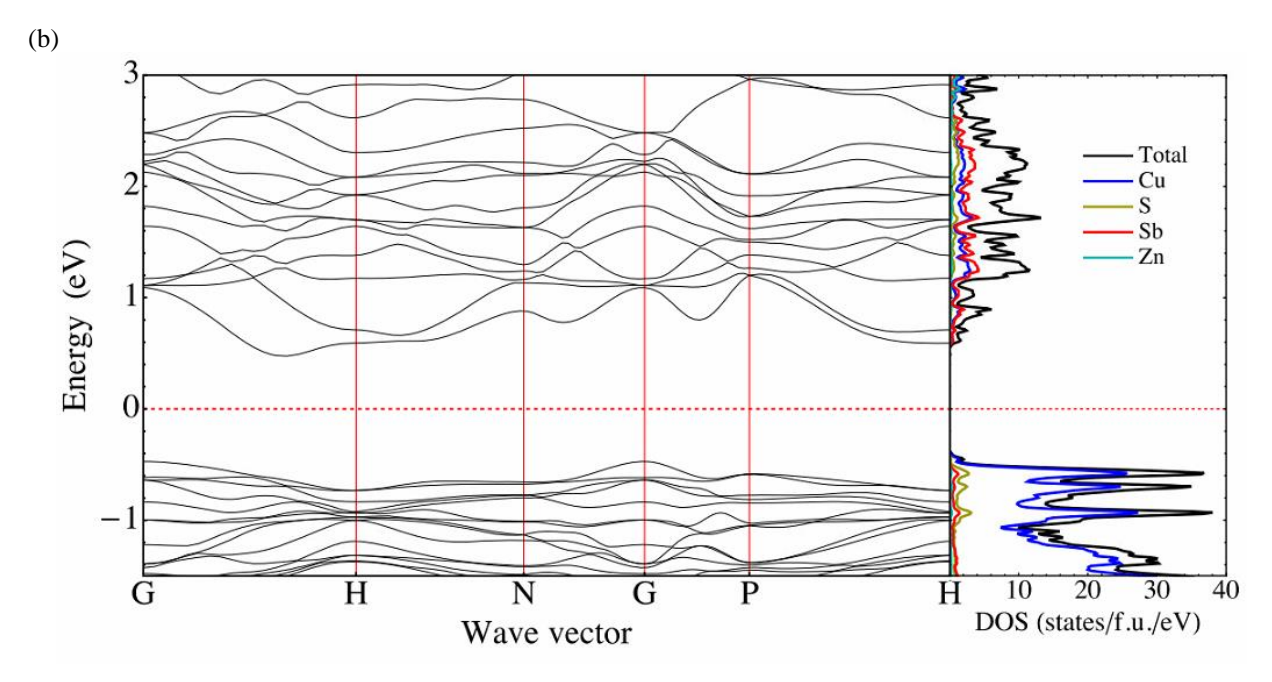


Figure 1.6: Electronic band structure and density of states of (a)  $Cu_{12}Sb_4S_{13}$  and (b)  $Cu_{10}Zn_2Sb_4S_{13}^{35}$ .

Besides the Zn dopants, doping effects for various transition metal such as Mn, Fe, Co and Ni haven been studied over these years  $^{45-46}$ . Appropriate dopants can not only adjust the electronic properties but also enhance the figure of merit, zT. One of the highest zT value (zT=1 at 720 K)

was achieved by Lu et al.<sup>34</sup> by co-doping Ni and Zn into tetrahedrite. Recently, substitution on Sb site by other elements, such as Te and Bi, has also been studied, with significant improvement to the performance of thermoelectrics<sup>47-49</sup>.

Although there are a lot of researches in the field of tetrahedrites including enhancement of thermoelectric performance<sup>34, 36, 50</sup>, electronic properties<sup>40-44</sup>, different synthesis methods<sup>51-53</sup>, etc., there are still plenty of unknowns and uncertainties remained such as the dynamic properties, the Cu-rich tetrahedrite system, and the unique low-temperature behaviors, which will be discussed in detail in Chapter 2, 3, 4 and 5 in this thesis.

## 1.3 Lithium-ion battery and electrolyte material LiPON

# 1.3.1 Introduction of lithium-ion battery

Recalled the energy crisis we discussed above, besides the help from thermoelectrics, renewable energy sources such as solar energy<sup>54-56</sup>, wind power<sup>57-59</sup> and bioenergy<sup>60-62</sup> are making great contributions. However, one issue which cannot be ignored is the mismatch between excess energy generation and energy consumption. Therefore, reliable energy storage devices are emerging to relieve the energy demand and improve the efficiency of consuming energy resources. Lithium-ion batteries are known to be reliable and successful electrochemical energy storage devices and can found everywhere in our daily lives, including laptops, smartphones and electrical vehicles.

The general working principles of Li-ion batteries are shown in Figure 1.7 using Li<sub>x</sub>C<sub>6</sub>/Li<sub>1-x</sub>CoO<sub>2</sub> cell as an example. A Li-ion battery is composed of three essential parts, cathode (positive electrode), anode (negative electrode) and electrolyte (separator). During the charging process, lithium ions shuttle from the cathode to the anode through the electrolyte while the electrons move

from anode to cathode through external circuit simultaneously. And the reverse process occurs when discharging.

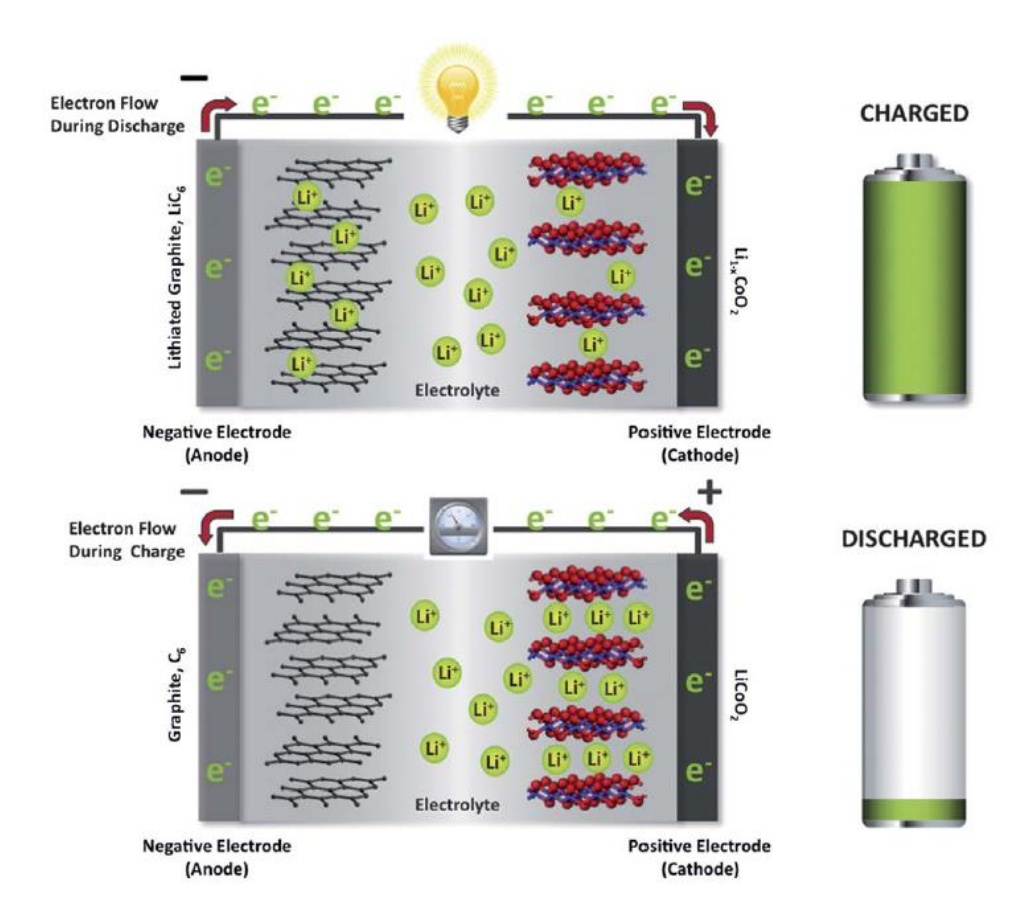


Figure 1.7: Schematic of working principles of  $\text{Li}_x\text{C}_6/\text{Li}_{1-x}\text{CoO}_2$  Li-ion battery<sup>10</sup>.

A suggested road map for development of electrode materials for Li-ion batteries is showed in Figure 1.8. In terms of cathode materials, LiCoO<sub>2</sub> was firstly considered and applied in electronic devices. However, the disadvantages such as high cost, toxicity, safety issue and relatively low capacity (~135 mAh g<sup>-1</sup>) limited its large-scale application<sup>63</sup>. Later LiMn<sub>1.5</sub>Ni<sub>0.5</sub>O<sub>4</sub> was developed and proved to have high working voltage of 4.7 V (compared to 4.1 V for LiCoO<sub>2</sub>). LiMPO<sub>4</sub> (M=Co, Fe, Mn, Ni or combinations of those) compounds are also becoming attractive due to their high capacity, e.g., 197 mAh g<sup>-1</sup> for Li<sub>3</sub>V<sub>2</sub>PO<sub>4</sub><sup>64</sup>. Whereas, there are still challenges

like rate capability and cycling performance for those to be commercially used. Besides, Li-excess layered oxides such as (Li<sub>2</sub>MnO<sub>3</sub>)<sub>x</sub>(LiMO<sub>2</sub>)<sub>1-x</sub> (M=Ni, Co, Mn) offered higher theoretical capacity (~250 mAh g<sup>-1</sup>) with a working voltage of ~4.0 V<sup>65</sup>. It is notable from Figure 7 that cathode materials like Li-O<sub>2</sub>, Li-S/C or Li<sub>2</sub>S-Si could be promising cathodes since they could offer even higher capacity. However, reversibility, compatibility and cycling performance are still big issues and need to be improved in the future<sup>66</sup>.

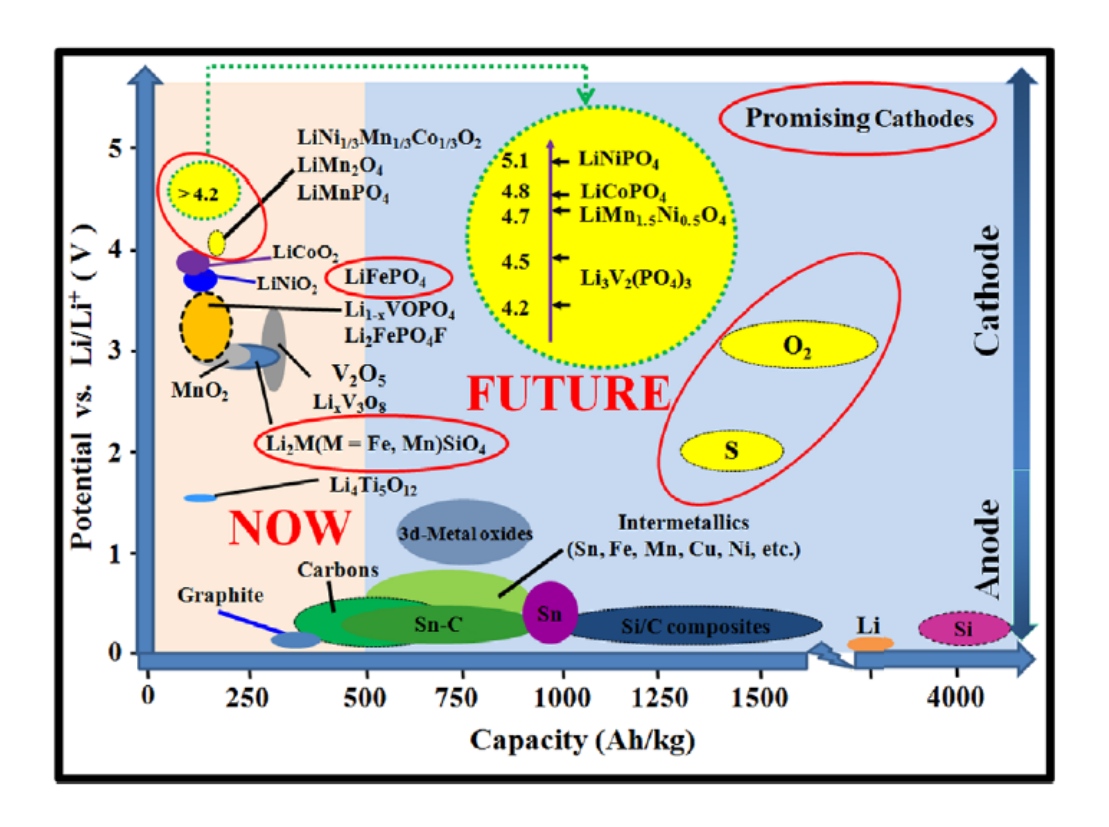


Figure 1.8: Current electrode materials road map<sup>67</sup>.

On the anode side, carbon in the form of graphite is the most widely used anode material in Li-ion cells due to its capability of intercalation and deintercalation of Li ions into and from its layered structure<sup>68-69</sup>. Although high energy density can be achieved by combining graphite and suitable cathodes, the low react potentials will easily lead to the formation of a passivating solid electrolyte interphase (SEI)<sup>63</sup> on the graphite side and result in poor cycle performance of the cell.

Furthermore, volumetric expansion or shrinkage of graphite occurred during the charging and discharging processes will possibly reduce the interfacial contact and lead to capacity fading. Lithium titanate (LTO) is another promising anode material, and known as "zero strain" due to extremely small volumetric change (~0.2%) during Li ion intercalation and deintercalation <sup>70</sup>. As a result, LTO has the characteristics of good cycle life, high rate capability and excellent safety features. While graphite can only accommodate one Li atom per graphene unit and thus having theoretical electrochemical capacity of 372 mAh g<sup>-1</sup>, other metals and metalloids such as Sn and Si, can accommodate more than four Li atoms per unit and thereby reaching much high capacities of 960 and 4009 mAh g<sup>-1</sup>, respectively<sup>71</sup>.

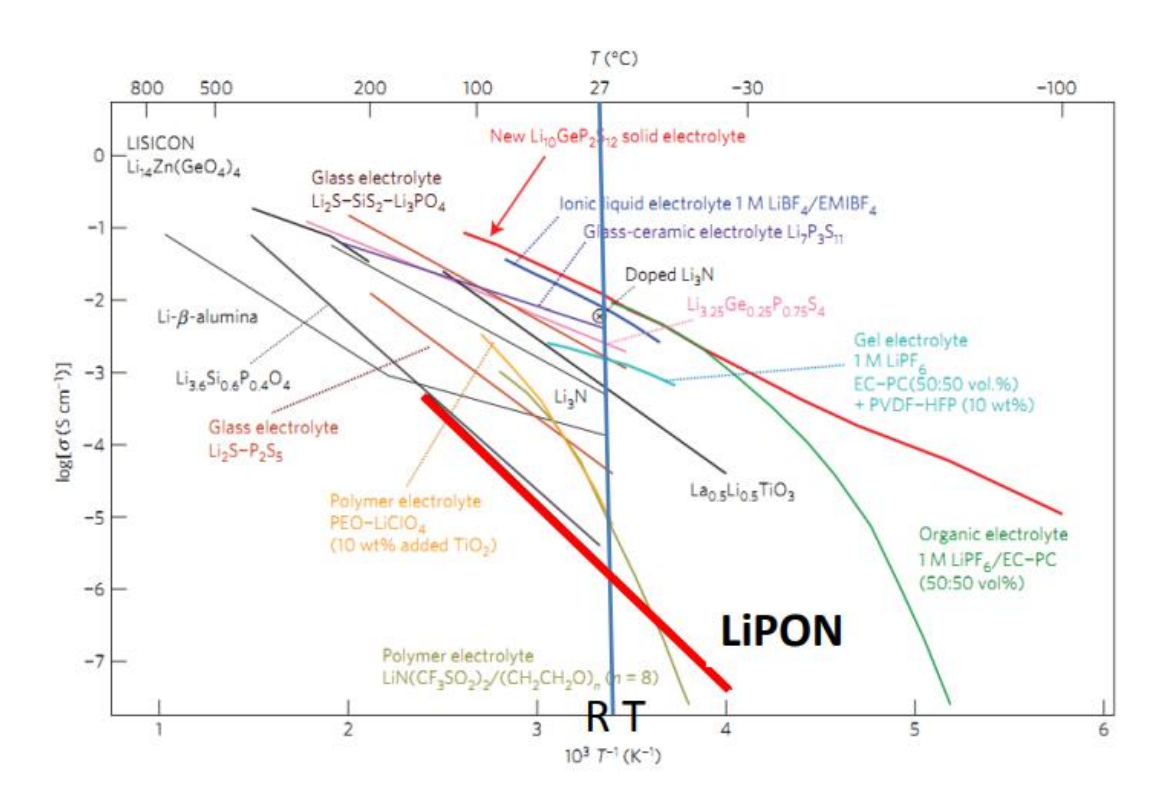


Figure 1.9: Temperature dependence of ionic conductivity of various electrolyte materials<sup>72</sup>.

Turning to electrolyte materials, they can be organized into several groups: inorganic solidstate electrolytes, organic liquid electrolytes, polymer electrolytes, ionic liquid and gel electrolytes.

Because electrolytes are primarily used to conduct ions during charging and discharging processes, ionic conductivity is one of the most critical criteria when selecting suitable candidates. The temperature dependence of ionic conductivity of commonly used Li electrolytes has been summarized in Figure 1.9. Among these various kinds of electrolyte materials, liquid electrolytes such as LiBF<sub>4</sub>, LiPF<sub>6</sub> dissolved in organic solvents like ethylene carbonate (EC) and dimethyl carbonate (DMC), have the disadvantages of poor electrochemical stability, limited operation temperature range, leakage, and most importantly the safety concerns (flammable)<sup>73</sup>. The polymer electrolytes, although having characteristics of great safety, easily preparation and flexible shape, there are many problems existed including instability of electrolyte/electrode interface, narrow operation temperature and limited mechanical properties<sup>74-76</sup>. Thus, in order to select proper electrolyte materials for large-scale application without safety issues, inorganic solid-state electrolytes might be the solution. Firstly, inorganic solid-state electrolytes display comparable ionic conductivity with liquid electrolytes, e.g., garnet-type oxides<sup>77</sup> exhibit high Li-ion conductivity of 10<sup>-3</sup> S cm<sup>-1</sup> at 25 °C, Li<sub>10</sub>GeP<sub>2</sub>S<sub>2</sub><sup>72</sup> offers superior Li ionic conductivity of 1.2 x 10<sup>-1</sup> <sup>2</sup> S cm<sup>-1</sup> at room temperature. Secondly, solid electrolytes generally perform wider electrochemical window than liquid electrolytes, which enable the cell to be operated under high cut-off voltage. In addition, good thermal stability of solids widens the operation temperature of batteries. Last but not the least, great safety operating environment can be achieved.

# 1.3.2 Electrolyte material LiPON

Lithium phosphorous oxynitride (LiPON) with general formula  $Li_xPO_yN_z$ , where x=2y+3z-5, are widely used as thin-film solid-state electrolytes in Li-ion battery. They were pioneered at Oak Ridge National Laboratory by sputtering  $Li_3PO_4$  target in  $N_2$  gas, while the ionic conductivity increased from 7 x  $10^{-8}$  S cm<sup>-1</sup> to 2.2 x  $10^{-6}$  S cm<sup>-1</sup> at room temperature<sup>78</sup>. Figure 1.10

reveals the quaternary diagram of stoichiometries of LiPON with four starting compounds (LiO<sub>1/2</sub>, LiN<sub>1/3</sub>, PO<sub>5/2</sub> and PN<sub>5/3</sub>). Most of the reported stable or meta-stable phases among the LiPON family are included. Besides the stoichiometric relationships, various structural patterns can be observed among the LiPON family. The tetrahedral PO<sub>4-x</sub>N<sub>x</sub> can be identified for all LiPON structures, but with different connecting options<sup>79-82</sup>. It can be [PO<sub>4</sub>]<sup>-3</sup> in Li<sub>3</sub>PO<sub>4</sub>, [PN<sub>4</sub>]<sup>-7</sup> in Li<sub>7</sub>PN<sub>4</sub>, or phosphate dimers  $[P_2O_7]^{-4}$  in Li<sub>4</sub>P<sub>2</sub>O<sub>7</sub> compound. In addition, the long chains pattern by phosphate groups sharing tetrahedral corner atoms can be found in LiPO<sub>3</sub><sup>83</sup>.

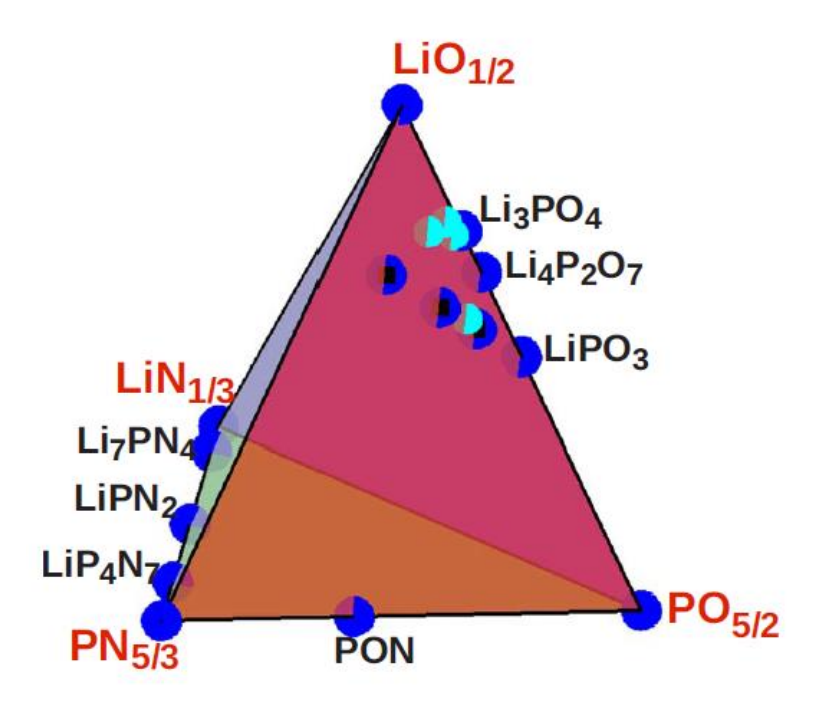


Figure 1.10: Composition diagram with starting materials of  $LiO_{1/2}$ ,  $LiN_{1/3}$ ,  $PO_{5/2}$  and  $PN_{5/3}$ . Natural and synthetic crystalline materials are labeled as dark (blue) circles, thin-film compositions as light (turquoise) circles, and examples of stable and meta-stables nitride phosphate materials as black square<sup>83</sup>.

Another interesting aspect in the LiPON family is the local environment of doping N atoms. Singly coordinated N can be found in Li<sub>7</sub>PN<sub>4</sub>, while doubly coordinated N was observed in

 $LiPN_2^{84-85}$ . Moreover, N can be both doubly and triply coordinated in structures like  $\alpha$ -P<sub>3</sub>N<sub>5</sub><sup>86</sup>. However, the actual local environment of doping N and its coordination in LiPON remains inconclusive and will be discussed in the following chapter.

LiPON is one of the most frequently used solid electrolytes in thin-film batteries. It had been reported that thin film batteries with LiCoO<sub>2</sub> as cathode, Li metal as anode and LiPON as electrolyte, are quite stable during the charge-discharge reactions (20,000 cycles with 0.001% capacity loss)<sup>87-88</sup>. Although the ionic conductivity of LiPON is relatively low comparing to other solid-state electrolytes in Figure 1.8, it is the only demonstrated solid-state electrolyte which is quite stable in direct contact with Li metal at potentials from 0 - 5 V, as shown in Figure 1. 11, which enables the potential of doubling the energy density of current commercial batteries<sup>89-91</sup>. In addition, LiPON can be used as additional stable protective SEI on top of liquid or polymer electrolyte to prevent reaction between electrodes and electrolyte<sup>92</sup>. However, the structure of LiPON, the effects of N doping, the interface reaction at LiPON/Li and the origin of its good electrochemical stability remains inconclusive, which we will discuss more in Chapter 6 and 7.

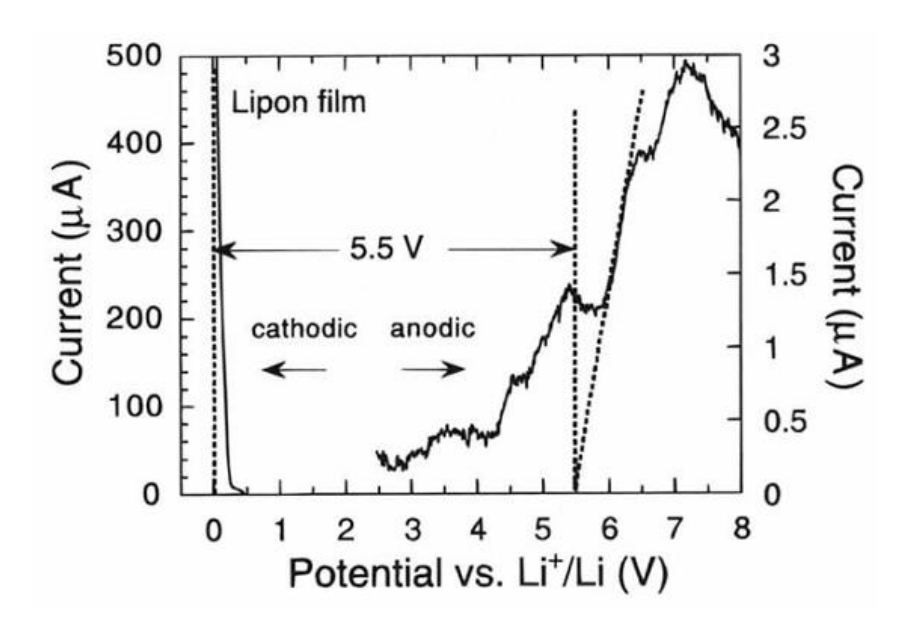


Figure 1.11: Current-potential curve of a LiPON/Pt half-cell with respect to Li/Li<sup>+</sup> reference<sup>91</sup>.

#### 1.4 Modeling techniques on structural and dynamical properties of energy materials

Considering the current experimental techniques have limits on studying specific research problems, computational modeling methods, which construct mathematical models to numerically study the behaviors of complex systems by simulation of computers, are proven to be quite powerful, efficient and reliable in many subjects including materials science, physics, chemistry, biology, etc. Figure 1.12 shows some popular computational techniques for different length and time scales. In this chapter we will discuss density-functional theory (DFT) and density-functional tight-binding (DFTB) in details since they are the computational techniques we will include in the following chapters for tetrahedrites and LiPON systems.

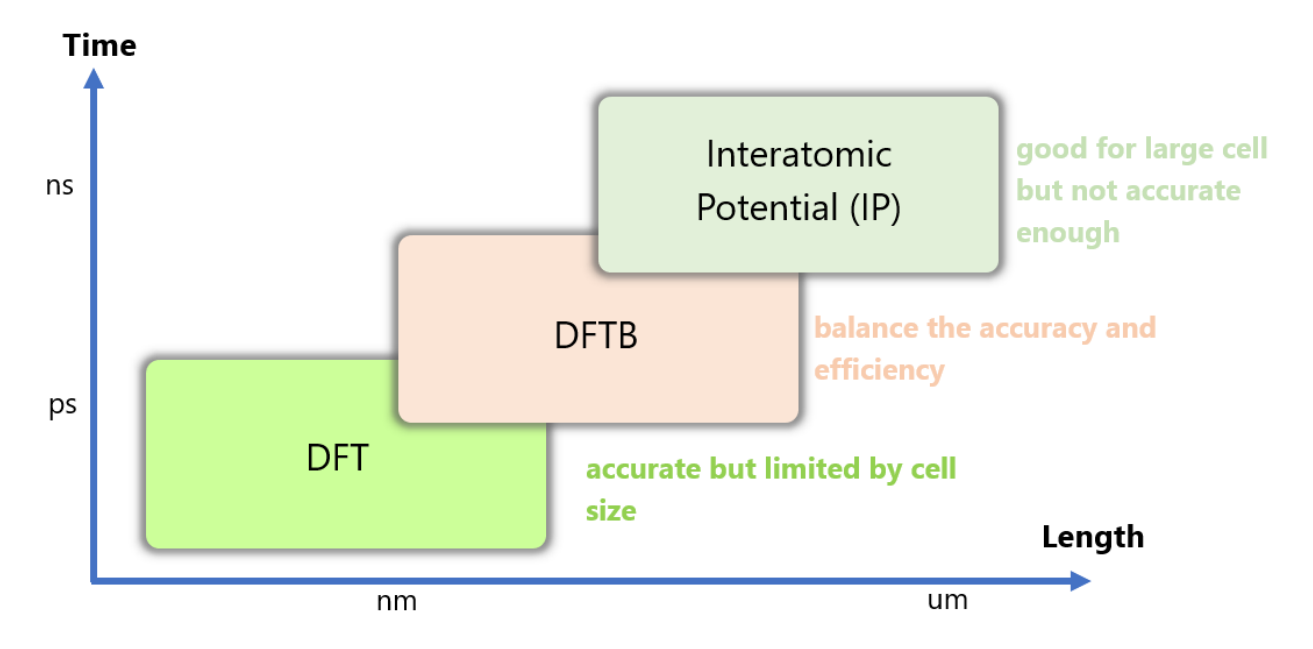


Figure 1.12: Popular computational techniques for different length and time scales.

#### 1.4.1 Introduction to DFT

DFT, developed by Hohenberg, Kohn and Sham<sup>93-94</sup>, is a computational quantum mechanical modelling method to investigate the electronic structure of many-body systems. DFT locates in the bottom left in Figure 1.9 indicating it is applied in the smallest length and time scale,

while it is the most accurate one as well. DFT reformulates the Schrödinger equation (SE), which describes the behavior of electron in a system, so that analytical solutions to SE can be tractable for real materials. Kohn and Sham<sup>94</sup> defined the most complex electron interactions in an exchange-correlation functional, whose explicit form remains unknown and need to be approximated. Thus, the selection of exchange-correlation functional, in a way, determines the accuracy of DFT calculation<sup>95-96</sup>.

The foundation of modeling material properties is based on the interactions between the electrons and nuclei, which follow the fundamental laws of quantum mechanics (QM). The basic of QM is the solution of SE, with the form of:

$$H\Psi = E\Psi, \tag{3}$$

where  $\Psi$  is wave function of the system, H and E is a Hamiltonian and an eigenvalue of the wave function, respectively. However, in practical cases, it is difficult to solve the exact H in many-electrons systems, thus, the Born-Oppenheimer (BO) approximation<sup>97</sup> has been made to solve SE by considering independent motions of electrons and nuclei. Nonempirical ab initio simulation with BO can calculate the system energy accurately, however, with very expensive computational cost and hence limits the numbers of atoms and the timescale. Later some empirical or semi-empirical methods are developed to research the material properties. Among them, DFT is the most accurate and least expensive, and hence the most popular one.

The fundamental of DFT based on two theorems by Hohenberg<sup>93</sup> and Kohn<sup>94</sup>: Hohenberg proposed that the ground-state wave function  $\Psi$  is a unique functional of the electron density function  $\rho(r)$  and therefore making the SE tractable by reducing the degree of freedom in SE from 3N to 3 dimensions; Kohn presented that the defined energy functional can be minimized by a

ground-state electron density  $\rho_0$ . With these two theorems, the total energy E within DFT can be expressed as:

$$E = T[\rho] + \int V_{ext}\rho(r)dr + \frac{1}{2} \iint \frac{\rho(r)\rho(r')}{|r-r'|} dr dr' + E_{XC}[\rho], \tag{4}$$

where  $T[\rho]$  is the kinetic energy of a noninteracting system with density  $\rho(r)$ ,  $V_{ext}$  is the external potential of electron and neutron interactions, the third term refers to the potentials of electron-electron interactions, and the last term  $E_{XC}[\rho]$  corresponds to the electron exchange-correlation energy of an interacting system with density  $\rho(r)$ . Kohn and Sham<sup>94</sup> also showed that the charge density  $\rho(r)$  can be represented by:

$$\rho(r) = \sum_{i=1}^{N} |\varphi_i(r)|^2,$$
(5)

$$\left(-\frac{1}{2}\nabla^2 + v_{eff}(r)\right)\varphi_i(r) = \varepsilon_i\varphi_i(r),\tag{6}$$

where  $\varphi_i(r)$  is the wave function of electron i for SE,  $v_{eff}$  is the effective external potential,  $\varepsilon_i$  is the eigenvalues. As we mentioned above, the exact form of  $E_{XC}[\rho]$  is still unknown. However, if  $\rho(r)$  varies sufficiently, the  $E_{XC}[\rho]$  can be written as:

$$E_{XC}[\rho] = \int \rho(r) \varepsilon_{XC}(\rho(r)) dr, \tag{7}$$

where  $\varepsilon_{XC}$  is defined as exchange and correlation energy per electron with density  $\rho$ .

The approximation of exchange-correlation energy is one of the most important steps during practical DFT applications, which has been developed by many researchers. Local density approximation (LDA)<sup>98</sup> or local-spin-density approximation (LSDA)<sup>99</sup> are the most successful ones, which have been proven to be reliable for solids. While generalized gradient approximation (GGA) is more accurate by applying gradient corrections, it is getting more and more attractions. Perdew-Burke-Ernzerhof (PBE) parametrization<sup>100</sup> within GGA is now the most widely used

model, especially in materials science. Later on, hybrids method was proposed by replacing a fraction of GGA exchange with Hartree-Fock (HF) exchange, for example, B3LYP method, which is more popular among chemists<sup>101</sup>. Figure 1.13 shows the number of recent DFT citations using these two methods, PBE and B3LYP. Besides, the Dark legend in the figure refers to those papers using either one without citing the original papers, and Other means all other DFT-related papers.

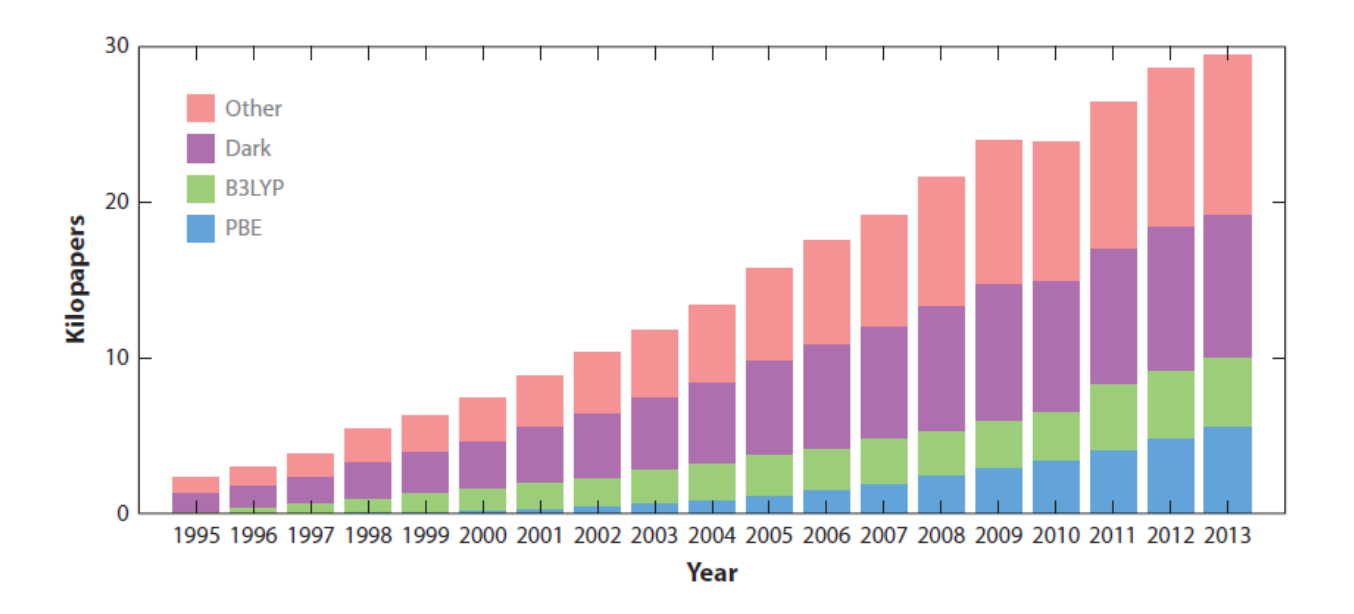


Figure 1.13: The number of DFT citations from 1995 to  $2013^{102}$ .

Molecular dynamics (MD) is widely used combining with DFT method, which describes the motion of collected atoms by their positions and momenta, and estimate the macroscopic physical properties by means of statistical mechanics<sup>103</sup>. Time evolution of the system can be determined by solving classical Newton's law:

$$\vec{F}_i(t) = m_i \frac{d^2 \vec{r}_i}{dt^2} = -\nabla U, \tag{8}$$

where  $\vec{F}_i(t)$  is the force acting on atom i at time t,  $m_i$  the atomic mass,  $\vec{r}_i$  the position, and U the interaction potential. A practical MD simulation requires an initial unit cell, periodic boundary condition, proper selection of interaction potentials, and stabilized controlment of temperature and

pressure. MD simulation can be accomplished in various ensembles, such as grand canonical  $(\mu VT)$ , canonical (NVT), microcanonical (NVE) and isothermal-isobaric (NPT). The temperature and pressure can be adjusted by pre-defined thermostat (e.g., Langevin, Berendsen, Nose-Hoover) and barostat (e.g. Parrinello-Rahman, Andersen, Berendsen), respectively.

The general inputs of DFT include the coordinates of atoms, boundary condition of unit cell, the choice of exchange-correlation functional, the parameters and algorithms for numerical and iterative convergence, and the way to treat electron system (typically the use of pseudopotentials). The outputs of DFT are useful quantities such as the total energy of system, cohesive energies, energy barriers, charge density of electrons, electronic band structure, etc<sup>104-105</sup>. DFT is proven to be powerful in predicting properties of energy materials and design of new materials in various aspects, such as thermoelectrics<sup>39</sup>, Li-ion batteries<sup>106-107</sup>, hydrogen production and storage<sup>108</sup>, superconductors<sup>109</sup>, photovoltaics<sup>110</sup>, etc<sup>111</sup>. Therefore, in this thesis we apply the reliable and accurate DFT method to study the structural, electronic and dynamics properties of tetrahedrite thermoelectrics in Chapter 2, 3, 4 and 5.

#### 1.4.2 Introduction to DFTB

However, the limitations of DFT still exist. For example, in a highly correlated electron systems, most functionals will fail. In addition, considering current computational expense, the simulated cell size cannot be too large (typically 1,000 atoms or less) and the time period should be short, therefore, long-time dynamics cannot be extracted. Other limitations include the difficulty in modelling van del Waals interactions and non-ground state properties<sup>112</sup>. In recent years, DFTB method was derived from DFT by neglection, approximation and parametrization of integrals<sup>113-115</sup>, with the advantage of 2-3 orders of magnitude faster in computational speed therefore allowing the treatment of larger unit cell and longer simulation time.

The starting point of DFTB based on the second order expansion of the total energy expression of DFT<sup>113</sup>. The original form of total energy within DFT can be found in Equation (4). In a system of M electrons, N nuclei, at position  $\vec{R}$ , it may be rewritten as:

$$E_{tot}^{DFT} = \sum_{i}^{occ} \langle \Psi_i | -\frac{\Delta}{2} + V_{ext} + \frac{1}{2} \int' \frac{\rho(\vec{r}')}{|\vec{r} - \vec{r}'|} |\Psi_i \rangle + E_{XC}[\rho(\vec{r})] + \frac{1}{2} \sum_{\alpha,\beta}^{N} \frac{Z_{\alpha} Z_{\beta}}{|\vec{R}_{\alpha} - \vec{R}_{\beta}|}, \tag{9}$$

where the first term refers to over occupied Kohn-Sham eigenstates  $\Psi_i$ , the second is the exchange-correlation contribution and the third one is ion-ion core repulsion,  $E_{ii}$ . Then this equation can be reformulated by substituting the charge density by a superposition of neutral atomic density  $\rho_0^{\alpha}$ ,  $\rho_0 = \sum_{\alpha} \rho_0^{\alpha}$ , and expanding  $E_{XC}$  at the reference density to the second order in the density fluctuations, as the following:

$$E = \sum_{i}^{occ} \langle \Psi_{i} | \widehat{H}_{0} | \Psi_{i} \rangle - \frac{1}{2} \iint' \frac{\rho_{0} \rho_{0}'}{|\vec{r} - \vec{r}'|} + E_{XC}[\rho_{0}] - \int V_{XC}[\rho_{0}] \rho_{0} + E_{ii} + \frac{1}{2} \iint' \left( \frac{1}{|\vec{r} - \vec{r}'|} + \frac{\delta^{2} E_{XC}}{\delta \rho \delta \rho'} \Big|_{\rho_{0}} \right) \delta \rho \delta \rho', \tag{10}$$

where  $\int'$  represents the  $\int d\vec{r}'$ . From here, several approximations have been made to construct the DFTB total energy expression:

1. In the second-order term, the charge density fluctuation  $\delta\rho=\rho-\rho_0$  is represented by  $\delta\rho=\sum_{\alpha}\delta\rho_{\alpha}$ , while  $\delta\rho_{\alpha}$  can be approximated by atomic charge fluctuations  $\Delta q_{\alpha}=q_{\alpha}-q_{\alpha}^{0}$ , where  $q_{\alpha}$  is determined by Muliken population analysis and  $q_{\alpha}^{0}$  is the number of electrons for neutral atom  $\alpha$ . A function  $\gamma$ , depending on the Hubbard parameter  $U_{\alpha}$  ( $U_{\alpha}=\frac{1}{2}\frac{\partial^{2}E_{\alpha t}}{\partial q_{\alpha t}^{2}}$  is the second derivative of the total energy of a single atom  $\alpha$  with respect to the occupation number of the highest occupied atomic orbital), is introduced to represent the integral over  $\frac{1}{r}$  term and second derivative of  $E_{XC}$ . Therefore, the second-order term can be expressed as:

$$E^{2nd} = \frac{1}{2} \sum_{\alpha,\beta} \Delta q_{\alpha} \Delta q_{\beta} \gamma_{\alpha\beta}. \tag{11}$$

2. Kohn-Sham eigenstates  $\Psi_i$  are expanded in a minimal basic set  $\phi_{\mu}$ , which consists a linear combination of atomic orbitals<sup>116-117</sup>, in the form of:

$$\Psi_i = \sum_{\mu} c_{\mu}^i \, \phi_{\mu}. \tag{12}$$

Here  $\phi_{\mu}$  is determined by solving a modified Kohn-Sham equation:

$$\left[T + v_{eff}(\rho) + \left(\frac{r}{r_0}\right)^{\sigma}\right]\phi_{\mu} = \epsilon_{\mu}\phi_{\mu},\tag{13}$$

where T is the kinetic energy operator and  $v_{eff}$  the effective potential of a free neutral pseudoatom. Originally  $r_0$ , the compression radius, was treated as a variational parameter<sup>116</sup> but in practice it is chosen to be 2 times the covalent radius<sup>113</sup>. Here  $\sigma$  has a default value of 2.

When two-center approximation has been adjusted for non-diagonal elements and eigenvalues of the free atom serve as diagonal elements, the Hamiltonian matrix elements yielded as:

$$\widehat{H}_{\mu\nu}^{0} = \begin{cases} \varepsilon_{\mu}^{free \, atom} & \text{if } \mu = \nu \\ \langle \phi_{\mu} | \widehat{H} (\rho_{\alpha}^{0} + \rho_{\beta}^{0}) | \phi_{\nu} \rangle & \text{if } \mu \in \alpha, \nu \in \beta, \alpha \neq \beta \end{cases}$$

$$0 & \text{otherwise}$$

$$(14)$$

The Hamilton  $\widehat{H}_{\mu\nu}$  can be precalculated and tabulated with the overlap matrix  $S_{\mu\nu}$  for interatomic distances and leads to a new expression as:

$$\widehat{H}_{\mu\nu} = \widehat{H}_{\mu\nu}^0 + \frac{1}{2} S_{\mu\nu} \sum_{\gamma} \Delta q_{\gamma} (\gamma_{\alpha\gamma} + \gamma_{\beta\gamma}), \tag{15}$$

where  $S_{\mu\nu} = \langle \phi_{\mu} | \rangle \phi_{\nu}$ . The solution of the eigenvalue problem for  $\widehat{H}_{\mu\nu}$  dominates the computational cost of DFTB calculation and hence provide the efficiency of this method.

3. For the remaining terms of Eq. (10), they can be summarized and defined as a short-range repulsive energy  $E_{rep}$  as:

$$E_{rep} = -\frac{1}{2} \iint' \frac{\rho_0 \rho_0'}{|\vec{r} - \vec{r}'|} + E_{XC}[\rho_0] - \int V_{XC}[\rho_0] \rho_0 + E_{ii}.$$
 (16)

 $E_{rep}$  is then approximated as a sum of two body potentials<sup>118</sup> as:

$$E_{rep} = \sum_{\alpha,\beta} U_{\alpha\beta} (R_{\alpha\beta}), \tag{17}$$

where  $U_{\alpha\beta}$  refers to atom-type specific pair potentials, and is constructed as the difference between the total energy calculated in DFT and the corresponding electronic energy obtained by DFTB for the proper systems<sup>114, 119</sup> as:

$$U_{\alpha\beta}(R_{\alpha\beta}) = E_{total}^{DFT}(R_{\alpha\beta}) - E_{elec}^{DFTB}(R_{\alpha\beta}). \tag{18}$$

Thus, combining the approximations and substitutions discussed above, DFTB total energy formalism shows as:

$$E_{tot}^{DFTB} = \sum_{i,\mu,\nu} c_{\mu}^{i} c_{\nu}^{i} H_{\mu\nu}^{0} + \frac{1}{2} \sum_{\alpha,\beta} \Delta q_{\alpha} \Delta q_{\beta} \gamma_{\alpha\beta} + \sum_{\alpha,\beta} U_{\alpha\beta} (R_{\alpha\beta}), \tag{19}$$

where the first term contains the DFTB matrix elements and the third term describes the repulsive potential. These two terms together refer to standard (non-self-consistent) DFTB method<sup>117, 120</sup>, and the second term corresponds to the self-consistent charge (SCC) DFTB by approximation of the second order term of DFT Taylor series expansion.

DFTB, comparing to DFT, is efficient and suitable to study larger cell (more sampling) and long-time scale simulation, hence being applied to study the structure and dynamic properties such as diffusivity and ionic conductivity of LiPON in Chapter 6. We also use this method to investigate LiPON/Li metal interphase in Chapter 7 since a much larger cell is required.

## 1.4.3 Other computational techniques

There are many other available and successful modeling techniques in energy materials simulation, for example, interatomic potentials. Interatomic potentials use mathematical functions to calculate the potential energy of a system given atomic position in space<sup>121</sup>, which are popular due to its capability treating a large system (thousands of atoms). General interatomic potentials expression can be written as a series expansion of functional terms that depend on the position of atoms, while the total energy of the system  $E_{tot}$  becomes<sup>122</sup>:

$$E_{tot} = \sum_{i}^{N} E_{1}(\vec{r}_{i}) + \sum_{i,j}^{N} E_{2}(\vec{r}_{i}, \vec{r}_{j}) + \sum_{i,j,k}^{N} E_{3}(\vec{r}_{i}, \vec{r}_{i}, \vec{r}_{k}) + \cdots,$$
(20)

where  $E_1$ ,  $E_2$  and  $E_3$  is the one-body term, two-body term and three-body term, respectively, N the number of atoms,  $\vec{r}_i$  the position of atom i. The forces defined between atoms then can be obtained by taking three-dimensional derivative of  $E_{tot}$  with respect to the position of atom i as:

$$\vec{F}_i = -\nabla_{\vec{r}_i} E_{tot}. \tag{21}$$

The interatomic potentials have various kinds when dealing with different physical objects, including pair potentials (for example, Leonard-Jones potential<sup>123-124</sup>), many-body potentials (embedded atom model<sup>125</sup>, the Stillinger-Weber potentials<sup>126</sup>) and short-range repulsive potentials.

Although interatomic potentials method locates in the top right in Figure 1.9, it is still under the category of molecular scale methods, as well as DFT and DFTB. In addition to molecular scale methods, there are various modeling techniques<sup>103</sup> dealing with the simulation at microscale such as Brownian dynamics (BD)<sup>127-128</sup>, dissipative particle dynamics (DPD)<sup>129</sup>, lattice Boltzmann (LB)<sup>130</sup>, time-dependent Ginzburg-Landau (TDGL) method<sup>131</sup> and dynamic DFT method<sup>132</sup>. Furthermore, there are mesoscale and macroscale methods, such as micromechanics<sup>133</sup> and finite element analysis (FEA)<sup>134-135</sup>, to predict and analyze the macroscopic properties of materials. To

solve a research problem, it is helpful to combine two or even more modeling and computational methods discussed above to achieve a balance of efficiency and accuracy.

## 1.5 Dissertation outline

This dissertation is organized in 8 chapters as the following layout:

In the present chapter, Chapter 1, the fundamental scientific backgrounds are included, such as the current status of energy crisis, thermoelectric effect, application and performance of thermoelectric materials and introduction of tetrahedrite thermoelectric Cu<sub>12</sub>Sb<sub>4</sub>S<sub>13</sub>. Introduction to Li-ion batteries is also presented from the material science perspective, especially the electrolyte material LIiON.

In Chapter 2, neutron diffraction and computational study on pristine tetrahedrite Cu<sub>12</sub>Sb<sub>4</sub>S<sub>13</sub> is proposed, focusing on its low-temperature structure and properties. A metal-semiconductor transition (MST) occurred at 85 K was observed by significantly increasement of electronic resistivity upon cooling, accompanied with abrupt changes of magnetic properties and thermoelectric properties as Seebeck coefficient and thermal conductivity<sup>136-137</sup>. However, the discussion that whether there is a cubic to tetragonal phase transition at the MST temperature remains inconclusive<sup>138</sup>. Inspired by these works, we perform neutron diffraction measurement and computational simulation on tetrahedrite Cu<sub>12</sub>Sb<sub>4</sub>S<sub>13</sub>. No cubic to tetragonal phase transition at MST temperature can be identified, however, negative thermal expansion below 50 K is observed, according to both experimental and computational results. Sb-Cu*12e*-Sb interaction is examined at different temperatures. Thermoelectric related properties such as DOS, electrical resistivity, Seebeck coefficient and electrical thermal conductivity are calculated comparing to experimental data.

In Chapter 3, the incoherent and coherent dynamics study of tetrahedrite Cu<sub>10.5</sub>NiZn<sub>0.5</sub>Sb<sub>4</sub>S<sub>13</sub> by DFT-based MD simulations have been proposed. Recent inelastic neutron scattering (INS) experiment indicated the anomalous behavior of tetrahedrite called "phonon softening upon cooling". Calculated vibrational density of states (VDOS) derived from the Fourier transform of velocity autocorrelation function from simulation trajectory is presented comparing to INS data, where good consistency can be observed. Partial VDOS for Cu<sub>12e</sub> atoms at different temperatures shows that the low energy peak shifts to higher energy as temperature increases. The interaction between Cu<sub>12e</sub> and Sb at different temperatures is also included, where we discover that the reduction of anharmonic rattling of Cu between two Sb atoms upon cooling is responsible for the phonon softening. Coherent atomic dynamics are also examined by computing the longitudinal and transverse dynamics structure factor based on the momentum correlation function. Debye temperature, Debye heat capacity and sound velocity are calculated comparing to experimental data. Thermal conductivity is also extracted by making the approximation that the mean free path equals to the average interatomic spacing.

In Chapter 4, the transport properties study of Cu among Cu-rich tetrahedrite is presented using the Cu<sub>14</sub>Sb<sub>4</sub>S<sub>13</sub> as a model structure. Previous research<sup>139</sup> indicated that Cu becomes mobile above 393 K and are likely to be superionic conductors in Cu-rich tetrahedrite, while the excess Cu atoms were likely to be at Cu<sub>2</sub>4g sites, however, the insight of distribution and movement of Cu atoms remains unknown. Incoherent density correlation is calculated, from which the vibrating Cu group and diffusing Cu group can be identified. Cu self-diffusivity, jump length and residence time are investigated. The nuclear density map is proposed to visualize the movement of Cu atom between different sites, where several diffusion pathway can be observed. "Nudged elastic band"

(NEB) method is applied to estimate the migration energy barrier of different migration paths, where we select two actual paths (24g - 12d and 24g - 12e) from trajectory as examples.

In Chapter 5, we study the effect of cell size and basis set on results from DFT-based first-principles MD simulation of a model thermoelectric material: Cu<sub>10</sub>Zn<sub>2</sub>Sb<sub>4</sub>S<sub>13</sub> tetrahedrite. Two cell sizes, 1x1x1 with 58 atoms and 2x2x2 with 464 atoms are selected, with two popular basis sets, plane waves (PW) and atomic orbitals (AO). Structural and dynamic properties, such as lattice parameters, partial and total vibrational density of states, phonon dispersion, heat capacity, and EXAFS spectra, are extracted from each of the simulation. Good agreement can be achieved by comparing with each other, except some minor differences, e.g., the partial VDOS, which we ascribe to different electronic structures and atomic forces from different basis sets. The larger 2x2x2 cell allow us to access the region closer to the hydrodynamic limit of atomic dynamics to study materials properties.

In Chapter 6, structure and ionic conduction study on Li<sub>3</sub>PO<sub>4</sub> and LiPON with DFTB method is presented. N deposition into Li<sub>3</sub>PO<sub>4</sub> can increase the ionic conductivity from 7 x 10<sup>-8</sup> S/cm without any N content to 3.3 x 10<sup>-6</sup> S/cm according to previous study<sup>91, 140</sup>. However, the origin of the N doping effect, e.g., the N coordination with P atoms, remains uncertain. Moreover, the study on the amorphous structure of LiPON is limited. Here in this chapter we apply the DFTB method to generate four model structures, crystalline Li<sub>3</sub>PO<sub>4</sub> (c-Li<sub>3</sub>PO<sub>4</sub>), amorphous Li<sub>3</sub>PO<sub>4</sub> (a-Li<sub>3</sub>PO<sub>4</sub>), crystalline LiPON (c-LiPON) and amorphous LiPON (a-LiPON), to investigate their structural properties. Lattice parameters of crystalline phases are in good agreement with experimental data. Apical N (N<sub>a</sub>) and doubly-coordinated N (N<sub>d</sub>) can be identified in a-LiPON, whereas no triply-coordinated N (N<sub>t</sub>) exists. Bond order (BO) calculation is implemented to investigated different bonding environment around P and Li atoms. Electron localized function

(ELF) maps and statistical analysis are performed to study the Li environment as well. In addition, we examine self-diffusivity of different atomic groups. We discover that the addition of N in c-LIPON helps the diffusion of P and O in the crystalline phase by investigating the incoherent density correlation plots. Li self-diffusivity extracting by DFTB shows good consistency with experimental results. Ionic conductivities for all four structures are also included by extrapolation of a Fourier transform form of transverse coherent charge current density correlation function from MD trajectories.

In Chapter 7, preliminary study on LiPON/Li interphase is proposed. A LiPON/Li interphase supercell is generated. No decomposition of LiPON, and no Li ions exchange between the bulk and metallic Li layers can be observed. A 6 Å interface layer is identified by investigating the Li charge distribution, beyond which the metallic Li maintain as bcc structure. Projected DOS of selected layers and atoms are also revealed in this chapter, suggesting the metallic behavior of the interface.

In Chapter 8, future works focusing on thermoelectric materials tetrahedrite, LiPON/Li interface and promising cathode materials are included, as well as the conclusions of the dissertation.

# CHAPTER 2: Pristine tetrahedrite Cu<sub>12</sub>Sb<sub>4</sub>S<sub>13</sub>: neutron diffraction and computational study on low-temperature properties

# 2.1 Introduction

The wide applications of thermoelectric materials have been discussed above. Some important applications such as cryogen-free cryogenic solid-state cooling, required thermoelectric candidates with high efficiencies at low temperatures. However, study on thermoelectric properties at low temperature region (below 300 K) is still limited. It has been reported that a metalsemiconductor transition (MST) at around 85 K will occur in Cu<sub>12</sub>Sb<sub>4</sub>S<sub>13</sub><sup>46</sup>, indicated by significant increasement of electronic resistivity, from about 2 x  $10^{-5}$   $\Omega m$  at 90 K to  $\sim 1.5$  x  $10^{-4}$   $\Omega m$  at 50 K upon cooling. Thermoelectric properties such as Seebeck coefficient and thermal conductivity, are also reported to have abrupt change at the same temperature <sup>136</sup>. However, it is still controversial that whether a structural phase transition accompanies the MST. For example, May et al<sup>138</sup>. reported a cubic to tetragonal phase transition below 88 K, suggested by cubic Bragg peak (611) splitting from powder x-ray diffraction. They also found out that Zn-doping would suppress the structural distortion by comparing the temperature dependence of lattice parameters and phonon DOS from inelastic neutron scattering (INS) measurements for Cu<sub>12</sub>Sb<sub>4</sub>S<sub>13</sub> and Cu<sub>10</sub>Zn<sub>2</sub>Sb<sub>4</sub>S<sub>13</sub>. Tanaka et al. compared synchrotron x-ray diffraction data of Cu<sub>12</sub>Sb<sub>4</sub>S<sub>13</sub> at 100 K and 75 K, and observed that (400) peak at 100 K split into double peaks at 75 K and concluded that the cubic to tetragonal phase transition was associated with MST<sup>137</sup>. On the other hand, Nasonova et al. did not observe structural transformation, nor any sign of reflection peaks splitting, by performing highresolution power X-ray diffraction<sup>136</sup>. Another characteristic phenomenon that occurred in tetrahedrite, is abrupt drop of magnetic susceptibility upon cooling, which also ascribed to the distribution of Cu 12e<sup>137, 141</sup>.

In this work, we present crystal structure study of stoichiometric  $Cu_{12}Sb_4S_{13}$  by neutron diffraction measurement in the temperature range of 20-300 K, comparing to experimental synchrontron x-ray data to have better understanding of the proposed structural phase transition. Density functional theory-based first-principles molecular dynamics simulation is also applied to investigate the origin of the unique low-temperature features of  $Cu_{12}Sb_4S_{13}$  and calculate its thermoelectric properties at low temperature range.

## 2.2 Computational and experimental details

Vienna Ab initio Simulation Package (VASP)<sup>142-145</sup> code employing the Projector Augmented-Wave (PAW) method was used for molecular dynamics (MD) and BoltzWann<sup>146-147</sup> module of Wannier90<sup>148</sup> code. Valence electron configurations for Cu, Sb, S atoms are 4s<sup>1</sup>3d<sup>10</sup>, 5s<sup>2</sup>5p<sup>3</sup>, and 3s<sup>2</sup>3p<sup>4</sup>, respectively. The plane wave energy cutoff was 450 eV. The generalized gradient approximation (GGA) with Perdew-Burke-Ernzerhof (PBE) parametrization<sup>100</sup> was applied as exchange-correlation (XC) functional and 2 x 2 x 2 k-mesh was used. Simulation cell was a 1 x 1 x 1 scale of unit cell with 58 atoms. For MD simulations, first a constant number of particles, pressure and temperature (NPT) ensemble was performed at 20, 50, 87.5 and 300 K for 3 ps to obtain lattice parameters. Then a constant number of particles, volume and energy (NVE) ensemble was implemented for 5 ps for equilibration and 20 ps for production at same temperatures as NPT. Time step was 1 fs for all the MD runs.

Thermoelectric properties were obtained by BoltzWann module of the Wannier90 package using results from DFT-based MD as input<sup>146-147</sup>. Relaxation time of BoltzWann calculation is set to be 10 fs.

Tetrahedrite ( $Cu_{12}Sb_4S_{13}$ ) powder was synthesized by the modified polyol process proposed by Weller et al<sup>149</sup>. To ensure uniform particle size, the powder was loaded into a stainless-

steel ball mill jar and milled for 10 min via a SPEX 8000D vibratory ball mill. Phase-purity of tetrahedrite powder was confirmed by X-ray diffraction (XRD) via a Rigaku Miniflex benchtop diffractometer with Cu K $\alpha$  radiation. No impurity phases were detected by XRD. Energy dispersive X-ray spectroscopy (EDS) was performed with a Hitachi TM-3000 Tabletop Microscope, a Bruker XFlash MIN SVE detector, and an accelerating voltage of 15 kV. Data for atomic ratios were averaged over 4 sites and normalized to the measured S content. The measured composition according to EDS was  $Cu_{13.4\pm0.3}Sb_{4.1\pm0.1}S_{13.0\pm0.3}$ .

Neutron diffraction was conducted at the BL-11A POWGEN beamline, Spallation Neutron Source (SNS), Oak Ridge National Laboratory, using our synthesized Cu<sub>12</sub>Sb<sub>4</sub>S<sub>13</sub> sample, at 20 K, 50 K, 87.5 K, and 300 K. The software Jana2006 was used for structure refinement<sup>150</sup>.

# 2.3 Results and Discussion

# 2.3.1 Low temperature structure of Cu<sub>12</sub>Sb<sub>4</sub>S<sub>13</sub>

Neutron diffraction was conducted at four different temperatures as shown in Figure 2.1. Earlier reports  $^{137-138}$  proposed that 004 peak was split into two peaks under MST temperature and thus  $Cu_{12}Sb_4S_{13}$  underwent phase distortion from cubic to tetragonal symmetry. In our case, no peak splitting of 004 reflection can be observed below the MST temperature, indicating that no structural phase transition occurred, and  $Cu_{12}Sb_4S_{13}$  stayed as cubic phase, which is in good agreement with the synchrontron x-ray data from Nasonova et al  $^{136}$ .

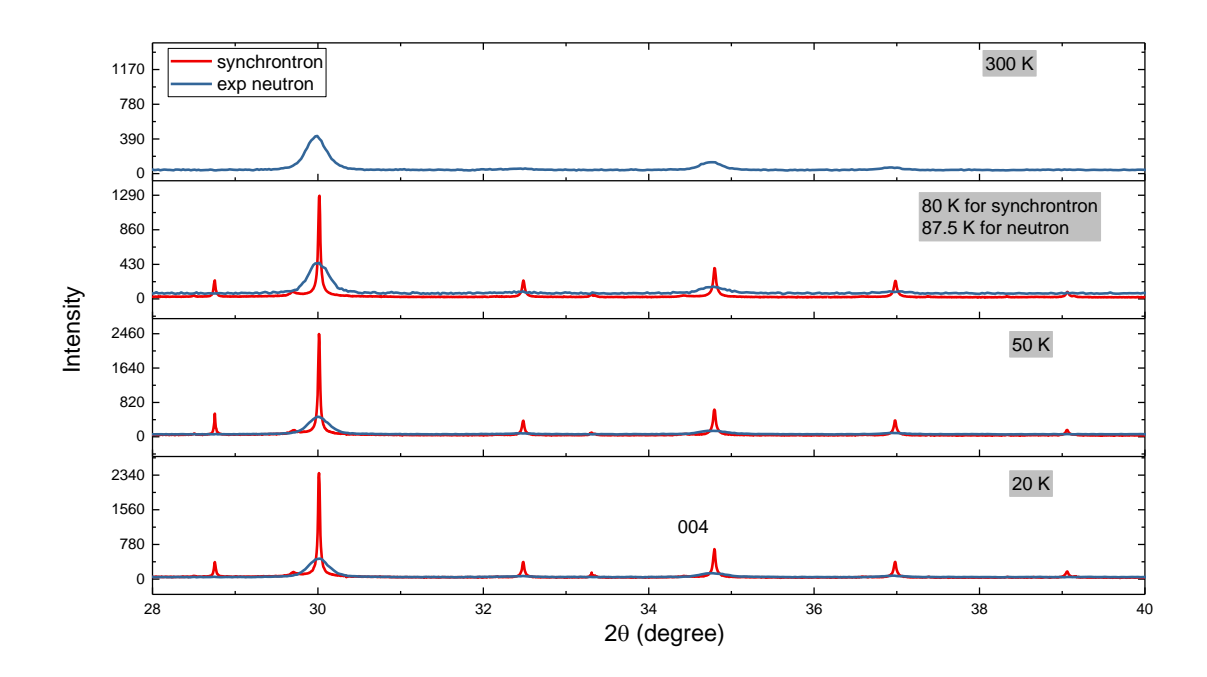


Figure 2.1: Neutron diffraction data for  $Cu_{12}Sb_4S_{13}$  at 20, 50, 87.5 and 300 K, synchrontron x-ray data by Nasonova el al. are shown for comparison. No peak splitting can be identified below MST temperature.

High quality of Rietveld refinement can be obtained for all temperatures using Cu<sub>12</sub>Sb<sub>4</sub>S<sub>13</sub> as a model as Figure 2.2 and 2.3. Occupancy of Cu*12e* and Cu*12d* were relaxed, while occupancy of S and Sb were fixed. Anisotropic atomic displacement parameters were used for all atom types. Atomic parameters at 20 K, 50 K, 87.5 K and 300 K are listed from Table 5.1 to Table 5.4. We also used a Cu-rich tetrahedrite model Cu<sub>13.2</sub>Sb<sub>4</sub>S<sub>13</sub>, created based on Vaqueiro's study<sup>139</sup>, for Rietveld refinement at 87.5 K for comparison, since this composition is close to our measure composition by EDS.

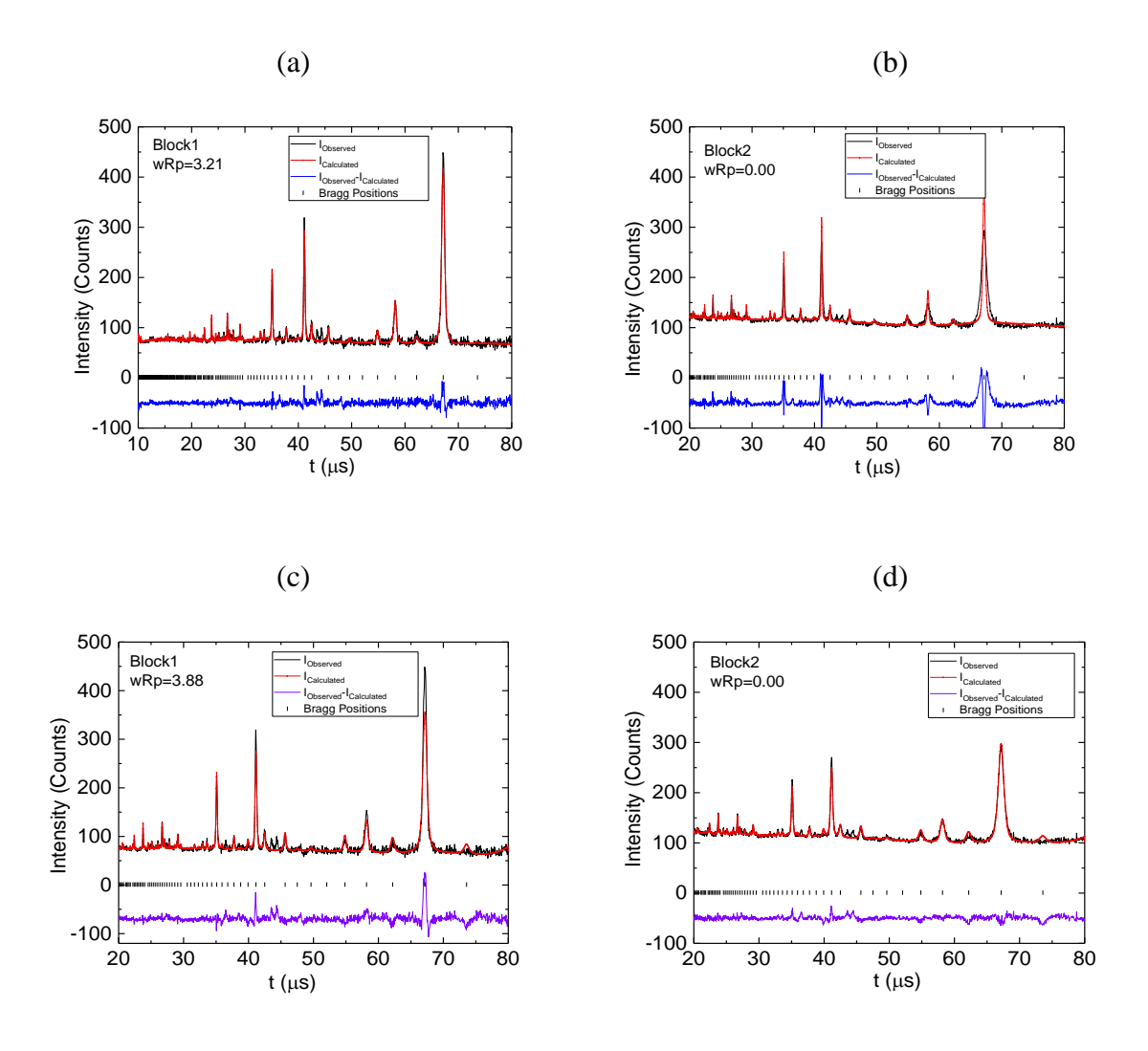


Figure 2.2: Neutron diffraction data collected for tetrahedrite sample at 87.5 K using (a, b)  $Cu_{12}Sb_4S_{13}$  and (c,d)  $Cu_{13.2}Sb_4S_{13}$  as model structures. Block 1 contains 80% of the data and block 2 has the rest 20%.

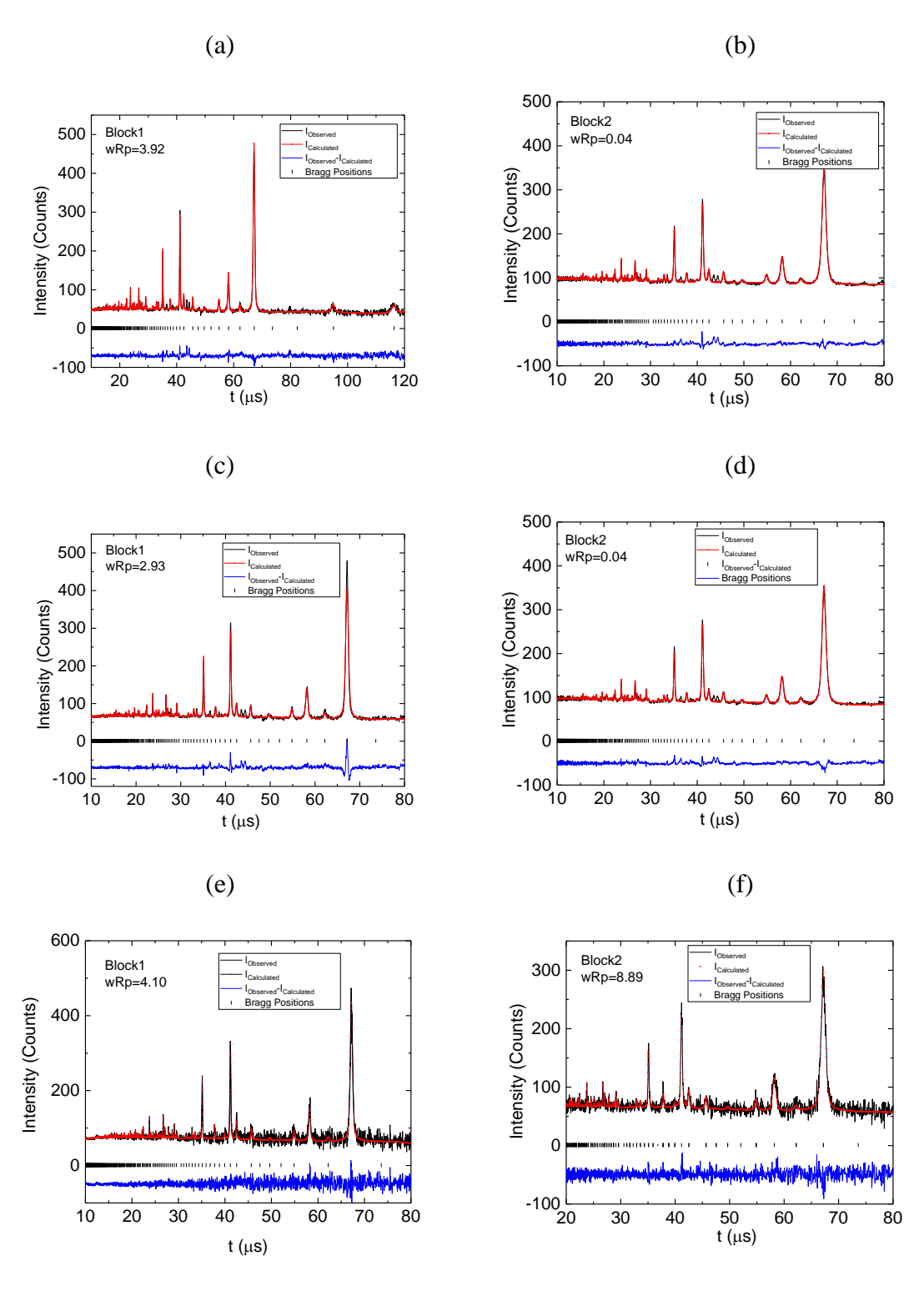


Figure 2.3: Neutron diffraction data collected for tetrahedrite sample at (a, b) 20 K, (c, d) at 50 K and (e, f) at 300 K using  $Cu_{12}Sb_4S_{13}$  structure as model. Block 1 contains 80% of the data and block 2 has the rest 20%.

Table 2.1: Atomic parameters in the crystal structure of Cu<sub>12</sub>Sb<sub>4</sub>S<sub>13</sub> at 20 K.

Atom	Pos.	Occu.	х	у	Z	U11(A^2)	U22	U33	U12	U13	U23	Uiso
Cu	12d	0.253751	0.5	0	0.25	0.011894	0.011894	0.051497	0	0	0	0.025095
Cu	12e	0.224567	0	0	0.214035	0.058684	0.058684	0.034048	0.037013	0	0	0.050472
Sb	8c	0.16667	0.261505	0.261505	0.261505	0.024516	0.024516	0.024516	0.008778	0.008778	0.008778	0.024516
S	2a	0.041667	0	0	0	0.093545	0.093545	0.093545	0	0	0	0.093545
S	24g	0.5	0.886243	0.886243	0.361347	0.005342	0.005342	0.010751	0.01381	-0.01464	-0.01464	0.007145

Table 2.2: Atomic parameters in the crystal structure of Cu<sub>12</sub>Sb<sub>4</sub>S<sub>13</sub> at 50 K.

Atom	Pos.	Occu.	х	у	z	U11(A^2)	U22	U33	U12	U13	U23	Uiso
Cu	12d	0.267736	0.5	0	0.25	0.023131	0.023131	0.059703	0	0	0	0.035322
Cu	12e	0.236726	0	0	0.215254	0.07577	0.07577	0.045305	0.040005	0	0	0.065615
Sb	8c	0.16667	0.261751	0.261751	0.261751	0.03073	0.03073	0.03073	0.01817	0.01817	0.01817	0.03073
S	2a	0.041667	0	0	0	0.084369	0.084369	0.084369	0	0	0	0.084369
S	24g	0.5	0.886196	0.886196	0.363424	0.003746	0.003746	0.022949	0.012198	-0.01412	-0.01412	0.010147

Table 2.3: Atomic parameters in the crystal structure of Cu<sub>12</sub>Sb<sub>4</sub>S<sub>13</sub> at 87.5 K.

Atom	Pos.	Occu.	х	у	Z	U11(A^2)	U22	U33	U12	U13	U23	Uiso
Cu	12d	0.300856	0.5	0	0.25	0.024975	0.024975	0.066094	0	0	0	0.038681
Cu	12e	0.200088	0	0	0.214784	0.050644	0.050644	0.018469	0.00977	0	0	0.039919
Sb	8c	0.16667	0.264096	0.264096	0.264096	0.008097	0.008097	0.008097	0.007339	0.007339	0.007339	0.008097
S	2a	0.041667	0	0	0	0.083969	0.083969	0.083969	0	0	0	0.083969
S	24g	0.5	0.881418	0.881418	0.364786	0.007672	0.007672	0.048948	-0.01577	-0.01577	-0.01456	0.021431

Table 2.4: Atomic parameters in the crystal structure of Cu<sub>12</sub>Sb<sub>4</sub>S<sub>13</sub> at 300 K.

Atom	Pos.	Occu.	x	у	Z	U11(A^2)	U22	U33	U12	U13	U23	Uiso
Cu	12d	0.315699	0.5	0	0.25	0.027136	0.027136	0.074901	0	0	0	0.043058
Cu	12e	0.216672	0	0	0.216946	0.071096	0.071096	43153	-0.05988	0	0	14384.38
Sb	8c	0.16667	0.267751	0.267751	0.267751	0.005902	0.005902	0.005902	-0.00122	-0.00122	-0.00122	0.005902
S	2a	0.041667	0	0	0	0.025203	0.025203	0.025203	0	0	0	0.025203
S	24g	0.5	0.88099	0.88099	0.359754	0.007221	0.007221	0.03179	-0.01152	-0.01074	-0.01074	0.015411

Lattice parameters from DFT-MD NPT ensemble have been plotted in Figure 2.4, together with lattice parameters obtained from our neutron diffraction experiment and synchrontron x-ray from Nasonova's work<sup>136</sup>. MD simulation showed that Cu<sub>12</sub>Sb<sub>4</sub>S<sub>13</sub> maintained as cubic symmetry at the designed temperature range, which is consistent with our neutron experiment. MD data are about 0.4% higher than neutron and synchrontron data, indicating good reliability of our

simulation. For both MD and neutron lattice parameters, positive thermal expansion from 50-300 K, and negative thermal expansion from 20-50 K can be observed. In comparison, synchrontron data have an upturn at 70 K upon cooling then reaches local maximum at 40 K and decrease again. Previous report<sup>136</sup> suggested the negative thermal expansion is associated with the position of Cu12e atoms. Inspired by this, we analyzed MD simulation trajectory to explain this phenomenon.

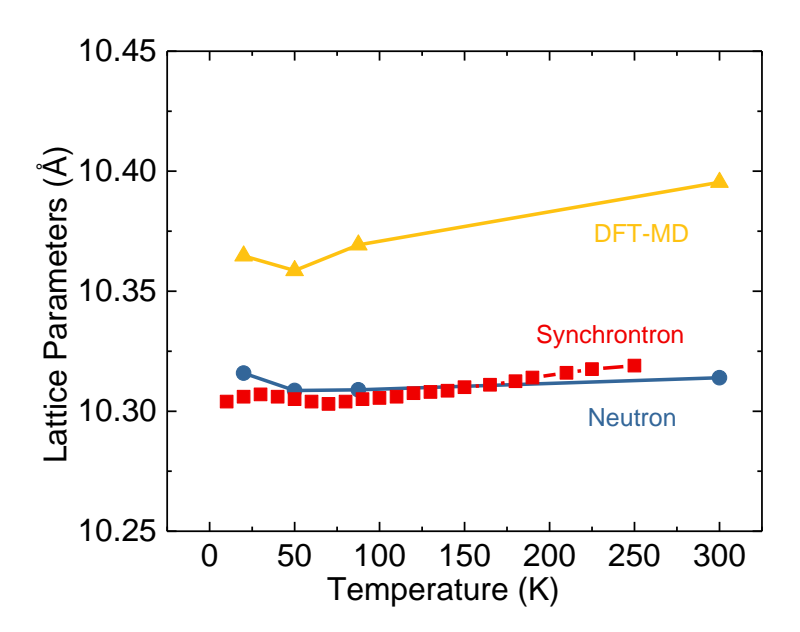


Figure 2.4: Lattice parameters of Cu<sub>12</sub>Sb<sub>4</sub>S<sub>13</sub> obtained by DFT-MD NPT simulation and neutron diffraction refinement. Lattice parameters proposed by Nasonova using synchrontron x-ray are shown here for comparison.

## 2.3.2 Sb-Cu 12e-Sb interaction

To gain the atomic insight of the negative thermal expansion and crystal structure of  $Cu_{12}Sb_4S_{13}$  at low temperature, we inspected the distance between each  $Cu_{12}e$  and the two coordinated Sb atoms as the schematic in Figure 2.5(a). According to our previous research<sup>39</sup>, the rattler atoms ( $Cu_{12}e$ ) are regulated by the nearby lone pair electron of Sb and responsible for the

interested anharmonic movement, and lead to low lattice thermal conductivity of Cu<sub>12</sub>Sb<sub>4</sub>S<sub>13</sub>. Here we plotted the one-pair-potentials (O.Pr.P) of Cu<sub>12</sub>e-Sb by converting the distribution of distance between those two atoms at 20 K and 300 K. At 20 K, a double-well shape (highlighted red in Figure 2.5(b)) can be identified for the Cu<sub>12</sub>e and Sb interaction energy, which indicated that the associated Cu<sub>12</sub>e atom is locked to one of the bonded Sb with average distance of 2.95 Å. 6 of total 12 Cu<sub>12</sub>e atoms in our unit cell appeared to be locked with bond order of 0.2169 based on the Density Derived Electrostatic and Chemical scheme<sup>151</sup> calculation, while the other 6 12e are rattling between two Sb atoms, as shown in Table 2.5. At both 20 and 300 K, the "symmetric" quartic shape (highlighted blue in Figure 2.5(b) and (c)) can be observed and suggesting that the associated Cu<sub>12</sub>e atom is rattling between two lone pair Sb. The number of locking and rattling Cu<sub>12</sub>e at different temperatures can also be found in Table 2.5. Locking 12e appeared when temperature went below MST temperature, and became more popular as temperature decrease. Notably, at 20 K, the distance between Cu<sub>12</sub>e and lone pair Sb is (3.17 Å) larger than the other cases, which could compensate the shrinkage of unit cell and lead to negative thermal expansion.

Table 2.5: Number of rattling and locking Cu 12e, Cu 12e -Sb bond order and bond distance for  $\text{Cu}_{12}\text{Sb}_4\text{S}_{13}$  at different temperatures.

	Number of	Number of	Locking Cu 12e - Sb	Cu 12e - lone pair Sb
	rattling Cu 12e	locking Cu 12e	bond order	distance (Å)
20K	6	6	0.2169	3.17
50K	7	5	0.1784	3.06
87.5K	10	2	0.1386	3.07
300K	12	0	No locking 12e (lone pair)	3.12



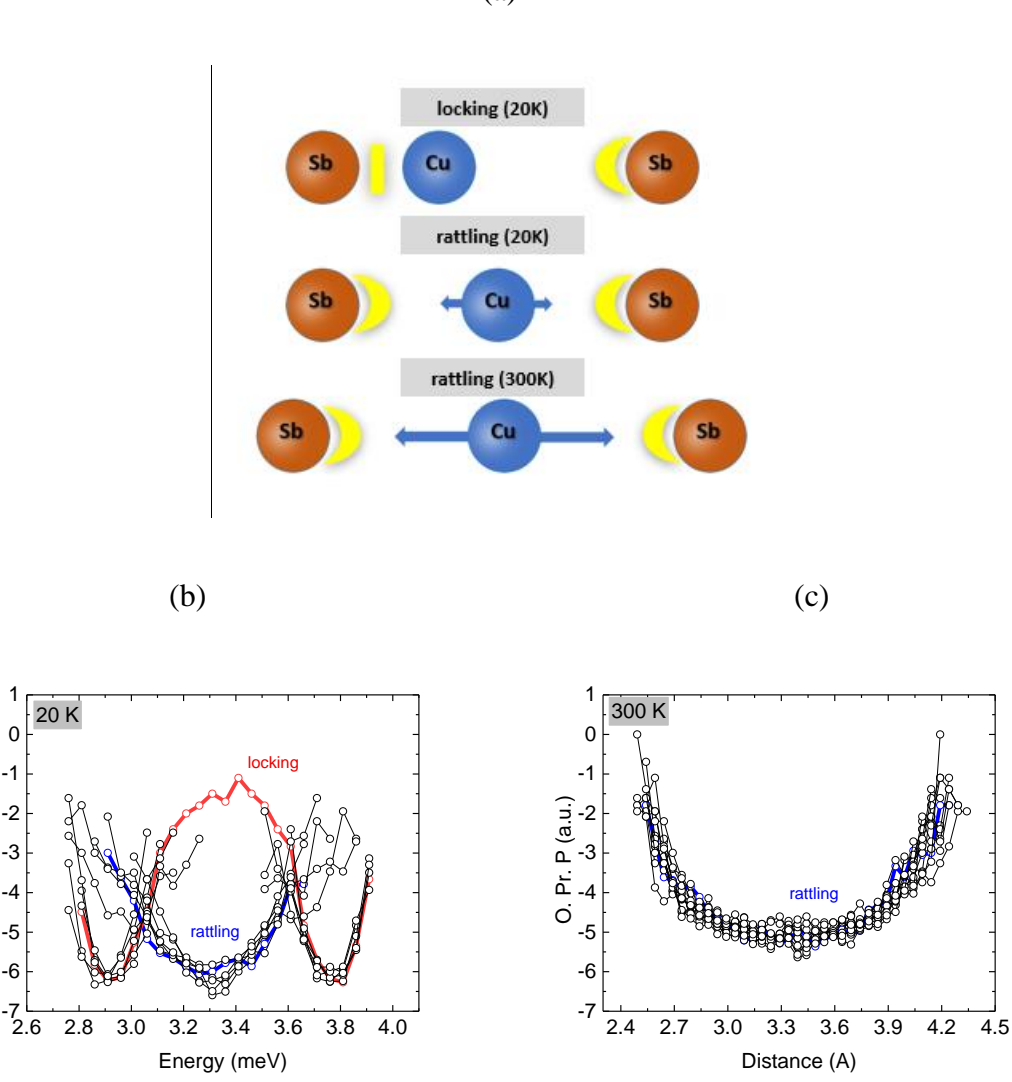


Figure 2.5: Schematic of Cu-Sb interaction at 20 K and 300 K (a) and potential energy landscape based on Sb-Cu12e-Sb cluster at (b) 20 K and (c) 300 K.

# 2.3.3 Vibrational Density of States

O. Pr. P (a.u.)

Calculated VDOS is derived from the Fourier transform of velocity autocorrelation function of atomic trajectories as following:

$$I_{vv}(\omega) = \int_0^\infty \left\langle \frac{1}{Nk_B T} \sum_{n=1}^N m_n v_n(0) \cdot v_n(t) \right\rangle \cos(\omega t) W(t) dt, \tag{22}$$

where  $m_n$  and  $v_n$  are the mass and velocity of nth atom, N the total number of atoms in the

group, and W(t) the Gaussian window function with a peak width of 1 meV<sup>152</sup>. Calculated partial vibrational density of states of each atomic group is presented in Figure 2.6. It is obvious that the low energy vibrational mode (~3 meV at 300 K), which is contributed by Cu12e atoms, is shifting to lower energy with decreasing temperature, i.e., phonon softening upon cooling<sup>138, 153-154</sup>. The observation is consistent with experimental INS data<sup>153</sup> and validate our simulation results.

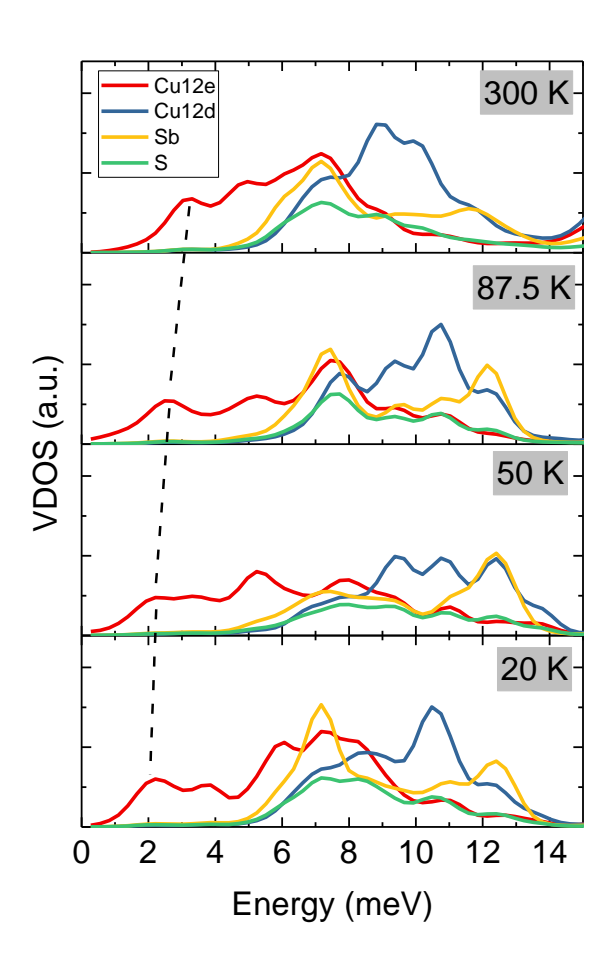


Figure 2.6: Partial vibration density of states (VDOS) of each atomic group for  $Cu_{12}Sb_4S_{13}$  at different temperatures.

# 2.3.4 Thermoelectric properties

Density of states (DOS) calculation of Cu<sub>12</sub>Sb<sub>4</sub>S<sub>13</sub> at different temperatures, is presented in

Figure 2.7. We used the average structure of NVE run as input structure for each temperature. At 300 K, the Fermi level  $E_F$  falls into top of valence bands with a sharp peak suggesting the degenerated p-type semiconductor feature of  $Cu_{12}Sb_4S_{13}$  with a bandgap of 1.30 eV, which is in good agreement with previous reports<sup>35, 40, 155-156</sup>. Overall feature do not vary a lot as temperature decreased, except that band gap energy slightly dropped from 1.30 eV to 1.25 eV.

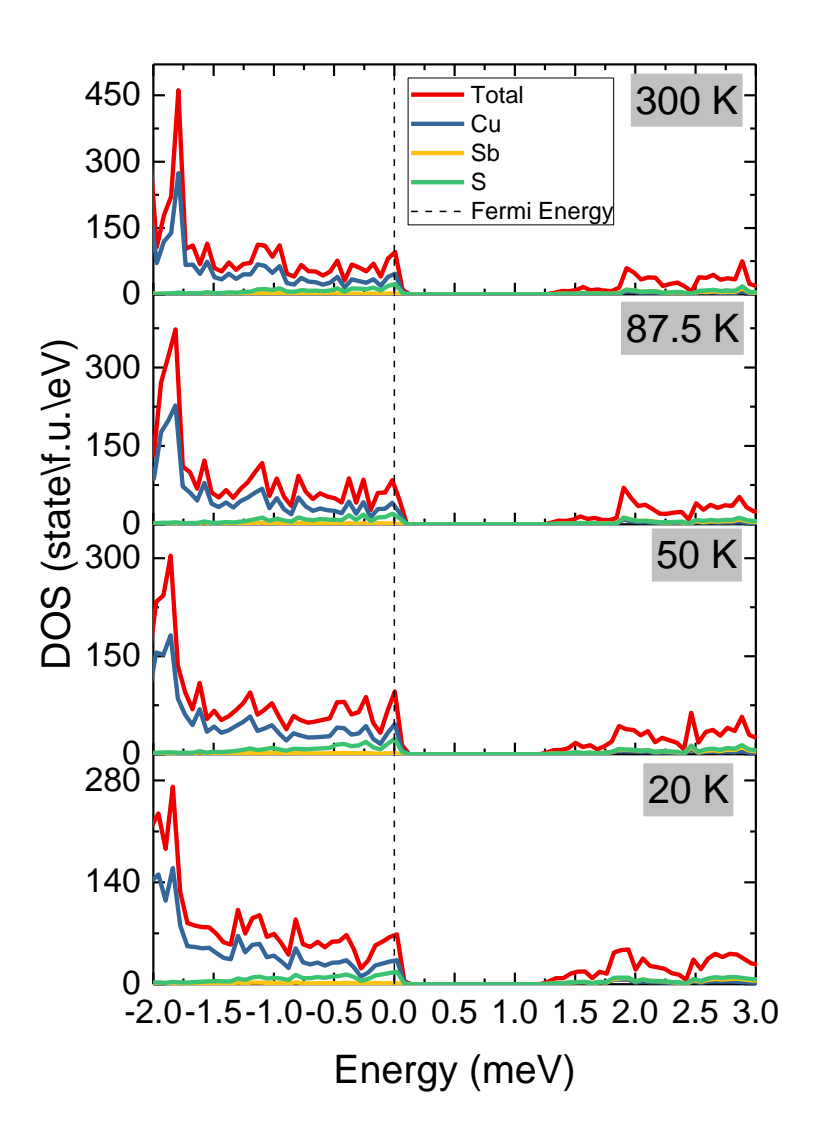


Figure 2.7: DOS calculation for Cu<sub>12</sub>Sb<sub>4</sub>S<sub>13</sub> and partial contribution from each atomic group at different temperatures. Fermi energy is marked by dashed line.

Thermoelectric properties of Cu<sub>12</sub>Sb<sub>4</sub>S<sub>13</sub> are calculated by Boltzwann transport equation implemented in *VASP*. In the system where an electric field E and temperature gradient  $\nabla T$  exist, current density J and the electronic heat current  $J_Q$  can be described as <sup>157-158</sup>

$$J = \sigma(E - S\nabla T), \tag{23}$$

$$J_Q = T\sigma SE - \kappa \nabla T, \tag{24}$$

where  $\sigma$  is electrical conductivity, S is Seebeck coefficient and  $\kappa$  is the thermal conductivity. Since we only take the electronic contribution part account for  $J_Q$ , electrical thermal conductivity  $\kappa_e$  here is defined as heat current per unit of temperature gradient in open circuit condition and can be expressed as:

$$\kappa_e = \kappa - S \sigma ST, \tag{25}$$

Based on the semiclassical transport theory using the Boltzmann transport equation presented by Pizzi et al<sup>146</sup>, the expression for tensors  $\sigma$ , S and  $\kappa$  can be described as a function of chemical potential  $\mu$  and temperature T:

$$[\sigma]_{ij}(\mu, T) = e^2 \int_{-\infty}^{+\infty} d\varepsilon \left( -\frac{\partial f(\varepsilon, \mu, T)}{\partial \varepsilon} \right) \sum_{ij} (\varepsilon), \tag{26}$$

$$[\sigma S]_{ij}(\mu, T) = \frac{e}{T} \int_{-\infty}^{+\infty} d\varepsilon \left( -\frac{\partial f(\varepsilon, \mu, T)}{\partial \varepsilon} \right) (\varepsilon - \mu) \sum_{ij} (\varepsilon), \tag{27}$$

$$[\kappa]_{ij}(\mu, T) = \frac{1}{T} \int_{-\infty}^{+\infty} d\varepsilon \left( -\frac{\partial f(\varepsilon, \mu, T)}{\partial \varepsilon} \right) (\varepsilon - \mu)^2 \sum_{ij} (\varepsilon), \tag{28}$$

where i and j are the Cartesian indice,  $f(\varepsilon, \mu, T)$  the usual Fermi-Dirac distribution function and  $\sum_{i,j}(\varepsilon)$  the transport distribution function (TDF).

In Figure 2.8(a), the temperature dependence of electrical resistivity has been showed. The calculated resistivity values from BoltzWann are roughly one order magnitude lower than the experimental data during the whole temperature range. Moreover, the MST showed in Nasonova's

study is unable to catch, despite discontinuity can be observed at 87.5 K. This result is in good agreement with our previous DOS calculation. This is possibly due to the limited ability of using PBE as XC functional in this calculation.

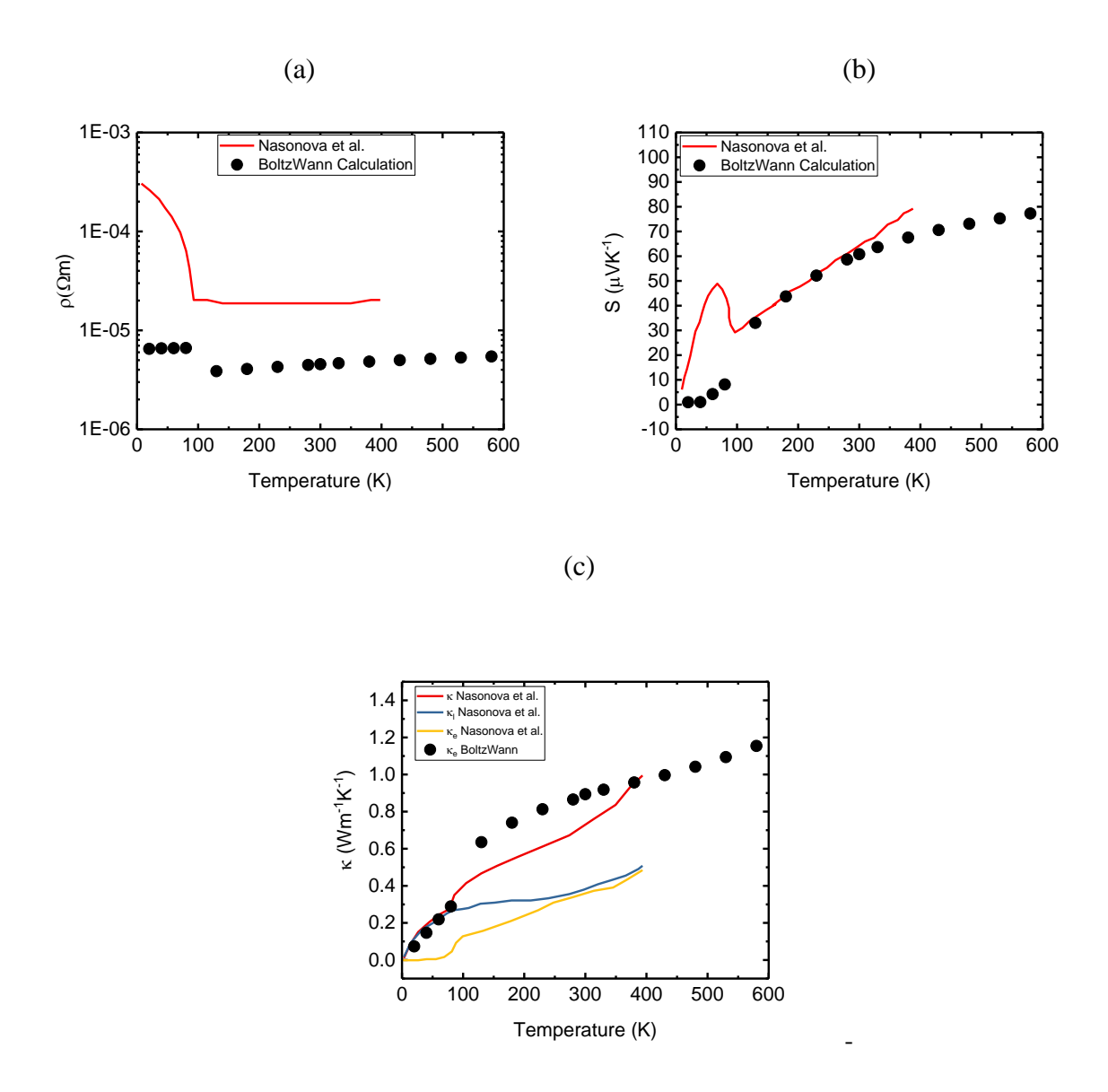


Figure 2.8: Temperature dependencies of calculated (a) electrical resistivity, (b) Seebeck coefficient and (c) electrical thermal conductivity for  $Cu_{12}Sb_4S_{13}$ . Experimental data from Nasonova el al.<sup>136</sup> are shown here for comparison.

Seebeck coefficient *S* from BoltzWann calculation have been shown in in Figure 2.8(b). S maintained positive at the whole temperature range, suggesting that holes are major carriers in this structure. In addition, S increased as temperature increased above MST temperature, which is another evidence of degenerate p-type semiconductor feature of Cu12Sb4S13. Comparing to experimental data, from MST temperature to 250 K, good agreement between simulation results and experimental values. Above 250 K, instead of keeping growing linearly, calculated data showed a decreased rate of growing and approached a plateau at high temperature range. Below MST temperature, computed data did not have the local maxima at 67 K however the abrupt increasement at MST temperature can be observed.

Thermal conductivity  $\kappa$  is composed of two parts, the lattice part  $\kappa_l$  and the electronic part  $\kappa_e$ . In the experimental data, there was an upturn at MST temperature for  $\kappa_e$ , which was contributed from the remarkable electrical conductivity of metal, and relatively smoother grow for  $\kappa_l$ . Here we obtained  $\kappa_e$  by applying Equation (25) as shown in Figure 2.8(c). The upturn at MST temperature can be identified, however, the absolute values were higher than the experimental data for the whole temperature range, due to the lower estimation of resistivity calculation.

#### 2.4 Conclusion

In this work, we examined the low-temperature structural properties of pristine tetrahedrite Cu<sub>12</sub>Sb<sub>4</sub>S<sub>13</sub> by neutron diffraction measurement, along with DFT-based molecular dynamics simulation. No evidence of the reported cubic-tetragonal phase transition occurred accompanied with MST from our experimental and computational results. Negative thermal expansion below 50 K can be observed, which we ascribed to the interaction between locking Cu*12e* and coordinated Sb atom. Density of states calculations by DFT did not reveal MST, but slightly bandgap reduction as temperature decreased can be observed. Moreover, we investigated the low

energy phonon vibrational mode which accounted for the anomalous phonon softening. We also calculated thermoelectric properties such as electrical resistivity, Seebeck coefficient and electronic thermal conductivity by BoltzWann code at low temperature and compared with experimental data. Further investigations are required to understand the origin of MST and the related properties of  $Cu_{12}Sb_4S_{13}$ .

## CHAPTER 3: Incoherent and coherent atomic dynamics of Cu<sub>10.5</sub>NiZn<sub>0.5</sub>Sb<sub>4</sub>S<sub>13</sub>

#### 3.1 Introduction

Previous study indicated that the transition metal dopants such as Ni, Zn, Fe and Mn, can improve the thermoelectric performance of tetrahedrites by adjusting electronic structure and reducing lattice thermal conductivity <sup>35-36</sup>. Previous experimental and computational studies found that the low thermal conductivity in tetrahedrites accompanied by anomalous atomic dynamics <sup>45, 152</sup>. One of the anomalous behaviors is the unusually large anisotropic displacement (ADP) of trigonal planar Cu12e atoms. Our previous study <sup>152</sup> indicated that the large ADP can be attributed to the Cu12e-Sb lone pair. Weak bonding between Cu12e and Sb leads to large vibration amplitude, results in the out-of-plane anharmonic rattling. The other type of anomalous behavior is called "phonon softening upon cooling", or stiffening upon heating, which can be observed by inelastic neutron scattering (INS) measurements. This behavior can be described as low-energy vibration mode energies decreased with the decreasing temperature. Although it has been argued that this phenomenon is also due to the dynamics of Cu12e atoms, the details remain unknown. This work will apply DFT-based MD simulation, along with inelastic neutron scattering (INS) experiment, to study the atomic mechanism of Cu<sub>10.5</sub>NiZn<sub>0.5</sub>Sb<sub>4</sub>S<sub>13</sub> tetrahedrites <sup>154</sup>.

## 3.2 Computational and experimental details

Ni-doped tetrahedrite with the composition Cu<sub>10.5</sub>NiZn<sub>0.5</sub>Sb<sub>4</sub>S<sub>13</sub> has been chosen as a candidate in this study. The synthesis method and condition can be found in Lu's previous work<sup>34</sup>. DFT-based MD simulation was performed with the *Vienne Ab initio Simulation Package* (VASP)<sup>143-144, 159-160</sup> employing the Projector Augmented-Wave (PAW) method<sup>161-162</sup>. GGA of PBE parametrization<sup>100</sup> was used for exchange-correlation functional. Simulation cell was 1 x 1 x 1 supercell with 58 atoms in total, while Ni and Zn are randomly distributed at Cu*12d* sties.

Valence configurations are 3p<sup>6</sup>4s<sup>1</sup>3d<sup>10</sup>, 4s<sup>1</sup>3d<sup>9</sup>, 4s<sup>2</sup>3d<sup>10</sup>, 5s<sup>2</sup>5p<sup>3</sup> and 3s<sup>2</sup>3p<sup>4</sup> for Cu, Ni, Zn, Sb and S respectively. First a constant number of particles, pressure and temperature (NPT) ensemble was implemented for 3 ps, with a Langevin thermostat and Parrinello-Rahman barostat, to obtain lattice parameters at various temperature. Next a constant number, volume, and energy (NVE) ensemble was performed for 5 ps for equilibration and followed by 20 ps production run for sampling atomic trajectories. Plane wave energy cutoff was 450 eV, with a gamma point K-mesh, and timestep was 1 fs.

INS of a powdered sample at 300 K were implemented by the wide Angular-Range Chopper Spectrometer (ARCS) at the Spallation Neutron Source of Oak Ridge National Laboratory, with incident neutron energy of 20 meV.

## 3.3 Results and discussion

# 3.3.1 Incoherent atomic dynamics of Cu<sub>10.5</sub>NiZn<sub>0.5</sub>Sb<sub>4</sub>S<sub>13</sub>

The calculated vibrational density of states (VDOS) is calculated from MD trajectory using the method as shown in Section 2.3.3, to compare the one extracted from INS measurement, as shown in Figure 3.1(a). VDOS from INS measurement is obtained by making the one-phonon incoherent scattering approximation<sup>163</sup>, with Debye-Waller factors from MD trajectories. The comparison indicates relatively reasonable agreement between computation and experiment, while the high energy portions difference is due to the one-phonon incoherent approximation. Figure 3.1(b) shows the partial VDOS spectra for each atom group. It is worth noting that a low energy peak exhibited at around 4 meV, which is predominately contributed by Cu*12e* atoms. This low energy vibration mode often suggests weak bonding and large-amplitude, and possibly suppresses the acoustic phonon branch, and leads to low thermal conductivity.

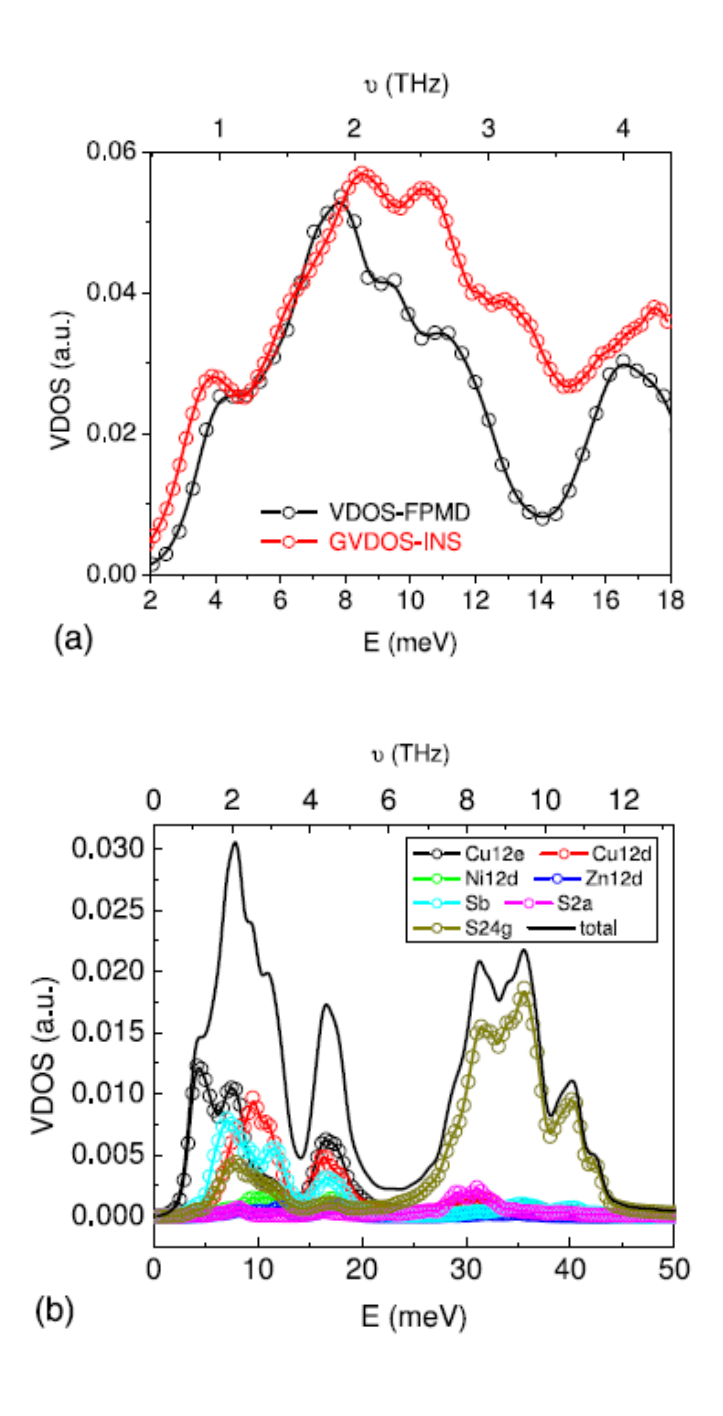


Figure 3.1: (a)Comparison of VDOS from MD simulation and INS experiment. (b) Partial VDOS for each atom group and total VDOS from MD simulation at 300K.

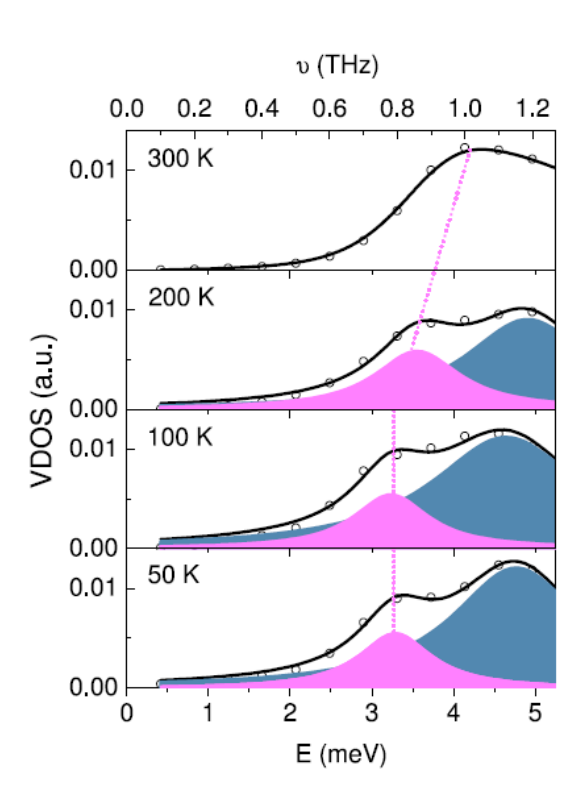


Figure 3.2: Partial VDOS of Cu12e atoms at different temperatures. Shape was fitted to sum of two Lorentzian functions.

Previous experimental INS data indicated that the low energy modes shifted to lower energies with lower temperature, i.e., phonon softening upon cooling, for Cu<sub>10</sub>Zn<sub>2</sub>Sb<sub>4</sub>S<sub>13</sub> and Cu<sub>10</sub>Zn<sub>2</sub>Sb<sub>2</sub>Te<sub>2</sub>S<sub>13</sub><sup>138, 153</sup>. To understand the mechanisms, we calculate partial VDOS for Cu<sub>12</sub>e atoms at different temperatures, as shown in Figure 3.2. Two peaks (at ~3.25 eV and ~4.8 eV) can be identified for 50 K, 100 K and 200 K, which can be fitted to the sum of two Lorentzian peaks. The first peak located at 3.25 eV for 50 K and 100 K, then shifted to higher energy as temperature increases, which is consistent with experimental INS data. Our previous work<sup>152</sup> suggested that the Sb lone pair electrons modulate the motion of Cu<sub>12</sub>e atom and lead to its anharmonic rattling. To visualize to interaction between Cu<sub>12</sub>e and Sb, we convert the distribution of distances to effective one-pair-potential (Figure 3.3(a) and 3.3(c)) and correlated to VDOS of Cu<sub>12</sub>e (Figure 3.3(b) and 3.3(d)). At 50 K, a double-well shape (highlighted red in Figure 3.3 (a)) can be identified

for the Cu and Sb interaction energy. This double-well shape is consistent with previous lattice dynamic calculation<sup>164</sup>, which indicates that the associated Cu12e atom is locked to one of the bonded Sb with average distance of 2.9 Å (Figure 3.3(e)). The Density Derived Electrostatic and Chemical (DDEC) scheme<sup>151</sup> calculation show that Cu12e - Sb bond order is 0.25, more like a bonding pair instead of lone pair. The certain Cu12e thus contributed to high vibrational energy of 5.5 meV as Figure 3.3(b). In addition, the "symmetric" quartic shape (highlighted blue in Figure 3.3 (b)) is also observed, which suggests that associated Cu12e is rattling between two lone pair Sb with average bond order of 0.1, and is responsible for the low vibrational energy of 3.25 meV. Then correlation at 300 K has been studied as Figure 3.3(c) and Figure 3.3(d). All Cu12e atoms at 300 K exhibit as rattlers and vibrational amplitude increased by additional thermal energy, thus results in higher vibrational energy, i.e., softening upon cooling.

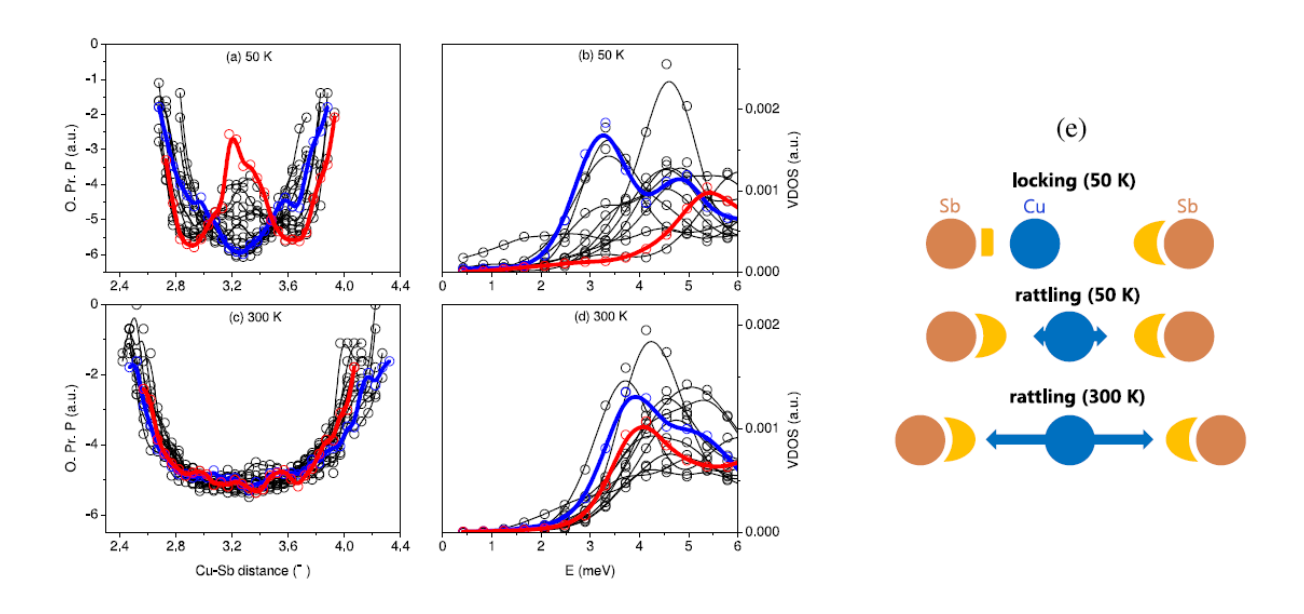


Figure 3.3: Potential energy landscape based on Sb-Cu12e-Sb cluster at 50 K (a) and 300 K (b), and correlated VDOS spectra of Cu12e at 50 K (c) and 300 K (d). Cu12e-Sb interaction are shown in (e).

# 3.3.2 Coherent atomic dynamics of Cu<sub>10.5</sub>NiZn<sub>0.5</sub>Sb<sub>4</sub>S<sub>13</sub>

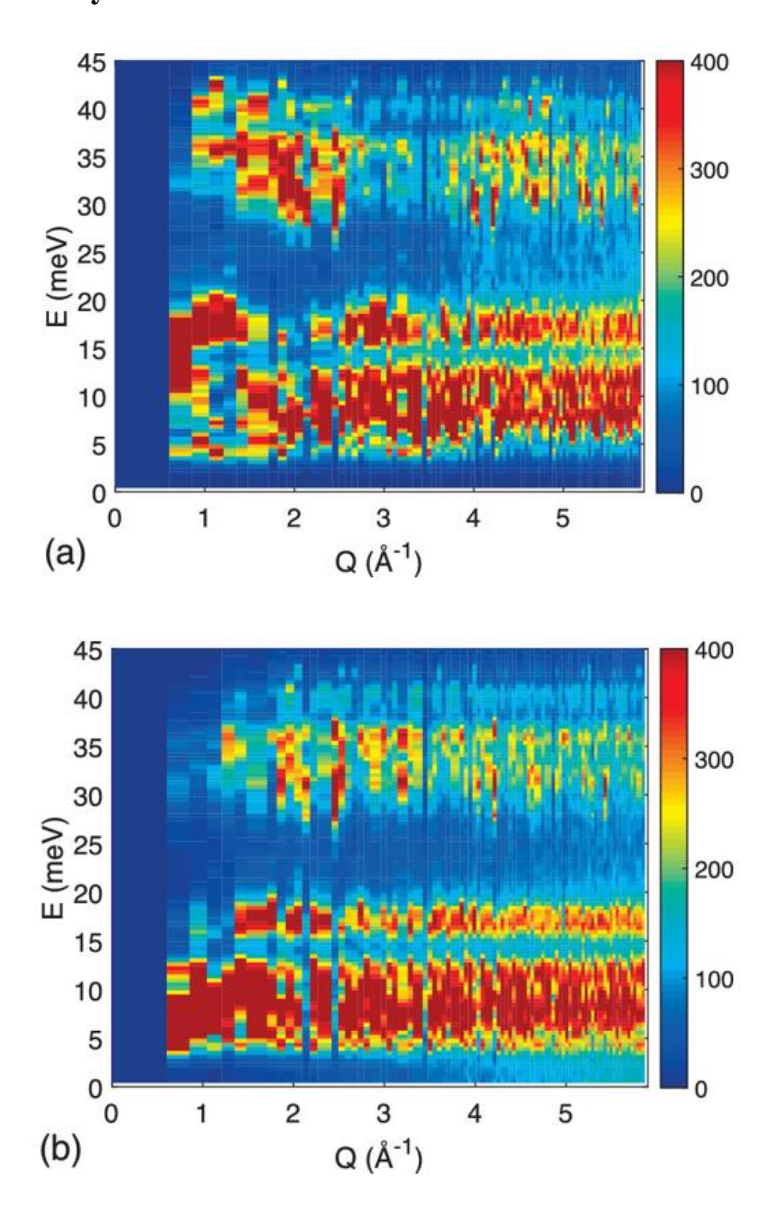


Figure 3.4: Calculated dynamic structure factors based on the momentum correlation function (a) longitudinal and (b) transverse direction.

Coherent atomic dynamics are also examined by computing the longitudinal and transverse dynamics structure factor based on the momentum correlation function, as shown in Figure 3.4. The minimum Q value in this work is  $0.6 \text{ Å}^{-1}$  due to the limited cell size. A clear optic band can be identified at ~ 4 meV. Because of the acoustic-optic interaction, i.e., "avoided crossing"  $^{165-166}$ ,

dispersive bands at ~10-20 meV/0.6-1.3 Å<sup>-1</sup> for longitudinal, ~5-10 meV/0.6-1.8 Å<sup>-1</sup> for transverse direction, are reminiscent of the optic branch. Although the acoustic branch of "avoided crossing" is not recognizable, which suggests that it is confined in a small dynamic region which is less than 4 meV and 0.6 Å<sup>-1</sup>. Therefore, we hypothesize that it's an evidence of phonon mean free path is close to the interatomic spacing and lead to low thermal conductivity. To validate the significance of the hypothesis semi-quantitatively, we obtaine a Debye temperature of 281 K and Debye heat capacity of 2.81 k<sub>B</sub>/atom at 300K. Although our Debye temperature is much higher than the value of 500 K from heat capacity studies<sup>167</sup>, our Debye heat capacity is comparable to the value of 2.75 k<sub>B</sub>/atom. In addition, the mean sound speed have been computed with the value of 2522 m/s, which is close to the sound speed of 2668 m/s in hydrodynamic region from bulk modulus<sup>168</sup>. Moreover, by making the approximation that the mean free path equals to the average interatomic spacing, we can obtain the thermal conductivity of 0.45 W m<sup>-1</sup> K<sup>-1</sup>, which is similar to the experimental value of 0.43 W m<sup>-1</sup> K<sup>-1</sup> <sup>34</sup>. The good agreements between our study and literatures provide the validation of previous hypothesis.

## 3.4 Summary

In this work we investigate the incoherent and coherent atomic dynamics of Cu<sub>10.5</sub>NiZn<sub>0.5</sub>Sb<sub>4</sub>S<sub>13</sub> tetrahedrite using first-principle molecular dynamics simulation. For the incoherent dynamics, the computed vibrational density of states is in good agreement with the experimental result from inelastic neutron diffraction data at 300 K. Detailed analysis of Cu motion inside the Sb[CuS<sub>3</sub>]Cu atomic cage indicates the reduction of anharmonic rattling of Cu between two Sb atoms upon cooling, which leads to anomalous phonon softening. For the coherent dynamics, the dynamic structure factors in the longitudinal and transverse direction suggest that the acoustic modes are confined in a small region of the scattering space, which accounts for the

small thermal conductivity measured. This study could further our understanding of the atomic

dynamics of tetrahedrite thermoelectrics and can more generally provide insight on how materials

can be designed at the atomic level to possess intrinsically low lattice thermal conductivity, an

important parameter for not only thermoelectrics but also other applications such as thermal barrier

coatings.

This work was published on APL Materials 4.10 (2016):104811.

https://doi.org/10.1063/1.4959961

54

## CHAPTER 4: Mobile Cu movement in Cu-rich tetrahedrite Cu<sub>14</sub>Sb<sub>4</sub>S<sub>13</sub>

## 4.1 Introduction

The Cu-Sb-Cu phase diagram indicated that tetrahedrite composition varies from Cu<sub>12</sub>Sb<sub>4</sub>S<sub>13</sub> to Cu<sub>14</sub>Sb<sub>4</sub>S<sub>13</sub> depending on temperature<sup>169</sup>. Tetrahedrites with more than 12 Cu, i.e., Cu-rich tetrahedrite, had better thermoelectric performance than the pristine cell according to previous study by Vaqueiro et al<sup>170</sup>. The thermoelectric figure of merit *zT* for Cu<sub>14</sub>Sb<sub>4</sub>S<sub>13</sub> reached ~ 0.6 at 573 K, which was similar to reported substituted tetrahedrites Cu<sub>11</sub>Zn<sub>1</sub>Sb<sub>4</sub>S<sub>13</sub><sup>164</sup> and Cu<sub>12</sub>Sb<sub>3</sub>TeS<sub>13</sub><sup>41</sup>. Vaqueiro also suggested that, for Cu-rich tetrahedrites, Cu becomes mobile above 393 K and are likely to be superionic conductors, while the excess Cu atoms were likely to be at Cu24*g* sites. However, the insight of how Cu atoms distribute and move remains unknown. Inspired by the previous work, it is interesting to investigate the details of mobile Cu movement, with the help of DFT-based MD simulation using a Cu-rich tetrahedrite Cu<sub>14</sub>Sb<sub>4</sub>S<sub>13</sub> as a model.

To help us understanding the local environment of different Cu sites and possible Cu diffusion pathways, we manually put extra Cu atoms into a stoichiometric Cu<sub>12</sub>Sb<sub>4</sub>S<sub>13</sub> cell (I-43m) and make Cu24g sites fully occupied with the composition of Cu<sub>14</sub>Sb<sub>4</sub>S<sub>13</sub>, using a three-dimensional visualization software VESTA<sup>37</sup>. The initial crystal structure and representative unit around Cu24g are shown in Figure 4.1 and Figure 4.2. Three distinct Cu sites can be identified, as Cu12d, Cu12e and Cu24g site. The local environment of Cu12d and Cu12e have been discussed in Section 1.2.3, while the additional Cu24g are bonded to three S atoms and encompassed with two Cu12d and two Cu12e atoms. From the crystal structure of Cu<sub>14</sub>Sb<sub>4</sub>S<sub>13</sub>, it is reasonable to hypothesize that mobile Cu atom may move inside the structure by jumping between 12d, 12e and 24g sites.

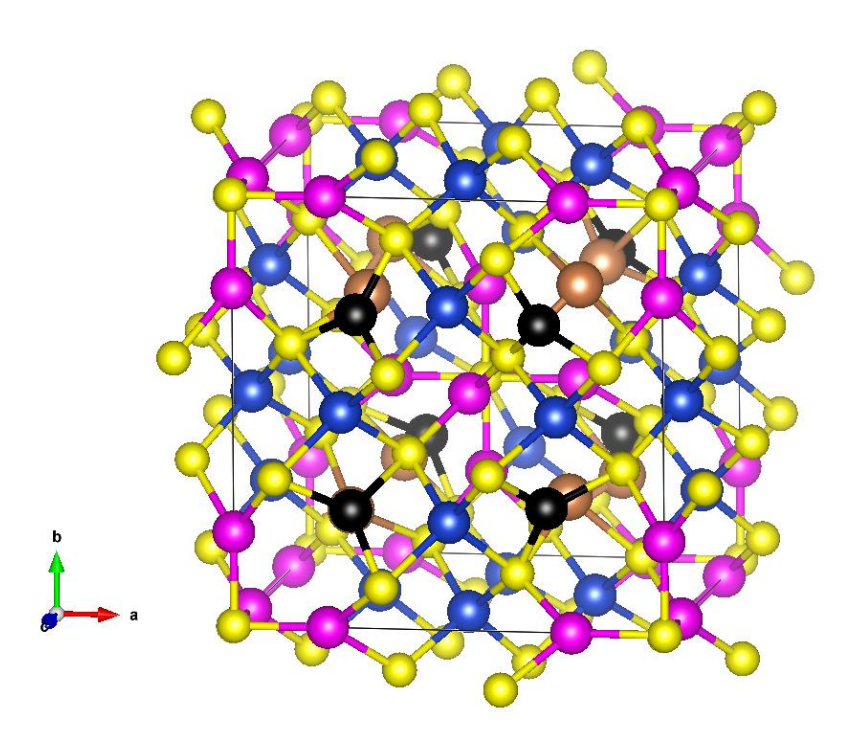


Figure 4.1: Initial crystal structure of Cu-rich tetrahedrite Cu<sub>14</sub>Sb<sub>4</sub>S<sub>13</sub> with three distinct Cu sites. Cu24g atoms are displayed as black.

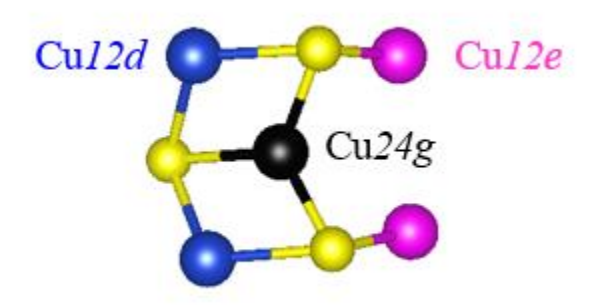


Figure 4.2: Cu24g local environment for better visualization.

# 4.2 Computational details

Cu-rich tetrahedrite  $Cu_{14}Sb_4S_{13}$  has been chosen as the model structure in the study, and excess Cu atoms are distributed in  $Cu_{24g}$  sites based on previous research <sup>155, 170-171</sup>. Simulation setups are the same as Section 3.2, except that PBE-D3<sup>172</sup> is used as exchange-correlation functional with 2x2x2 K-points mesh. NVE production simulation time is increased to 40 ps in

this case. Simulation temperature is chosen to be 700 K, since Cu-rich tetrahedrite will collapse into a single phase above  $\sim 500$  K based on the neutron diffraction data<sup>170</sup>.

# 4.3 Results and discussion

# **4.3.1** Lattice parameters

Lattice parameter obtained from NPT simulation is 10.3972 Å at 700 K, comparing to 10.4924 Å at 673 K from literature. Regarding that PBE-D3 method usually underestimates lattice parameters for about 4%, the difference is considered to be acceptable <sup>173</sup>. Lattice fluctuation during NPT can be observed as Figure 4.3. The relatively large fluctuation suggested the structural instability, which we ascribe to the mobile Cu atoms movement inside the cell.

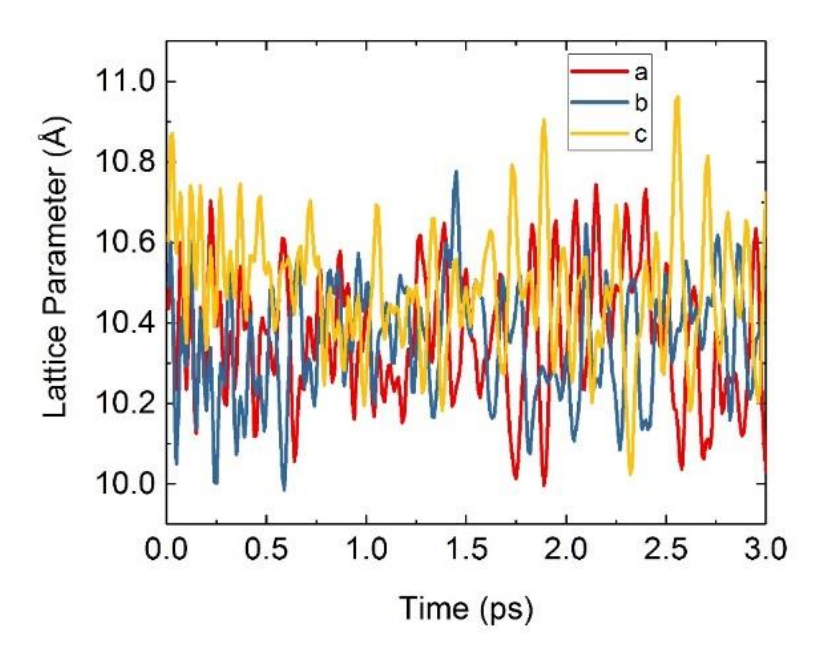


Figure 4.3: Lattice parameters (a, b, c) as function of time in NPT simulation.

## 4.3.2 Incoherent density correlation and Cu self-diffusivity

Here we use incoherent density correlation  $(I_{inc,\alpha}(Q,t))$  to investigate the diffusivity of Cu-rich tetrahedrite.  $I_{inc,\alpha}(Q,t)$  is calculated from MD trajectory for each Q value<sup>107</sup>, with correlation time of 35 ps as following:

$$I_{inc,\alpha}(Q,t) = \frac{1}{N_{\alpha}} \langle \sum_{n=1}^{N_{\alpha}} e^{jQ \cdot r_n^{\alpha}(0)} e^{-jQ \cdot r_n^{\alpha}(t)} \rangle.$$
 (29)

where  $\alpha$  is the atomic specie,  $N_{\alpha}$  the number of  $\alpha$  atoms, Q the wave vector and  $r_n^{\alpha}(t)$  the position of nth atom at time t.  $I_{inc,\alpha}(Q,t)$  of diffusing species will exhibit a clear decay to 0 (ideally), while the vibrating ones will show rapid decay and then non-zero plateau. Simulation cell have 28 Cu atoms in total. After examining the shape of calculated  $I_{inc,\alpha}(Q,t)$  for each Cu atom, these Cu atoms can be divided into two group: vibrating Cu and diffusing Cu. Then  $I_{inc,\alpha}(Q,t)$  of all vibrating Cu are summed and averaged, as well as the diffusing group, as shown in Figure 4.4, where only three smallest Q values are inlouded. Ignoring the first 5 ps, where atoms are undergoing ballistic collision and other short-time dynamics, the decay of diffusing Cu group  $I_{inc,\alpha}(Q,t)$  plot can be described as a stretched exponential function  $I^{174}$ :

$$I_{inc,\alpha}(Q,t) = A * \exp\left(-\Gamma^{KWW}Q(t)^{\beta(Q)}\right),\tag{30}$$

where A is scaling factor,  $1/\Gamma^{KWW}$  is the relaxation time and  $\beta$  is stretching parameter.  $\Gamma$  vs.  $Q^2$  plot is shown in Figure 4.5, a linear dependence of  $\Gamma$  with  $Q^2$  ( $\Gamma = D$   $Q^2$ ) is characteristic of continuous random walk translational diffusion, i.e., Fickian diffusion, where the slope D is self-diffusion constant<sup>107</sup>. In addition to applying Fickian diffusion model to describe the continuous random walk translational diffusion at low Q range, the broadening of  $\Gamma$  with  $Q^2$  reached a plateau asymptotically at higher Q, indicating a typical jump-diffusion process, and can be described as

the Singwi-Sjölander (SS) jump model<sup>175-176</sup> in which diffusion occurs via jump diffusion where residence time  $\tau$  is much longer than the required jump time. SS model can be expressed by

$$\Gamma^{SS}(Q) = \frac{1}{\tau} \frac{Q^2 \langle r^2 \rangle / 6}{1 + Q^2 \langle r^2 \rangle / 6'} \tag{31}$$

where  $\tau$  is the residence time and  $\langle r^2 \rangle$  the mean square jump distance. At low Q value SS model reduces to Fickian model with  $D = \langle r^2 \rangle / 6\tau$  and jump length  $l = \sqrt{\langle r^2 \rangle}$ . Cu diffusivity obtained from Fickian model and SS model yield 4.8961 x  $10^{-6}$  cm<sup>2</sup>/s and 1.0 x  $10^{-5}$  cm<sup>2</sup>/s, respectively. Residence time and mean jump length can be extracted by SS model fit, with values of 0.9885 ps and 0.9947 Å, resepectively.

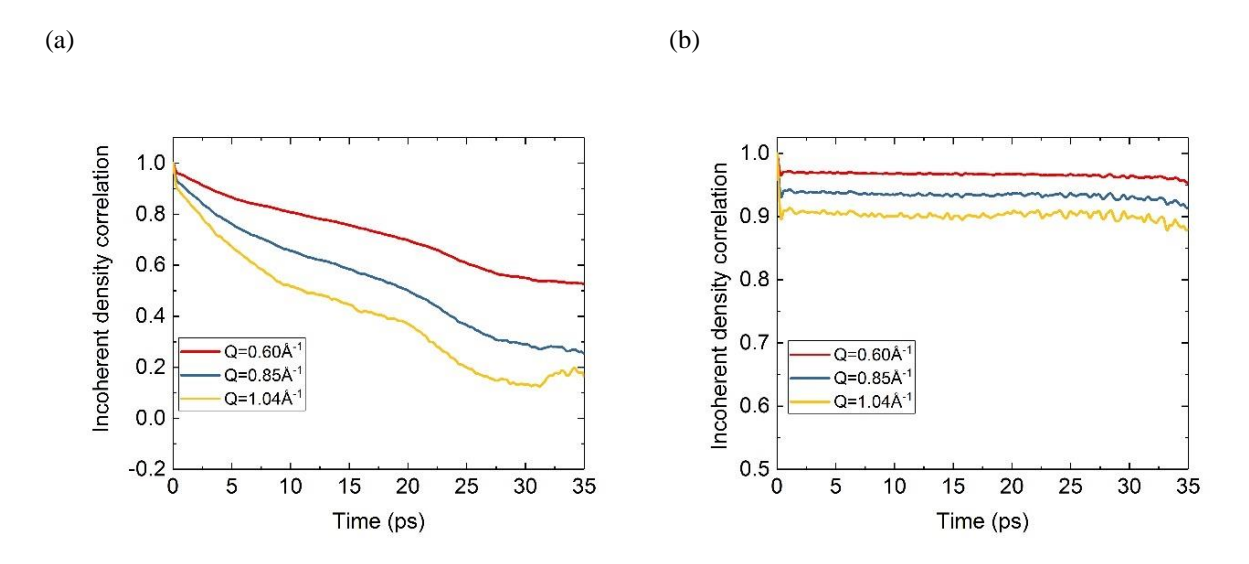


Figure 4.4: Incoherent density correlation for (a) diffusing Cu atoms and (b) vibrating Cu atoms for three small Q values.

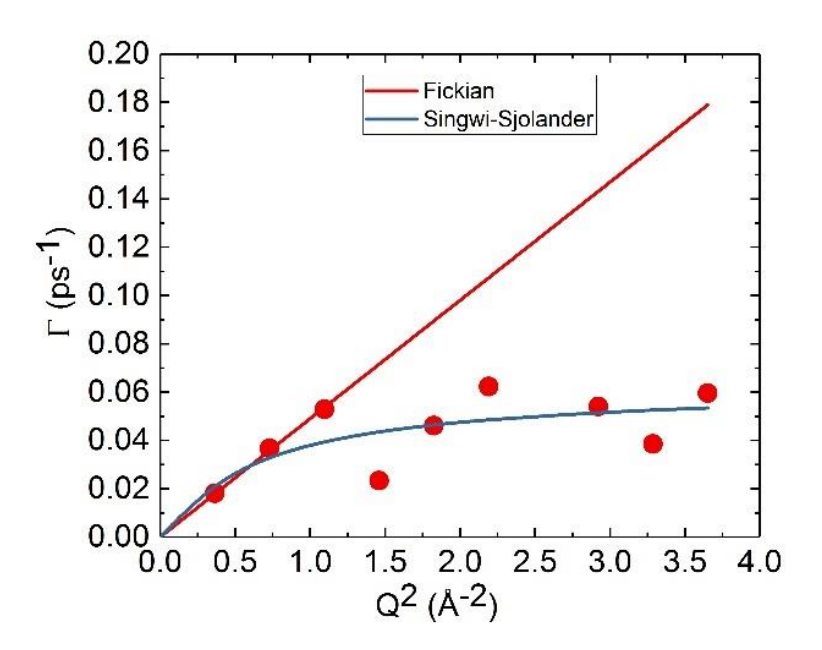


Figure 4.5: HWHM ( $\Gamma$ ) as a function of  $Q^2$ . Red line is fitted to Fickian model and blue line is fitted to Singwi-Sjolander model.

# 4.3.3 Cu nuclear density map

Although the quantitatively incoherent density correlation analysis offered useful information including Cu self-diffusivity, physical details such as the distribution and movement of Cu atoms remain unknown. Nuclear density map enables the visualization of atom distribution by dividing the cell into cubic pixels of roughly 0.1 Å in length, then calculate the probability density of each type of atom in each pixel<sup>177</sup>. Figure 4.6 was generated by VESTA, showing the density maps of representative units of diffusing pathways. Isosurface level is determined to be 0.12 Å<sup>-3</sup> for better visualization. From the nuclear density map, various diffusion paths for Cu atoms can be identified. For example, a diffusion path between 12d site and 24g site can be observed as Figure 4.6(a), the intermediate site could be a 48g site. We also noticed that Cu atom can jump from a 12d cage to another 12d cage, without taking a 12e or 24g site as intermediate

transition (Figure 4.6(b)). In addition, Cu atom can diffuse between 12e site and 24g site back and forth (Figure 4.6(c)). No nuclear density was identified between Cu12d and Cu12e sites, which means a direct jump between these two sites is not favorable for Cu atoms in this case. It is noticeable that one of the Cu12d sites is never accessed by Cu atom during the whole simulation time (40 ps in total). We think that might due to the finite transport ability of Cu at 700 K, or limited statistics by using 1x1x1 simulation cell and 40 ps simulation time. Moreover, identified diffusion paths with the participation of atoms in Cu12d and Cu24g sites are much more than the paths including Cu12e atoms, suggesting that Cu atoms are stable at Cu12e sites, which is interesting considering the weak bonding of Cu12e – Sb inside Sb[CuS3]Sb cage, and need to be further investigated.

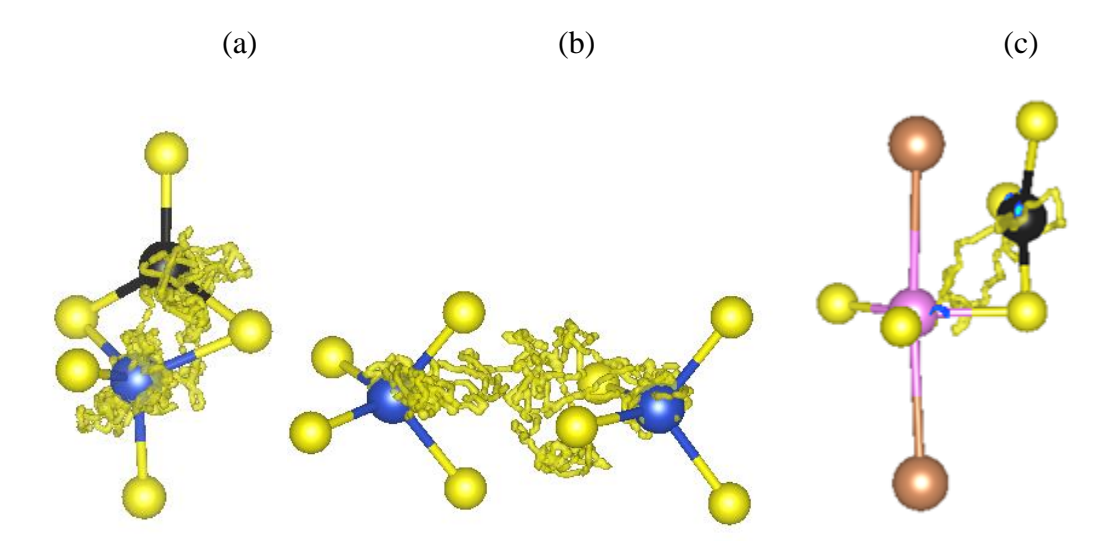


Figure 4.6: Nuclear density may of Cu atom showing the diffusion pathway: (a) 12d - 24g path; (b) 12d - 12d path; (c) 12e - 24g path. Brown atom is Sb and yellow is S. Isosurface level of 0.12 Å<sup>-3</sup>.

# 4.3.4 Energy barriers

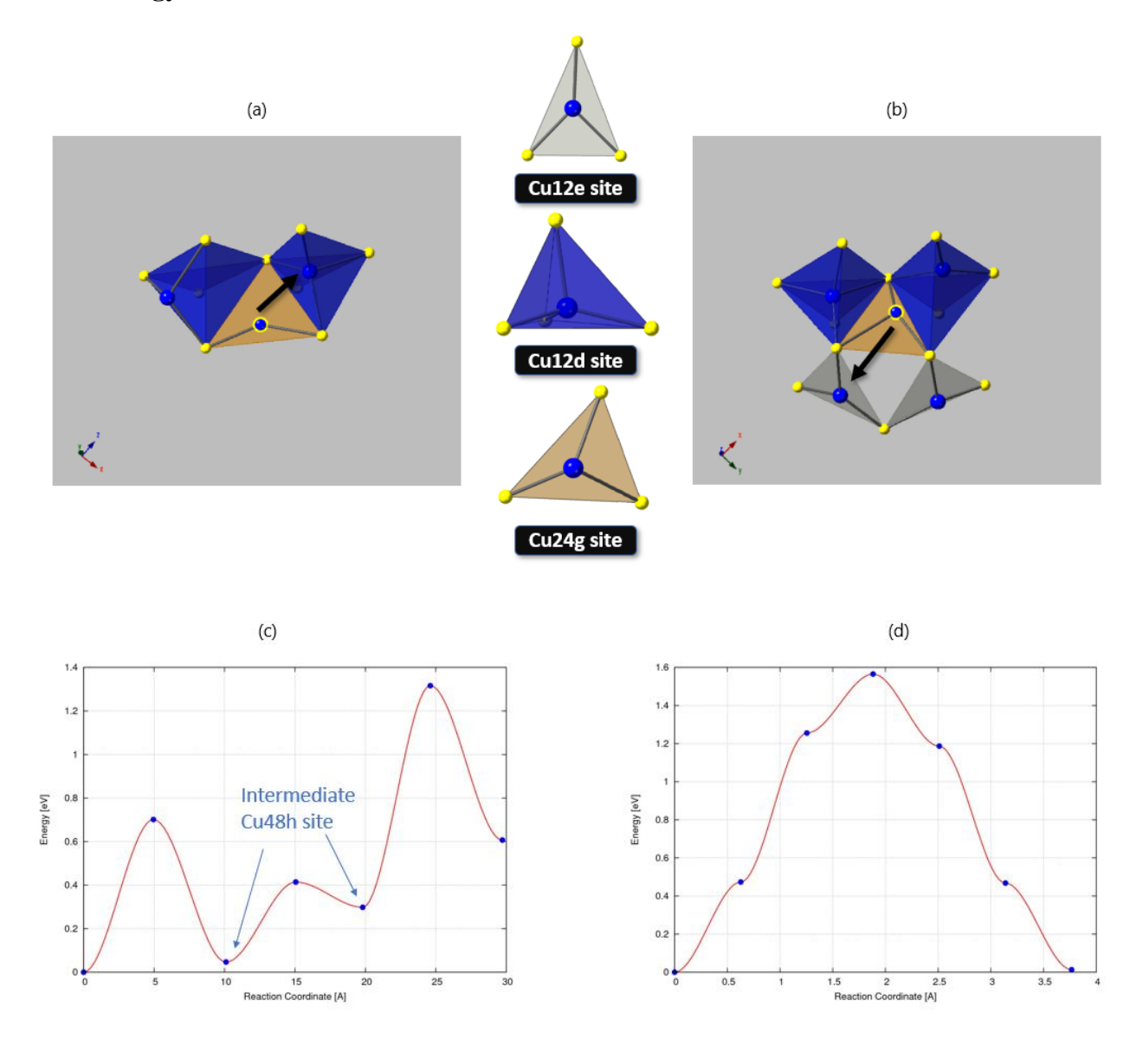


Figure 4.7: Diffusion paths schematic of (a) 24g - 12d and (b) 24g - 12e extracted from the actual MD trajectory and migration energy barriers of (c) 24g - 12d and (d) 24g - 12e from NEB calculations.

In order to estimate the migration energy barriers of different migration paths, here we applied "nudged elastic band" (NEB)<sup>178-180</sup> methods as programmed in the *VASP* package, using 5 images between each metastable configuration. Two diffusion paths, 24g - 12d and 24g - 12e

are selected as examples for comparison. The initial states and final states are chosen among our MD trajectory, instead of manually creating vacancies, which leads to better estimation of the real case. Zero of energy is chosen as the initial state energy. Figure 4.7 (a) and (b), obtained by  $CrystalMaker^{181}$ , reveal the schematic of those two diffusion paths, where only part of the crystal cell are shown for better visulization. Figure 4.7 (c) displays the migration energy diagram of 24g - 12d, with migration energy barrier  $E_m$  of 1.32 eV, where two intermediate local minimums (corresponding to Cu48h sties) can be observed. Whereas,  $E_m$  of 24g - 12e is estimated to be 1.56 eV as displayed in Figure 4.7 (d), which is higher than the 24g - 12d case, indicating the 24g - 12d diffusion pathway is energetically preferable than 24g - 12e. This result is in good agreement with the above density map analysis that less diffusion paths involving 12e atoms can be observed.

# 4.4 Summary

In this chapter we discussed the Cu ion transport properties of copper-rich tetrahedrite  $Cu_{14}Sb_4S_{13}$  with the help of DFT-based MD. Large fluctuation of lattice parameter from NPT indicated the structural instability during the simulation. By investigating the shape of incoherent density correlation  $I_{inc,\alpha}(Q,t)$  at 700 K, we can conclude that some Cu atoms remain vibrating while the other become mobile by diffusing among different Cu sites. Diffusivity, residence time and mean square jump length of mobile Cu atoms can be extract by fitting simulation data to Fickian model and SS model. The nuclear density map is also examined to visualize the motion of Cu atoms at different sites.  $Cu_{12d}$  and  $Cu_{24g}$  tend to be more mobile than Cu in 12e sites within the simulation. Future study with larger cell and longer simulation time will be needed to confirm this. Moreover, several diffusion paths can be identified, including direct jump between two 12d sites. "Nudged elastic band" (NEB) calculation is applied to estimate the migration energy barriers  $E_m$  for 24g - 12d and 24g - 12e diffusion paths, with the values of 1.32 eV and 1.56 eV,

respectively. Further study of nonstoichiometric tetrahedrite as potential ionic conductor will be interesting, including optimization of Cu-rich composition and experimental validation of the transport properties such as Cu self-diffusivity, ionic conductivity and activation energy.

# CHAPTER 5: Density-functional theory based molecular dynamics simulation of tetrahedrite thermoelectrics: effect of cell size and basis sets

#### **5.1 Introduction**

With the advancement of hardware and software infrastructure, computational modeling has become an indispensable tool in materials research, often in parallel with experimental effort. Among different modeling methods, density-functional theory (DFT) in the Kohn-Sham approach<sup>182</sup> has been widely used in the investigation of chemicals, hard materials, and soft matter. Although DFT calculations are considered as first-principles methods they are not option free, as the size of simulation cell, basis sets for the wavefunction, exchange-correlation (XC) functional, etc. must be selected first. While there are many studies on the effect of XC functionals, e.g. the recent study by Tran et al. 183, the examination of cell size is rare due to the computational overhead associated with the increase of atoms/electrons. One of the size studies by Spiekermann et al. 184 suggested different trends, e.g. water release for a 192-atom cell and water uptake for a 96-atom cell of supercritical H<sub>2</sub>O-SiO<sub>2</sub> fluids, pointing to a finite size effect. In terms of basis sets, plane waves (PW) and atomic orbitals (AO) are two popular choices. Recently, Miceli et al. 185 compared the structural, dynamic, and electronic properties of liquid water using both AO and PW basis sets and found good agreement on results from two sets. Ulian et al. 186 also compared PW and AO basis sets using Mg<sub>3</sub>Si<sub>4</sub>O<sub>10</sub>(OH)<sub>2</sub> layer silicate and found both basis sets adequately describe the geometry, energy, and infrared spectra.

Inspired by these studies, in this work we report our investigation of effect of cell size and basis set on results from DFT-based first-principles molecular dynamics simulation of a thermoelectric material:  $Cu_{10}Zn_2Sb_4S_{13}$  tetrahedrite. Tetrahedrite materials with a general composition of  $Cu_{12-x}M_xSb_4S_{13}$  where M is a metal dopant have emerged recently as promising

thermoelectric candidates due to their elemental abundance, environmental friendliness, favorable electronic properties, and most importantly low lattice thermal conductivity (< 1 W m<sup>-1</sup> K<sup>-1</sup> for a wide temperature range)<sup>164, 187</sup>. While this group of materials has been the subject of several DFT calculations<sup>34, 42, 164, 188-192</sup>, the effect of calculation "parameters" such as cell size and basis set remains elusive. We selected two cell sizes (1x1x1 and 2x2x2) and two basis sets (PW and AO) and compared simulation results from three simulations (1x1x1 PW, 1x1x1 AO, and 2x2x2 AO) and with experiments.

# 5.2 Computational and experimental details

Vienna Ab initio Simulation Package (VASP)<sup>193-196</sup> code employing the Projector Augmented-Wave (PAW) method<sup>197-198</sup> and Quickstep code<sup>199</sup> implemented in cp2k<sup>200</sup> are employed as DFT packages using PW and AO basis sets, respectively. In VASP, valence electron configurations for Cu, Zn, Sb, S atoms are 4s<sup>1</sup>3d<sup>10</sup>, 4s<sup>2</sup>3d<sup>10</sup>, 5s<sup>2</sup>5p<sup>3</sup>, and 3s<sup>2</sup>3p<sup>4</sup>, respectively. The plane wave energy cutoff was 450 eV. In Quickstep, the mixed Gaussian and plane wave (GPW) method, i.e. Gaussian basis sets for orbitals with auxiliary plane waves for electron density, was used. Valence electron configurations were the same as in VASP but with Godecker–Tetter–Hutter (GTH) norm-conserving pseudo potentials<sup>201-202</sup>. The plane wave cutoff was 1200 Ry and the atomic orbital (Gaussian) basis sets were molecular optimized double zeta-valence basis sets with a polarization function (DZVP)<sup>203</sup>. In both cases, the generalized gradient approximation (GGA) with Perdew-Burke-Ernzerhof (PBE) parametrization<sup>204,205</sup> was used for the XC functional and a single Gamma point was used for the k-mesh. Two sizes of simulation cells, 1x1x1 (58 atoms) and 2x2x2 (464 atoms) were used based on the crystal structure of tetrahedrite (I-43m) with Zn randomly distributed at Cu12d sites. We chose 1x1x1 cell to compare AO and PW basis sets and

AO basis set to compare 1x1x1 and 2x2x2 cells. Due to the exorbitant computational cost, we did not use the 2x2x2 cell and PW combination.

For MD simulation, first a constant number of particles, pressure and temperature (NPT) ensemble at 300 K and zero pressure was implemented for 3 ps for 1x1x1 cells in order to obtain the lattice parameters. The Langevin thermostat (friction coefficient of 50 and 1 ps<sup>-1</sup> for atoms and lattice) and Parrinello and Rahman barostat (lattice mass of 10 a.m.u.) was used in *VASP*, while a Nose thermostat (time constant of 0.1 ps) and Martyna-Tuckerman-Tobias-Klein (MTTK) barostat<sup>206</sup> (time constant of 0.5 ps) was used in Quickstep. Next a constant number, volume, energy (NVE) ensemble was performed for 5 ps for equilibration and 20 ps for production at 300 K, while in NVE there is no temperature correction was made. The time step was 1 fs for both NPT and NVE runs.

Synthesis of  $Cu_{10}Zn_2Sb_4S_{13}$  powder was performed by mechanical alloying as described in the literature<sup>51</sup>. Cu K-edge X-ray absorption experiments were performed at the 4-3 beamline of Stanford Synchrotron Radiation Laboratory. We used the software SIXPack<sup>207</sup> to average raw data files out of three absorption scans and employed the software Athena<sup>208</sup> to extract the EXAFS signal.

## 5.3 Results and discussion

#### **5.3.1** Average structure

Average structure of  $Cu_{10}Zn_2Sb_4S_{13}$  after 1x1x1 PW NVE simulation is shown in Figure 5.1. Two distinct Cu sites can be identified, as  $Cu_{12d}$  and  $Cu_{12e}$ .  $Cu_{12d}$  atom coordinated by four S atoms and form a tetrahedron, while  $Cu_{12e}$  atom surrounded by three S atoms and form a triangular planar coordination. All the Zn dopants located in  $Cu_{12d}$  sites.

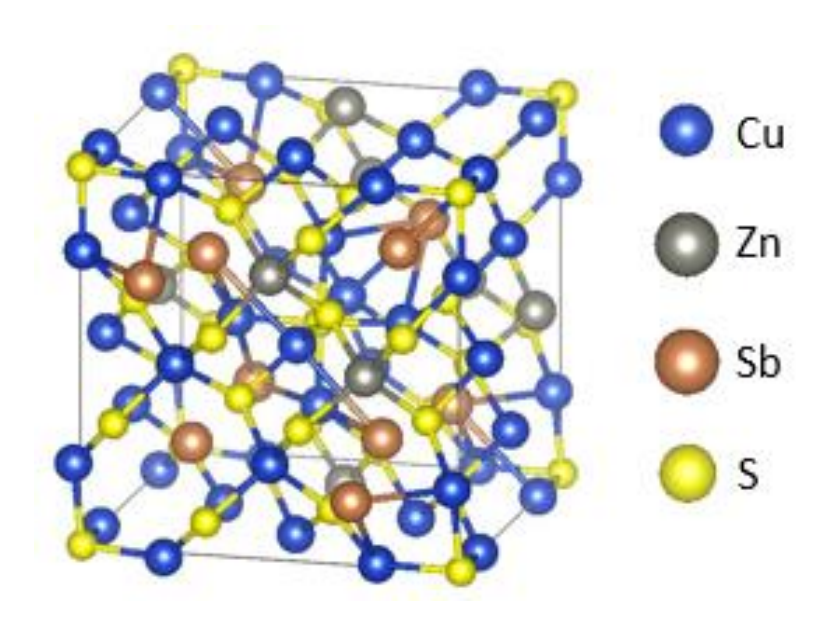


Figure 5.1: Average structure after 1x1x1 PW NVE simulation showing the crystal structure of  $Cu_{10}Zn_2Sb_4S_{13}$ .

# **5.3.2** Lattice parameters

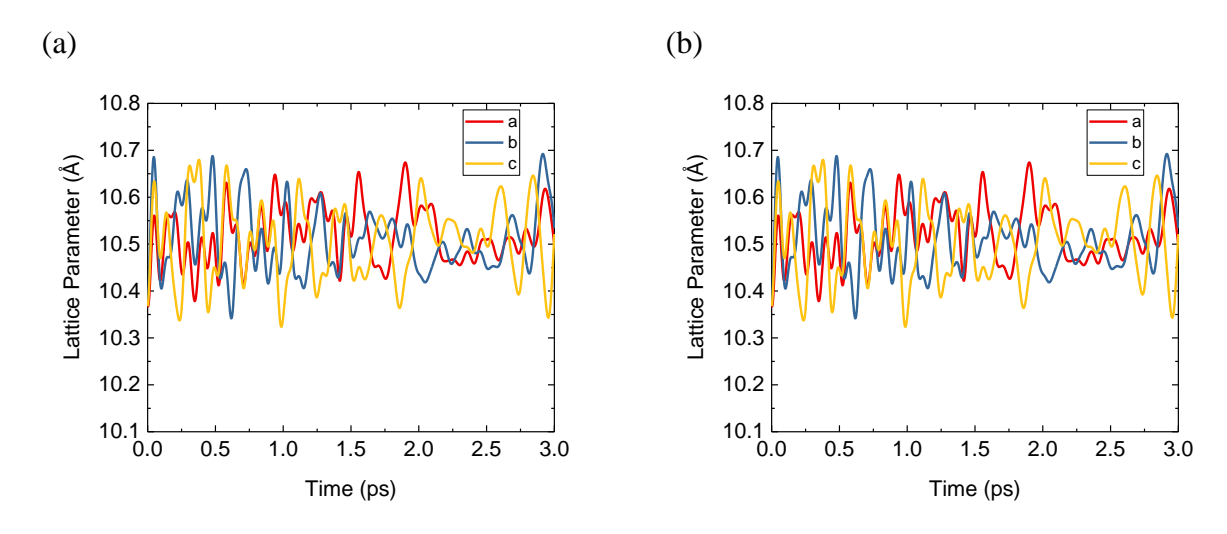


Figure 5.2: Lattice parameters (a, b, c) of (a) 1x1x1 PW and (b) 1x1x1 AO cell as a function of time in NPT simulation.

Lattice parameters (a, b, c) from the NPT ensemble of 1x1x1 PW and 1x1x1 AO simulations at 300 K are shown in Figure 3.1. It can be seen both simulations suggest a cubic structure. The average cubic lattice parameters are  $10.4692 \pm 0.135$  Å and  $10.5113 \pm 0.073$  Å, respectively. They are close to each other within the standard deviation. They are both higher than the literature value of 10.3833 Å<sup>209</sup>, as the PBE XC functional tends to overestimate lattice parameters for various materials<sup>183</sup>. We took the lattice parameter of 2x2x2 AO cell as double of 1x1x1 AO cell.

# **5.3.3** Vibrational density of states

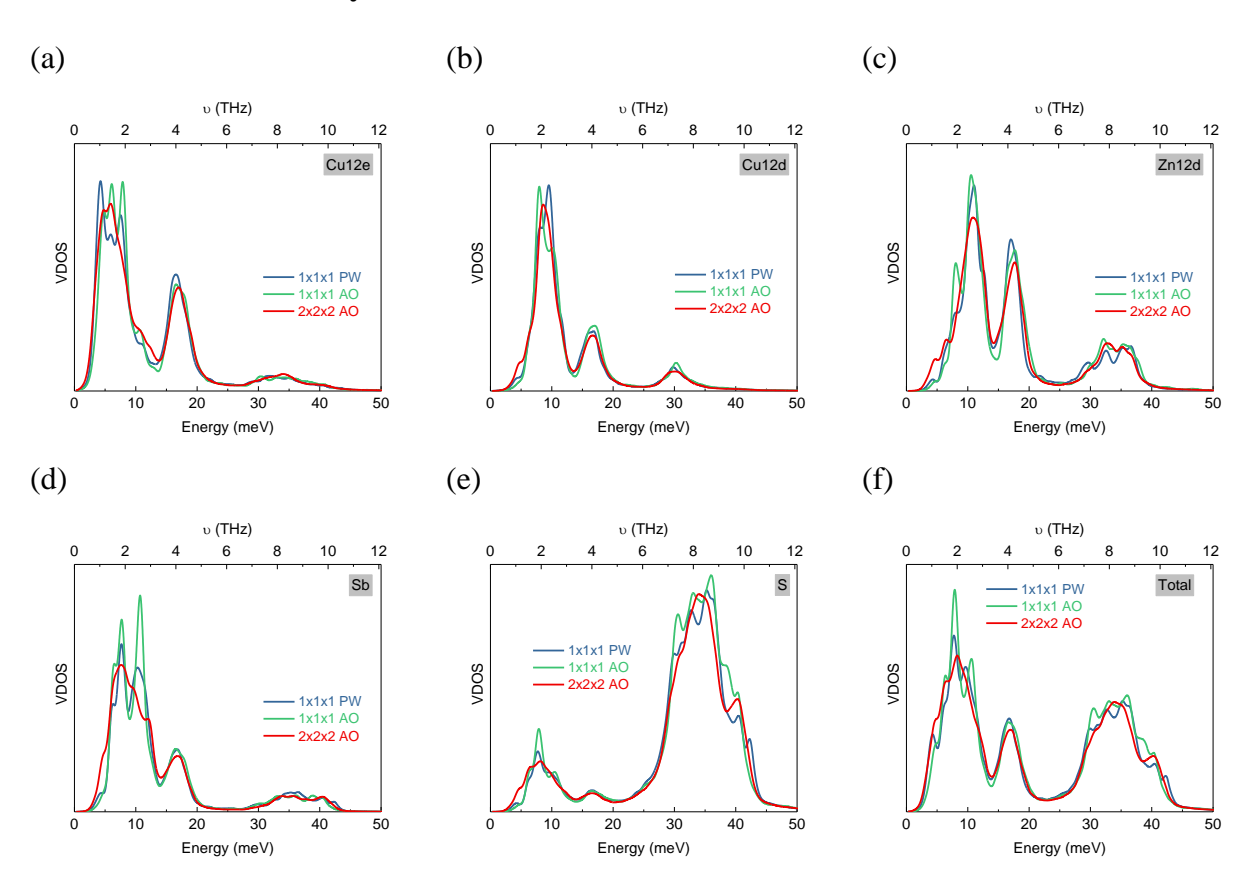


Figure 5.3: Partial and total vibrational density of states (VDOS) of each atom group (a-e: Cu12e, Cu12d, Zn12d, Sb, and S; f: total) for three simulations (1x1x1 PW, 1x1x1 AO, and 2x2x2 AO).

We investigated the effect of cell size and basis set on vibrational density of states (VDOS),

which can be extracted from the atomic trajectory as discussed in Section 2.3.3. The partial VDOS (a-e) of each atom group, Cu12e, Cu12d, Zn12d, Sb, and S and total VDOS (f) are shown in Figure 5.3. The 12e and 12d sites are trigonal planar and tetrahedral positions, respectively. In Figure 5.3(a), the vibration of Cu12e shows three peaks (~4.2, 5.9, 7.5 meV) at the low-energy portion with the first peak being strongest for 1x1x1 PW simulation, while 1x1x1 AO simulation has three peaks (~4.8, 6.1, 7.8 meV) with the second and third peaks almost equal in intensity. If we compare 1x1x1 AO and 2x2x2 AO simulations, we can see the peak at 7.8 meV from the former decays into a shoulder in the latter. The similar observation was made for other atom groups (b-e) and the total group (f). We think that different basis sets cause slightly different electronic structures and atomic forces, leading to slight variation in vibrational properties. On the other hand, larger cells allow more atoms and vibrational modes to be sampled, which effectively broaden the peaks.

Under the harmonic approximation, the vibrational energy is connected to the total VDOS as the following:

$$U(E = \hbar\omega, T) = \frac{\int_0^\infty \frac{E}{[exp(E/(k_BT)) - 1]} I_{vv}^{total}(E) dE}{\int_0^\infty I_{vv}^{total}(E) dE},$$
(32)

from which heat capacity can be computed. The constant-volume heat capacity per atom for three simulations is shown in Figure 5.4. Heat capacities of three simulations are close to each other at all temperatures and approach  $3k_B$  at high temperature according to the Dulong-Petit law. In the meantime, experimental data for the same compound measured by Lara-Curzio et al.<sup>210</sup> and for a similar composition  $Cu_{10.5}Zn_{1.5}Sb_4S_{13}$  measured by Lu et al.<sup>164</sup> are also included in Figure 5.4. Experimental values agree well with computed ones. It is worth noting that we assume the total VDOS (obtained from 300 K, i.e. Figure 5.3(f)) stay the same for the entire computed range,  $0 - 10.5 Cm_1 = 1.00 Cm_2 = 1.00 Cm_2$ 

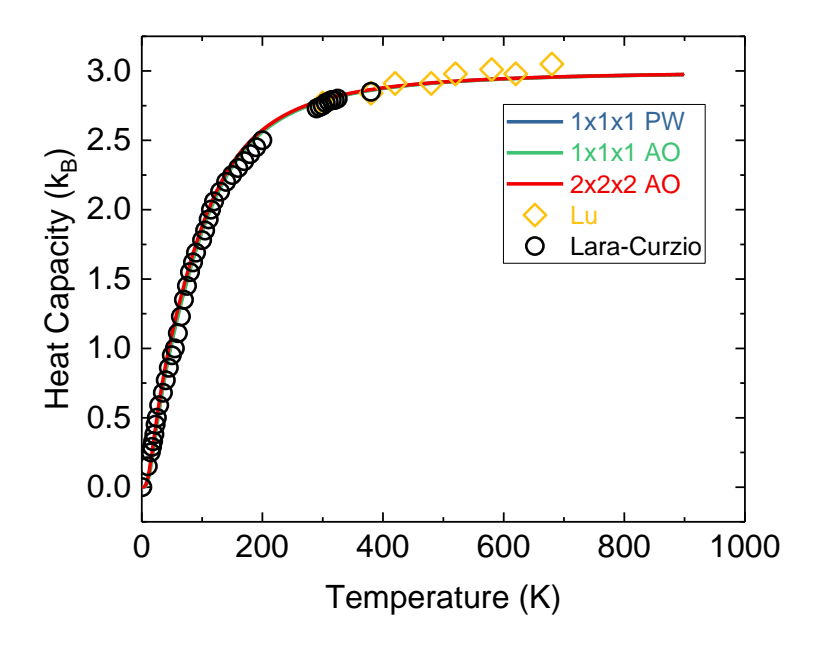


Figure 5.4: Heat capacity per atom for three simulations (1x1x1 PW, 1x1x1 AO, and 2x2x2 AO). Experimental data from Lu et al.<sup>7</sup> and Lara-Curzio et al.<sup>33</sup> are also shown for comparison.

## **5.3.4 Phonon dispersion**

In addition to VDOS, we also examined the effect of cell size and basis set on phonon dispersion by comparing the *Q*-resolved coherent velocity correlation. For the coherent velocity

$$J(Q,t) = \sum_{n=1}^{N} v_n(t), \tag{33}$$

where N is the total number of atoms, the longitudinal (L) and transverse (T) correlation can be calculated as the following:

$$C^{L}(Q,t) = \frac{1}{Q^{2}} \langle (Q \cdot J(Q,0))(Q \cdot J(-Q,t)) \rangle, \tag{34}$$

$$C^{T}(Q,t) = \frac{1}{2Q^{2}} \langle \left( Q \times J(Q,0) \right) \cdot \left( Q \times J(-Q,t) \right) \rangle. \tag{35}$$

The allowed Q vectors are based on the simulation cell as  $n_1a_1^* + n_2a_2^* + n_3a_3^*$  where  $a^*$  are the

reciprocal lattice vectors and n are integers. While the larger cell size of 2x2x2 AO simulation enables smaller Q value to be studied, we picked two smallest values that are common to all three simulations (0.60 and 0.84 Å<sup>-1</sup>) and plotted the longitudinal and transverse response in Figure 5.5. Similar to what we observed for VDOS in Figure 5.3, results from three simulations are comparable but not identical. Examples of notable deviations include the large intensity difference of transverse peak at ~2 THz in Figure 5.5(b) and of longitudinal peak at ~40 meV in Figure 5.5(c).

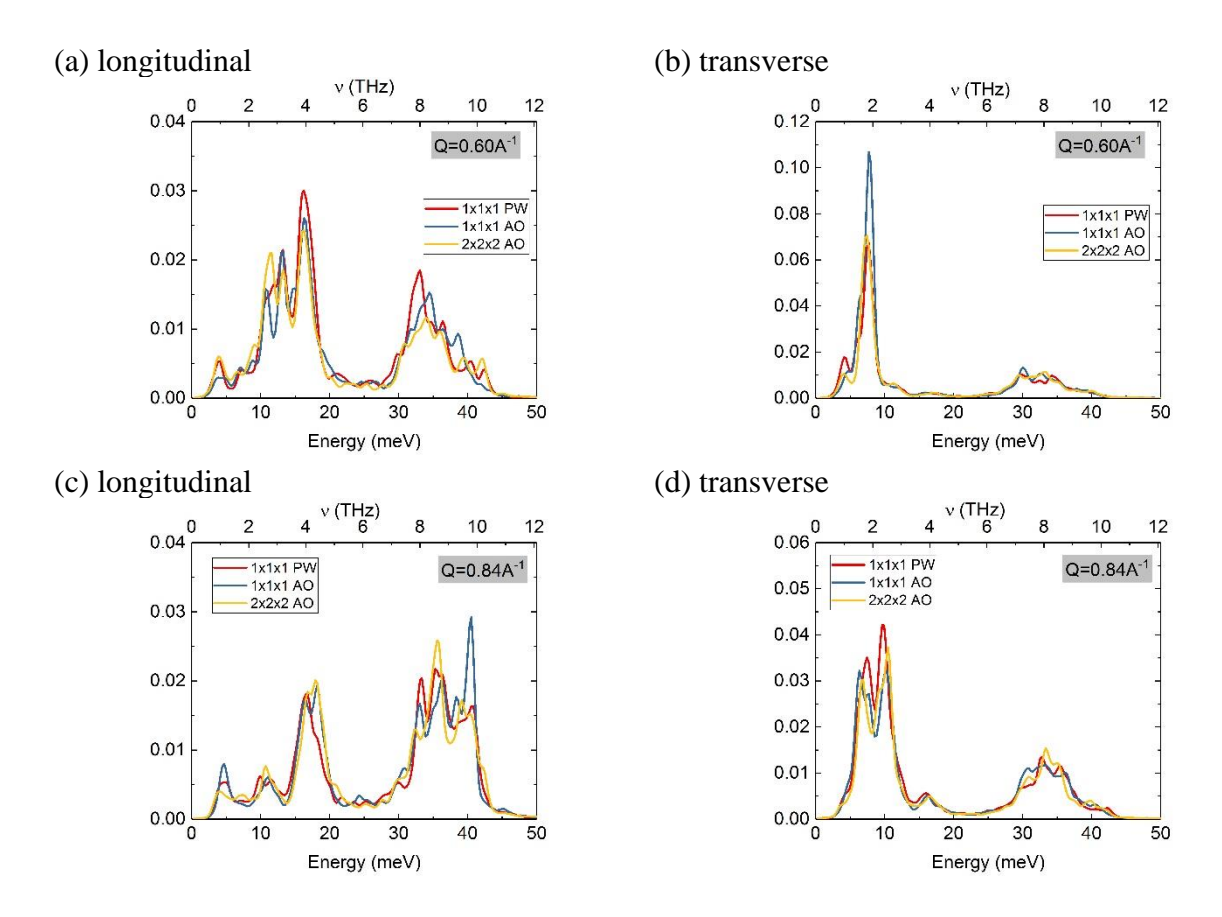


Figure 5.5: Longitudinal phonon dispersion for (a) Q=0.60 A<sup>-1</sup>, (c) Q=0.84 A<sup>-1</sup> and transverse phonon dispersion for (b) Q=0.60 A<sup>-1</sup>, (d) Q=0.84 A<sup>-1</sup>.

# 5.3.5 EXAFS spectra

Extended X-ray Absorption Fine Structure (EXAFS) experiments are often applied to study the local structure around an atomic species. In this work we will also compare Cu edge EXAFS

spectra from computation and experiment. Computationally, the EXAFS spectrum was obtained from configuration averaging of atomic trajectory. Briefly, we selected 1 frame for every 10 fs of the trajectory to have a total of 2,000 frames. In each frame, we defined an atomic cluster around each Cu atom (20 in total) with a 5 Å radius and employed the software FEFF9<sup>211</sup> to calculate the EXAFS spectrum. We averaged over all selected frames and all Cu atoms in each frame and plotted the result in Figure 5.6. Similar to the heat capacity plot in Figure 5.4, results from three simulations are close to each other. The peak position difference between computation and experiment in Figure 5.6 is likely caused by the difference in lattice parameter, i.e. Section 5.3.2, as these peak positions are related to specific bond lengths.

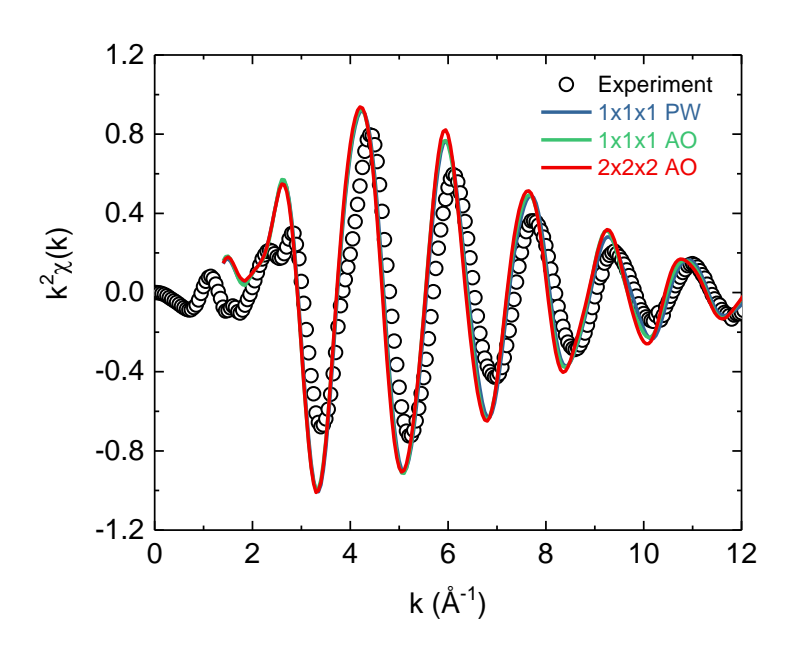


Figure 5.6: k²-weighted Cu EXAFS spectrum obtained by experiment (black circle) and simulations (solid lines).

## 5.3.6 2x2x2 AO Simulation

The low Q values accessible only to the 2x2x2 cell allow us to examine the region closer

to the hydrodynamic limit of atomic dynamics, where useful materials properties could be extracted<sup>212</sup>. First, we could study sound speeds by examining the longitudinal and transverse momentum correlation. They have the same expression as in Eq. (27) but with the expression as:

$$J(Q,t) = \sum_{n=1}^{N} m_n v_n(t). \tag{36}$$

Longitudinal and transverse response of coherent momentum correlation with three smallest Q values corresponding to the 2x2x2 cell are shown in Figure 5.7. In the longitudinal case, the strongest peak of each curve is moving to higher energy with increasing Q. We hypothesize that this peak corresponds to the longitudinal sound mode and plot its energy as a function of Q in Figure 5.7(c). A linear fit through the origin yields a longitudinal sound speed  $v_{s,L}$  of 3945 m/s. For the transverse response, two peaks can be observed and we ascribe them to transverse sound modes in Figure 5.7(b), with the Q dependence of peak position shown in Figure 5.7(c). It is possible that the two smallest Q are in the linear dispersion region but we only used slopes between the origin and smallest Q to obtain sound speeds of 1805 and 2186 m/s. We took the average of these two, 1995 m/s, as the transverse sound speed  $v_{s,T}$ . Sound speeds in cubic crystals are related to elastic properties such as shear (G) and bulk (B) modulus as the following:

$$v_{s,T} = \sqrt{C_{44}/\rho}, v_{s,L} = \sqrt{C_{11}/\rho}, C_{44} = G, C_{11} = B + 4G/3,$$
 (37)

where  $\rho$  is the mass density,  $C_{11}$  and  $C_{44}$  the elastic constants. The density from our 2x2x2 AO simulation is 4.77 g/cm<sup>3</sup>, while literature values range from 4.67 to 5.05 g/cm<sup>3</sup> due to sample variation<sup>168</sup>. Our calculated shear and bulk modulus are 19.0 GPa and 48.9 GPa, respectively, which are similar to experimental values of 19.1 – 23.0 GPa and 46.3 – 56.3 GPa<sup>168</sup>.

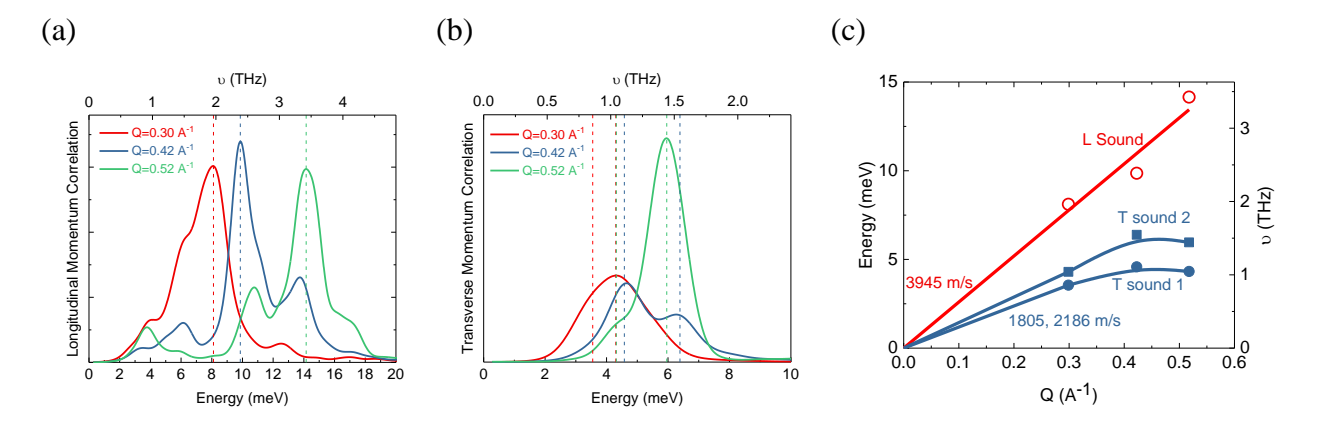


Figure 5.7: Longitudinal (a) and transverse (b) response of the momentum correlation. (c) Dispersion of longitudinal (L) and transverse (T) sound modes. Peak energy for each Q value (red dots: longitudinal; blue dots: transverse) and their linear regression have been shown.

Second, this larger cell also enables the identification of acoustic modes in phonon dispersion. Similar to Figure 5.5, longitudinal and transverse response of coherent velocity correlation with three smallest Q values corresponding to the 2x2x2 cell are shown in Figure 5.8. It is immediately recognizable that coherent momentum (Figure 5.7) and coherent velocity (Figure 5.8) responses are similar at these Q values. This is not surprising as it is expected that mass variation from different species in a multicomponent material will only have small influence at the hydrodynamic limit, i.e. the material behaving as a single component material with effective mass. The closeness of elastic properties between experiment and computation leads us to assign the strongest peak in Figure 5.8(a) as the longitudinal acoustic (LA) mode. In addition, positions of two shoulder peaks ahead of the LA peak,  $\sim$  4 and 6 meV, do not vary significantly with Q so we described them as quasi-localized (QL) modes with optic character. Such pre-LA peaks show up as Boson peaks in VDOS (e.g. Figure 5.3(f)) and a comparison to Figure 5.8(b) indicates that they are coupled to transverse acoustic modes, which is consistent with the investigation by Shintani and Tanaka<sup>213</sup> in revealing a universal link between boson peak and transverse phonons in glass.

In the context of thermal properties, we believe these quasi-localized modes scatter heat-carrying acoustic modes by reducing their lifetime (peak broadening in Figure 5.8) instead of reducing their speeds, leading to a small thermal diffusivity and lattice thermal conductivity.

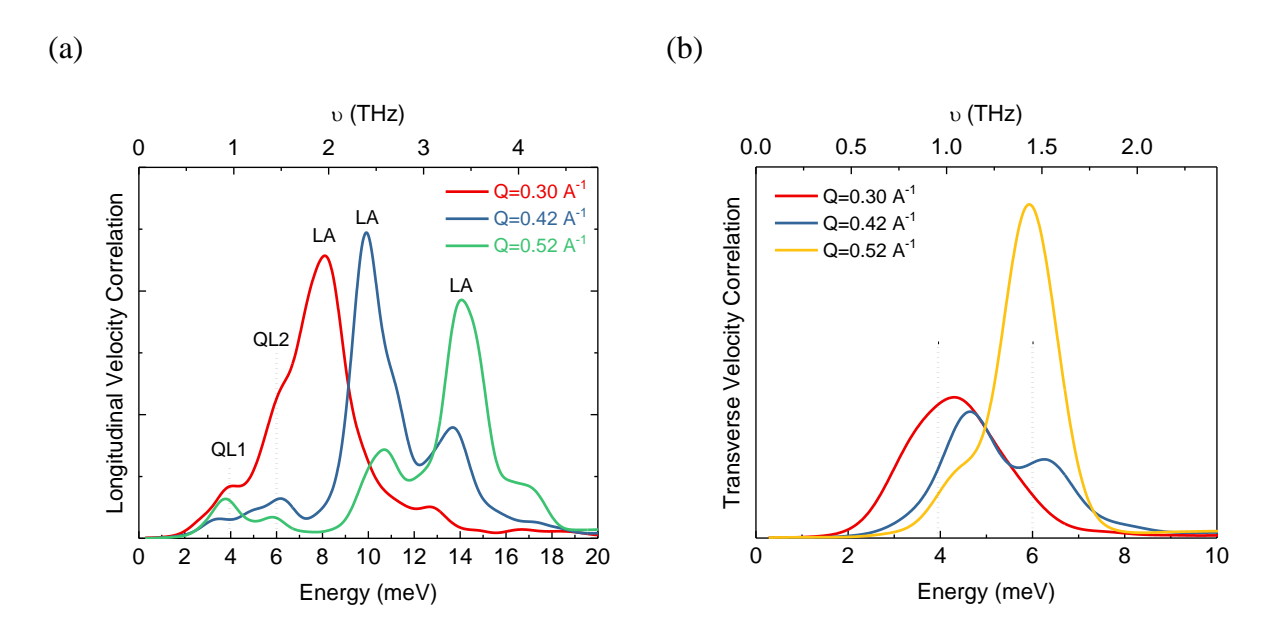


Figure 5.8: Longitudinal (a) and transverse (b) response of the coherent velocity correlation. Longitudinal acoustic (LA) and quasi-localized (QL) modes are marked in a. The dotted lines have the same energy between a and b.

If we compare Figure 5.55.5, Figure 5.7, and Figure 5.8, we can appreciate the advantage of employing a larger simulation cell, i.e. allowing smaller Q value to be accessed, where it becomes easier to identify the acoustic/sound modes. For example, the linear dispersion in Figure 5.7 could not to be observed in 1x1x1 cells.

## **5.4 Summary**

In this work we investigated the effect of simulation cell size and basis sets on the DFT-based molecular dynamics simulation results, using tetrahedrite Cu<sub>10</sub>Zn<sub>2</sub>Sb<sub>4</sub>S<sub>13</sub> thermoelectric as a model material. Three simulations, 1x1x1 cell with plane wave (PW) basis, 1x1x1 cell with

atomic orbital (AO) basis, and 2x2x2 cell with AO basis, were performed at 300 K. While variations can be observed for different cell sizes and basis sets, results of various structural and dynamic properties, such as lattice parameters, partial and total vibrational density of states, phonon dispersion, heat capacity, and EXAFS spectra are close to each other for three simulations. The larger 2x2x2 cell allows smaller Q to be accessed (closer to the hydrodynamic limit), where longitudinal and transverse sound/acoustic modes with linear dispersion can be identified. The bulk and shear modulus from extracted sound speeds agree with the experiment. In addition, two low-energy quasi-localized vibrational modes were detected. We believe that they scatter heat-carrying acoustic modes by reducing their lifetime instead of reducing their speeds, leading to a small thermal diffusivity and lattice thermal conductivity.

This work was published on Computational Materials Science 144 (2018): 315-321.

https://doi.org/10.1016/j.commatsci.2017.12.047

# CHAPTER 6: Structure and ionic conduction study on Li<sub>3</sub>PO<sub>4</sub> and LiPON with density functional tight binding (DFTB) method

#### **6.1 Introduction**

Despite that no conclusive explanation has been made, N in the LiPON is commonly ascribed as the key to the high ionic conductivity and outstanding electrochemical stability. Researches have shown that the conductivity of LiPON films increased as the N content increased, from  $7 \times 10^{-8}$  S/cm without any N content to  $3.3 \times 10^{-6}$  S/cm with 6% of N content  $^{91, 140}$ . However, how the N atoms coordinated with P atoms remains uncertain  $^{214-217}$ . By analyzing N1s X-ray photoelectron spectroscopy (XPS) data on LiPON films, Bates et al. indicated that N bridged among P atoms with double (N<sub>d</sub>) or triple (N<sub>t</sub>) coordination, and these crosslinked structure might cause the increase in Li<sup>+</sup> mobility by providing interconnected pathways  $^{78, 140}$ . However, another argument was made by Wang et al. that most N would form PO<sub>3</sub>N with apical N (N<sub>a</sub>) and the rest would be N<sub>d</sub><sup>218</sup>. Recent computational study supported the argument that only N<sub>a</sub> and N<sub>d</sub> configurations existed, while the ratio between this two was dependent on the Li content, with optimal composition Li<sub>2.94</sub>PO<sub>3.50</sub>No<sub>.31</sub> in terms of ionic conductivity  $^{219-220}$ . Investigating the both structures of the precursor Li<sub>3</sub>PO<sub>4</sub> and LiPON is the key to improve the battery performance and help illuminating the direction of future battery design.

Density functional theory<sup>221</sup> (DFT) based molecular dynamics (MD) simulations are commonly used in accessing the structural, electronic and transport properties of materials. A lot of researches on LiPON electrolyte have been done by DFT to simulate the crystalline (c-) /amorphous (a-) structures<sup>219-220, 222</sup>, energy calculations<sup>223</sup> and the interfacial reaction between LiPON and electrodes<sup>224-225</sup>. To study the transport properties, such as diffusion and ionic conduction, a large cell and a longtime scale simulation (more samplings) are preferable to obtain

reliable results. Previous study in Chapter 5 also showed the advantages of having a larger simulation cell size. Although DFT is known as accurate, it is limited by system size and simulation time. Thus, a suitable method which can balance the accuracy and efficiency is necessary. For example, here we employ a self-charge consistent density functional tight-binding (SCC-DFTB)<sup>113</sup> approach to study the structural and transport properties of Li<sub>3</sub>PO<sub>4</sub> and LiPON.

#### **6.2 Computational details**

Details of DFTB theories and equations derivation can be found in the introduction chapter, as well as at various publications<sup>113, 117, 226</sup> and will not be included here. All SCC-DFTB simulations were carried out by DFTB+ code proposed by Aradi et al<sup>227</sup>. DFTB parameters for the Li-P-O-N chemical space were obtained using the recently developed TANGO (tight-binding approximation-enhanced global optimization)<sup>228</sup> method that allows fast and reliable parameterization by performing a small amount of DFT calculations.

#### 6.2.1 Generation of c-Li<sub>3</sub>PO<sub>4</sub> and c-Li<sub>P</sub>ON models

Here we used γ-Li<sub>3</sub>PO<sub>4</sub> containing 128 atoms as initial c-Li<sub>3</sub>PO<sub>4</sub> structure. To build a c-Li<sub>2</sub>PO<sub>N</sub> cell, we replaced two O atoms by N atoms and removed two Li and two O atoms to balance the charge, so that the stoichiometry would be Li<sub>2.875</sub>PO<sub>3.75</sub>N<sub>0.125</sub>. Constant number of particles, pressure and temperature (NPT) ensemble was adopted to these two initial cells at 300, 800, 1000, 1400 and 1500 K for 20 ps. Constant number, volume, and temperature (NVT) ensemble was implemented at 1400 K and 1500 K for 400 ps.

## 6.2.2 Generation of a-Li<sub>3</sub>PO<sub>4</sub> and a-Li<sub>P</sub>ON models

In order to obtain amorphous phases, we performed a heat-and-quench method as shown in Figure 6.1. Initial structure guess was built by inserting 96 and 92 atoms in a cubic box by random packing, with stoichiometry Li<sub>3</sub>PO<sub>4</sub> and Li<sub>2.83</sub>PO<sub>3.67</sub>N<sub>0.17</sub>, respectively, and ~40% density

of the experimental reference for c-LiPON<sup>79</sup>, using the software Aten<sup>229</sup>. Then we annealed the cell at 1000 K for Li<sub>3</sub>PO<sub>4</sub> and 1400 K for LiPON, and quenched the structures at 300 K for equilibration, to obtain the amorphous phases. All the heating and cooling steps were allow to equilibrate for 20 ps. NVT simulations were applied to a-Li<sub>3</sub>PO<sub>4</sub> and a-LiPON afterward for at least 200 ps, followed by equilibrated NPT at the certain temperature. Berendsen thermostat was used for NPT runs and Nose-Hoover thermostat was employed for NVT simulations. Time step was chosen to be 1 fs for both NPT and NVT ensembles.

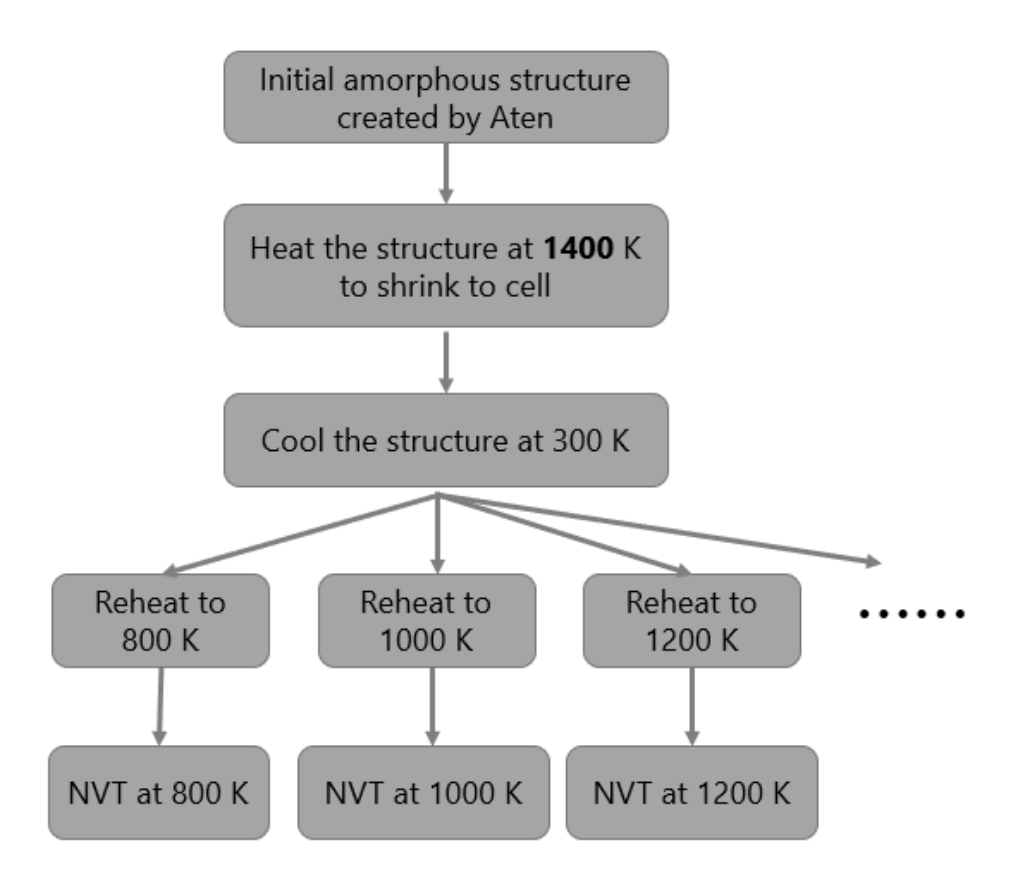


Figure 6.1: Flowchart of generation of amorphous a-Li<sub>3</sub>PO<sub>4</sub> and a-Li<sub>P</sub>O<sub>N</sub>.

#### 6.3 Results and discussion

## **6.3.1** Lattice parameters

Table 6.1: Calculated lattice parameters (a, b, c) of c-Li<sub>3</sub>PO<sub>4</sub> and c-LiPON at 300 K comparing to experiments.

	a(Å)	b(Å)	c(Å)
c-Li <sub>3</sub> PO <sub>4</sub> (exp) <sup>79</sup>	10.4612	6.1113	4.9208
c-Li <sub>3</sub> PO <sub>4</sub> (cal)	10.3267	6.0247	4.8499
Error (%)	-1.29	-1.14	-1.44
c-LiPON (exp) <sup>79</sup>	10.4690	6.1153	4.9195
c-LiPON (cal)	10.3487	6.0376	4.8602
Error (%)	-1.15	-1.27	-1.21

We examined the lattice parameters obtained from NPT simulations at 300 K for c-Li<sub>3</sub>PO<sub>4</sub> and c-LiPON to validate our computational results (shown in Table 6.1). Overall speaking the lattice parameters are in good agreement to experiments with about 1.1-1.5% underestimation. Volumes are also calculated for all four structures at different temperatures. Since we had different cell sizes for crystalline and amorphous phases, for the sake of easy comparison, total volumes were normalized by dividing by 16 for crystalline phases and by 12 for amorphous phases. Linear relationship can be observed for crystalline phase, while the amorphous phase had general increasing trend upon heating but kinks can be identified, e.g., amorphous Li<sub>3</sub>PO<sub>4</sub> at 800 K. Given that there were less atoms in amorphous LiPON cell than amorphous Li<sub>3</sub>PO<sub>4</sub>, the former had smaller volume than the other.

## **6.3.2** Exploration of LiPON structure

As mentioned above, there is a controversy occurred in the field that whether the  $N_t$  exist in LiPON. Spectroscopic works showed the evident that bridging N were presented in LiPON but it was difficult to distinguish whether they are  $N_d$  or  $N_t$ , or both. Here this computational work

enabled us to get atomic insight of LiPON structure. Figure 6.2 showed an example of a-LiPON structure after NVT run at 1200 K, with  $N_a$  and  $N_d$  bonding environment highlighted. At all other temperatures we simulated,  $N_a$  and  $N_d$  coexisted in a-LiPON structure, and no  $N_t$  was observed. It's worth noting that, for c-LiPON, two  $N_d$  existed at 1500 K and two  $N_a$  at 1400 K, which means the generation of  $N_d$  need relatively large external energy.

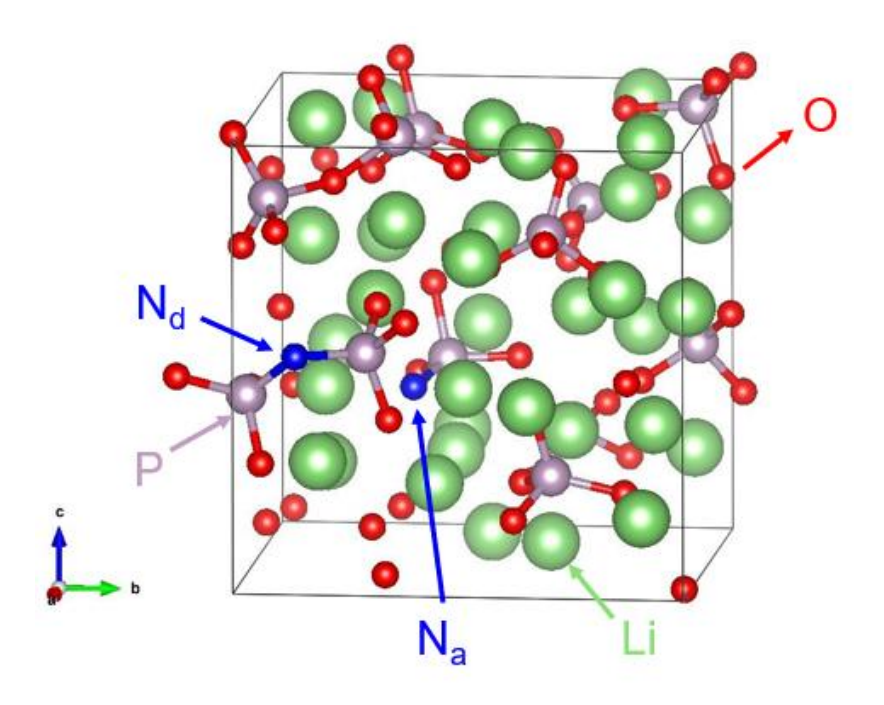


Figure 6.2: Schematic of a-LiPON structure at 1200 K from NVT run.

To understand the role of N in a-LiPON structure, we also examined the bond distance (BD) and bond order (BO) of P-N and P-O. Several representative snapshots of trajectory from 1400 K NVT simulation of a-LiPON had been investigated. The Density Derived Electrostatic and Chemical (DDEC) scheme<sup>151</sup> calculation was applied here to calculate the BO of P-N and P-O. In Figure 6.3 we plotted BO as a function of BD of these pairs. BO of P-N<sub>a</sub> were larger than P-N<sub>d</sub> and P-O when the BD were the same, meaning that P-N<sub>a</sub> bonds were stronger than other two pairs. The longest BD of P-N<sub>a</sub> was 1.91 Å with BO = 1.09, while the shortest BD of this pair was 1.43

Å with BO = 2.17, which indicated that P-N<sub>a</sub> pair is dynamically changing between single bond and double bond. Same scenario can be observed for P-N<sub>d</sub> pair and P-O pair, but it is notable that the BD of P-N<sub>d</sub> can vary from 2.15 Å (BO = 0.53) to 1.46 Å (BO = 1.76). When N<sub>d</sub> was close to one P with BO close to 2, it was far from the P on the other side with BO close 1, indicating that two PO<sub>3</sub> radicals were linked by N<sub>d</sub> in the form of P=N<sub>d</sub>-P, which was consistent with the hypothesis previously proposed by Wang et al<sup>79</sup>, although they claimed that only a small concentration of this kind of units would contain in LiPON. This argument could be settled by increasing the population of N in future works.

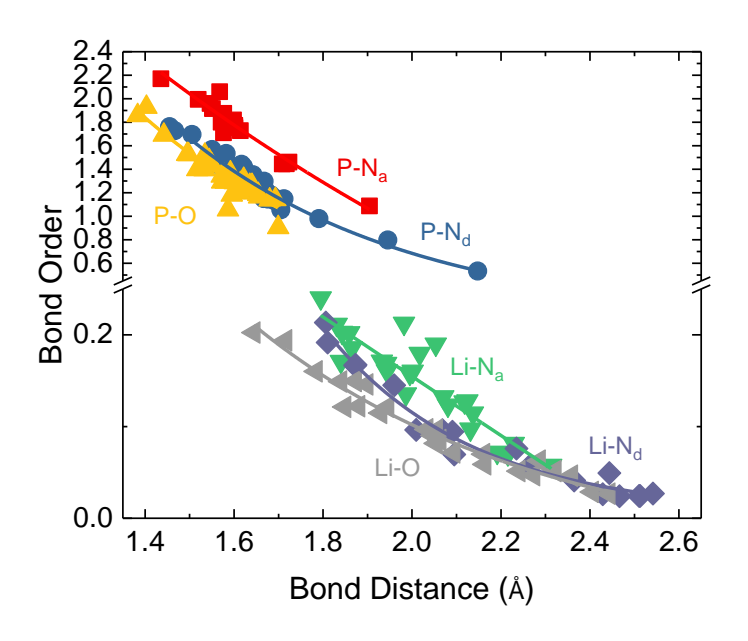


Figure 6.3: Bond order as a function of bond distance of P-N, P-O and Li-X pairs.

Similar analysis had been done for Li-X ( $X=N_a$ ,  $N_d$  and O) pairs and was shown in Figure 6.3. Although Li atoms were likely to form weak ionic bond to other elements, here BO of Li- $N_a$  were generally stronger than Li-O and Li- $N_d$ , suggesting that Li were less mobile when bonded to  $N_a$ . In addition, we investigated the local environment of Li atoms in a-LiPON with the help of

electron localization function  $^{230}$  (ELF) calculation. ELF maps of Li-X units with same BD of 2.12 Å were displayed in Figure 6.4 for comparison. Mushroom shapes electron sharing between Li-X were clear indicator of the existence of lone pair, while the electron shape was smaller and more localized in Li-O than Li-N<sub>a</sub> and Li-N<sub>d</sub>. Less electron sharing of P-O than P-N<sub>a</sub> and P-N<sub>d</sub> can also be observed here. To further investigate the Li-X interactions, we selected 2000 snapshots from 200 ps trajectory at 1400 K and calculated the Li coordination environment around these X atoms within cutoff distance of 2.3 Å, which was plotted in Figure 6.5. In the case of N<sub>a</sub>, more than half of the data located with 3 Li coordination, while 32.55% with 4 Li coordination and 10.20% with two Li around. In contrast, the Li coordination around N<sub>d</sub> and O were more distributed, indicating that Li atoms were more mobile when bonded to N<sub>d</sub> and O.

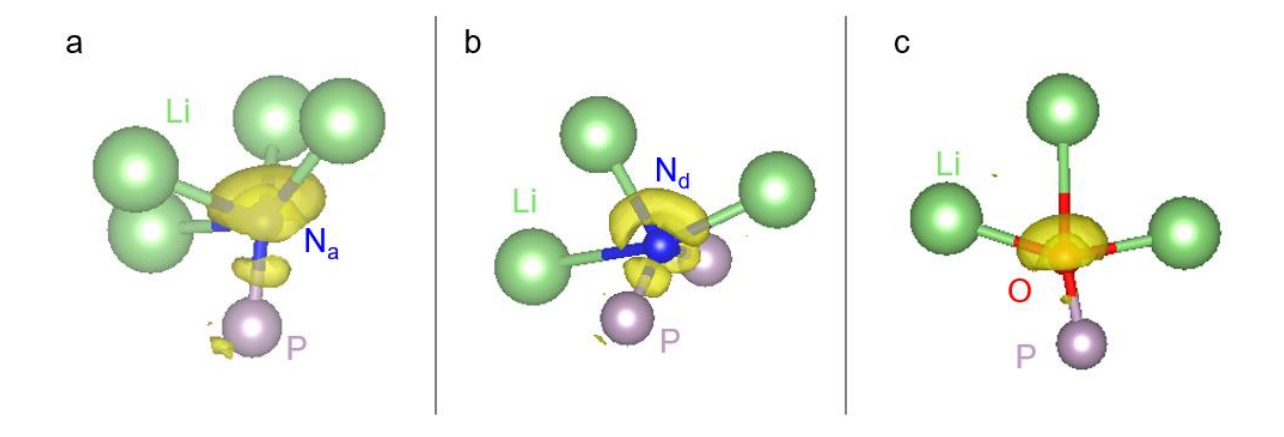


Figure 6.4: ELF maps of (a) Li-N<sub>a</sub>, (b) Li-N<sub>d</sub> and (c) Li-O units (isosurface level of 0.82).

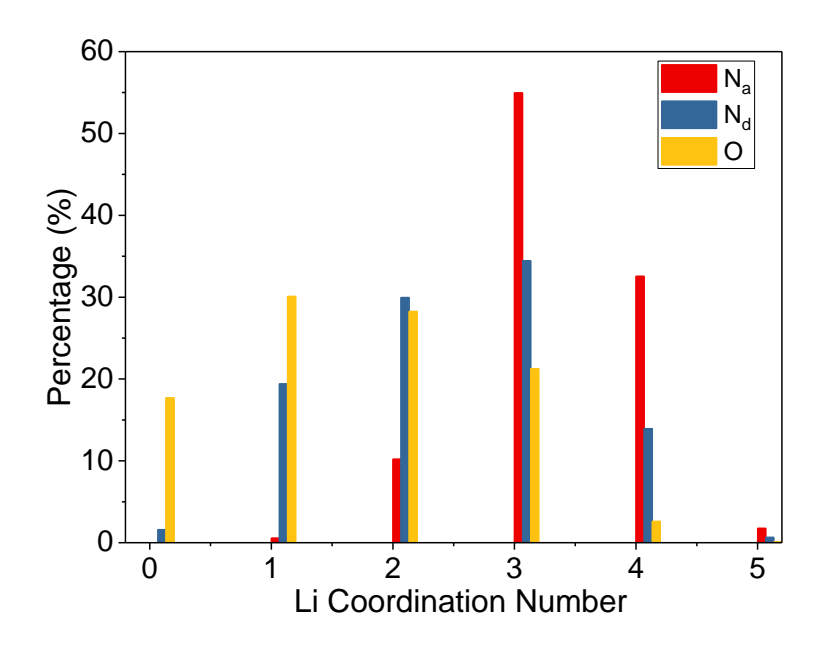


Figure 6.5: Statistical results of Li coordination number around Na, Nd and O.

# 6.3.3 Self-diffusivity of different atomic groups

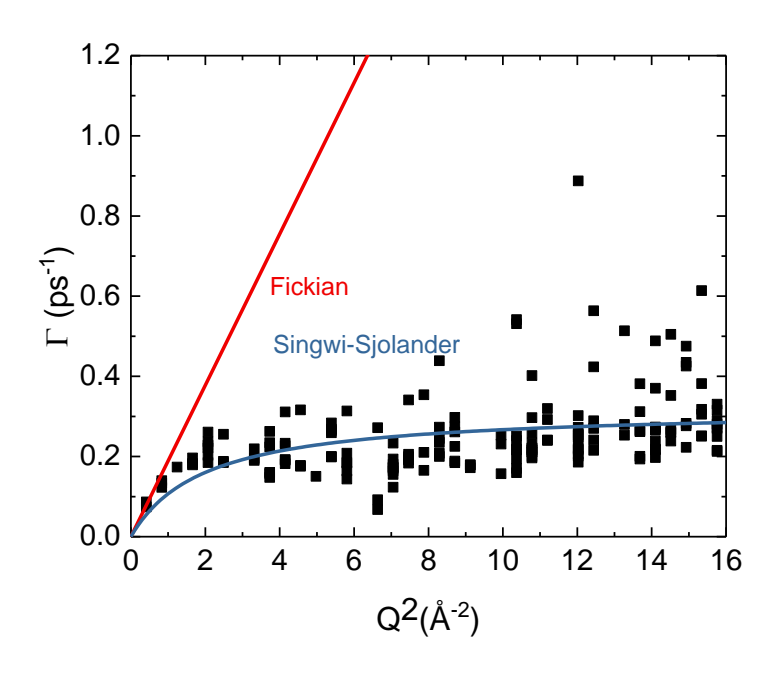


Figure 6.6: An example of  $\Gamma$  as a function of  $Q^2$  in Li diffusing at 1200 K for a-LiPON.

Determination of Li self-diffusivity is critical for understanding mechanism of the ionic

transport in Li-ion batteries<sup>231-233</sup>. Here we investigated the self-diffusivity of different atomic group by the incoherent density correlation I(Q,t), as discussed in Section 3.3.2. We implemented this same method to all the atomic groups in Li<sub>3</sub>PO<sub>4</sub> and LiPON to examine the self-diffusivity and the diffusion mechanism.

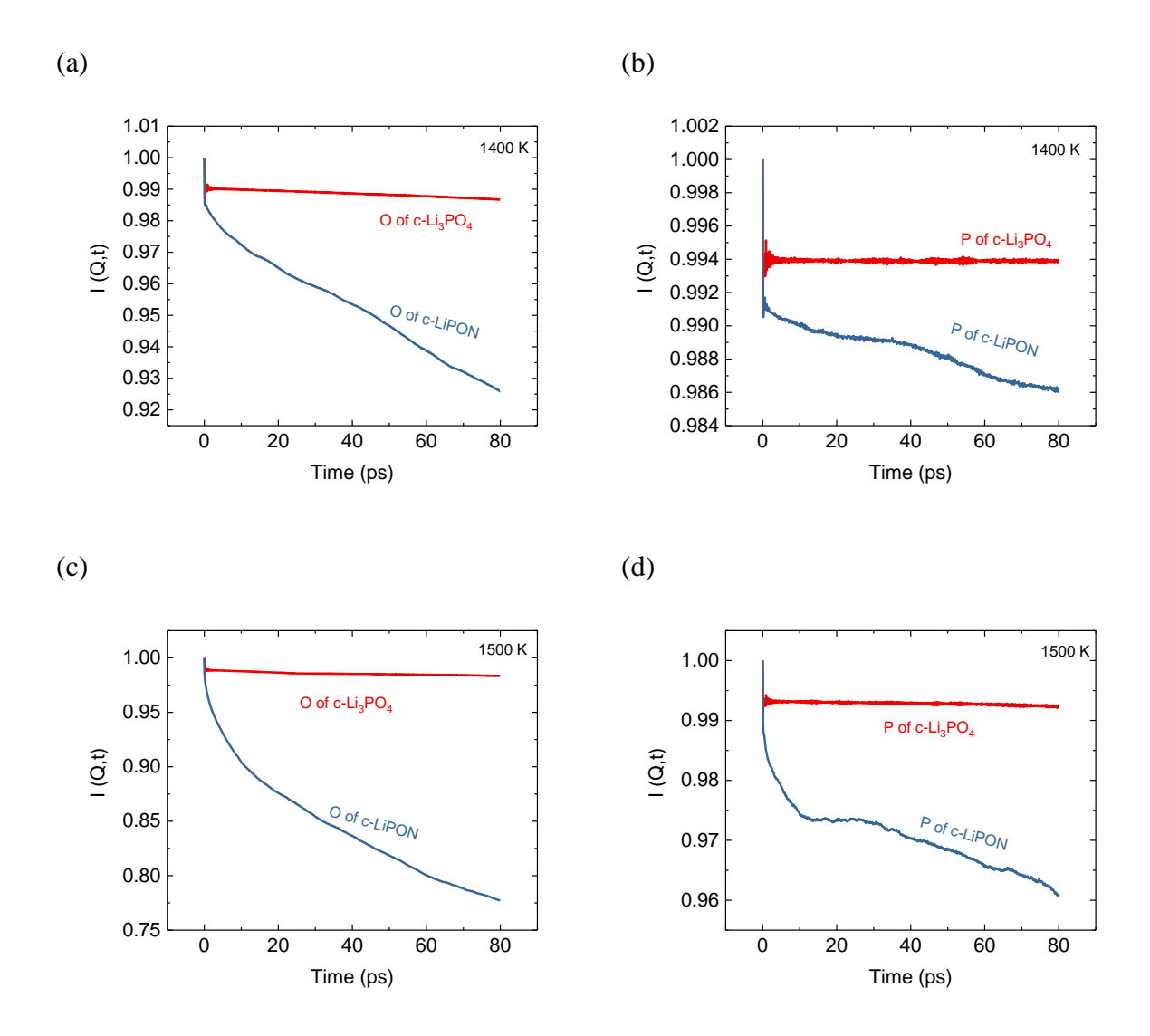


Figure 6.7: I(Q, t) of P and O for c-Li<sub>3</sub>PO<sub>4</sub> and c-LiPON at 1400 K and 1500 K.

Figure 6.6 is an example of  $\Gamma$  as a function of  $Q^2$ . Both Fickian model and SS model will be applied to extract the diffusivity D, residence time  $\tau$  and mean square jump distance  $\langle r^2 \rangle$ . The dynamics of atomic species P, O and N will be investigated first. A rapid decrease following by a

stable non-zero plateau indicated the vibration motion instead of diffusing. The I(Q,t) of P and O with smallest Q value in c-Li<sub>3</sub>PO<sub>4</sub> and c-Li<sub>PON</sub> showed typical examples of vibrating and diffusing types, where we noticed that P and O were diffusing in the c-Li<sub>PON</sub> structure but remained vibrating in c-Li<sub>3</sub>PO<sub>4</sub>, as shown in Figure 6.7. This implied that the addition of N atoms in c-Li<sub>PON</sub> helped the diffusion of P and O in the crystalline phase. The I(Q,t) of N in c-Li<sub>PON</sub> was not included here but it showed typical diffusion mode as well.

Self-diffusivity of P, O and N were shown in Figure 6.8. Activation energy ( $E_a$ ) was obtained by fitting the data to the Arrhenius law. Although the self-diffusivity of P, O and N can be calculated, the actual motion of these atoms could be correlated movement of a whole molecule (e.g.  $PO_4$ ), instead of individual jump. In c-LiPON, although P and N were diffusing according to their I(Q, t), their self-diffusivities were too low to get trustable estimation, and thus not included in the figure. It was notable that P and O were less mobile with higher activation energy in a-LiPON than in a-Li<sub>3</sub>PO<sub>4</sub>, especially P, which can be ascribed to the existence of  $N_d$  that bridged two P atoms together. The strong connection between  $N_d$  and P due to their covalent bond, and thus a possible increase of network-strain energy<sup>234</sup>, remarkably reduced the mobility of P, as well as the O, which was bonded to P. In addition, in a-LiPON, P stopped diffusing below 1200 K, O and N stopped diffusing below 1000 K, suggesting the advantage of a-LiPON being a single ion (Li-only) conductor at low temperatures.

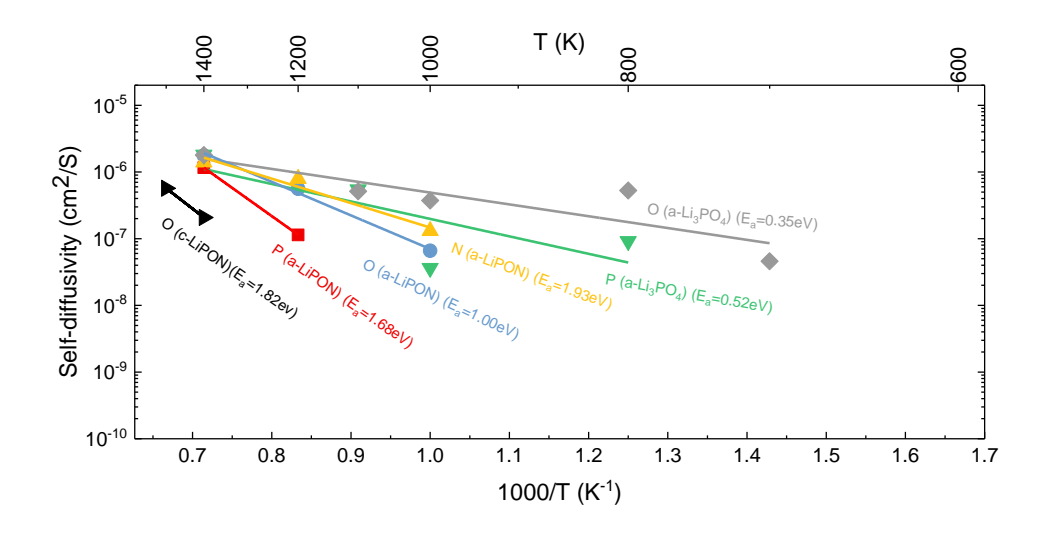


Figure 6.8: Self-diffusivity of P/O/N atomic groups from Li<sub>3</sub>PO<sub>4</sub> and LiPON as a function of temperature.

Li self-diffusivity from different structures had been summarized in Figure 6.9, together with computational results from other work and experimental values. Our calculated Li self-diffusivity of a-Li<sub>3</sub>PO<sub>4</sub> was in good agreement with Kuwata's experimental data measured by secondary ion mass spectroscopy<sup>235</sup>, with similar E<sub>a</sub> of 0.52 eV vs. 0.57 eV. Li self-diffusivity of a-Li<sub>3</sub>PO<sub>4</sub> obtained from Li et al. using neutral network (NN) potentials<sup>236</sup> was roughly one order of magnitude lower while the E<sub>a</sub> of 0.55 eV was close to ours. We also performed a DFT calculation using same a-LoPON structure at 1400 K employing *Vienna Ab initio Simulation Package* (*VASP*)<sup>193-196</sup> code for validation. DFT result showed slightly higher Li self-diffusivity (1.24 x 10<sup>-4</sup> cm<sup>2</sup>/s) than DFTB result (5.59 x 10<sup>-5</sup> cm<sup>2</sup>/s) at 1400 K. In addition, a-LiPON was observed to have slightly lower Li self-diffusivity than a-Li<sub>3</sub>PO<sub>4</sub>. This is consistent with what we stated above, that the existence of N<sub>a</sub> in a-LiPON suppressed the Li diffusion due to stronger Li-N<sub>a</sub> bonds. c-LiPON had almost one order of magnitude higher Li self-diffusivity than c-Li<sub>3</sub>PO<sub>4</sub> (4.05 x 10<sup>-6</sup> cm<sup>2</sup>/s vs. 6.24 x 10<sup>-7</sup> cm<sup>2</sup>/s at 1400 K), while both had large E<sub>a</sub> (~2.70 eV). We also tried to extract Li diffusivity of crystalline phases below 1400 K and it turned out that Li barely moved.

The residence time and jump length of Li diffusion obtained from SS model fits were shown in Figure 6.10. Rapid increase of residence time can be observed for all structures and activation energy can be obtained by an Arrhenius fit. Activation energies extracted from residence time were comparable to the ones obtained from Li self-diffusivity. The jump lengths generally decreased with increasing temperature, except the outlier for c-LiPON at 1500 K.

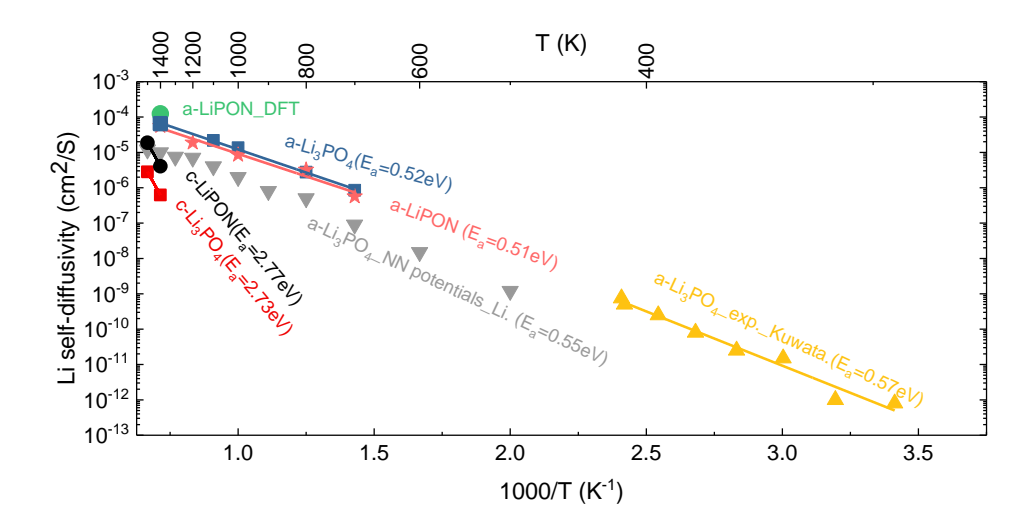


Figure 6.9: Li self-diffusivity of various structures as a function of temperature comparing to experimental results.

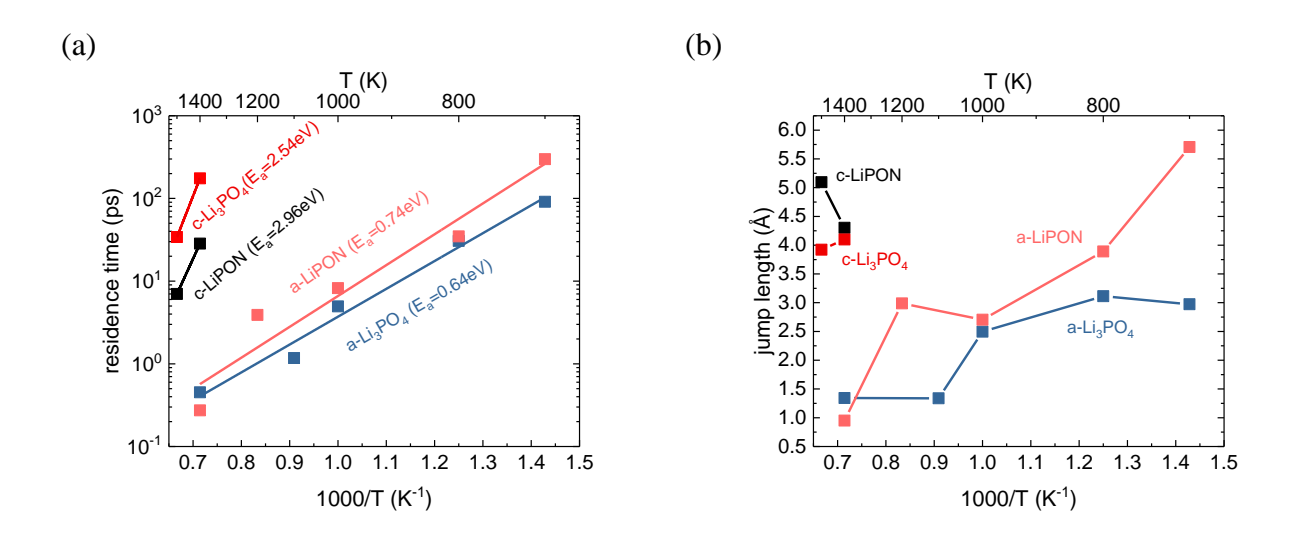


Figure 6.10: Residence time (a) and jump length (b) of Li diffusion.

## 6.3.4 Ionic conductivity

Ionic conductivity is known to be one of the most important properties for solid-state electrolyte materials. Here we extracted the ionic conductivity of Li<sub>3</sub>PO<sub>4</sub> and LiPON by coherent charge current density correlation function<sup>237-238</sup>, which includes the longitudinal and transverse components. The longitudinal component can be expressed as:

$$C^{L,c}(Q,t) = \frac{e^2}{Vk_BT} \frac{1}{Q^2} \langle (Q \cdot J(Q,0))(Q \cdot J(-Q,t)) \rangle, \tag{38}$$

while the transverse component as:

$$C^{T,c}(Q,t) = \frac{e^2}{Vk_BT} \frac{1}{Q^2} \langle (Q \times J(Q,0))(Q \times J(-Q,t)) \rangle, \tag{39}$$

where e is the electron charge, V the volume of the cell,  $k_B$  the Boltzmann constant, T the temperature. I(Q,t) is the collective charge current, which can be written as:

$$J(Q,t) = \sum_{n=1}^{N} q_n v_n e^{-iQ \cdot r_n(t)},$$
(40)

where  $q_n$  and  $v_n$  is the charge and velocity of nth atom, respectively. The Fourier Transform (FT) then applied to the longitudinal and transverse component as:

$$S^{L,T}(Q,\omega) = \int_0^\infty C^{L,T}(Q,t)e^{i\omega t}dt,\tag{41}$$

where  $\omega$  is the frequency. The ionic conductivity  $\sigma$  is extracted from the FT of transverse component as:

$$\sigma = \lim_{\omega \to 0} S^T(Q, \omega). \tag{42}$$

Figure 6.11 reveals an example of the transverse component of coherent charge current density correlation function (a)  $C^{T,c}(Q,t)$  and the corresponding FT form (b)  $S^T(Q,\omega)$  with three smallest Q values for a-LiPON at 1400 K. Unlike  $S^L(Q,\omega)$ , which shows as a peak with zero intercept at zero frequency,  $S^T(Q,\omega)$  has a non-zero intercept, meaning the ionic conductor

behavior of a-LiPON. In the real case, we cannot access the zero frequency due to the limited cell size by applying Equation (42). Thus, we averaged the six outputs of smallest Q value from the smallest  $\omega$  as the ionic conductivity.

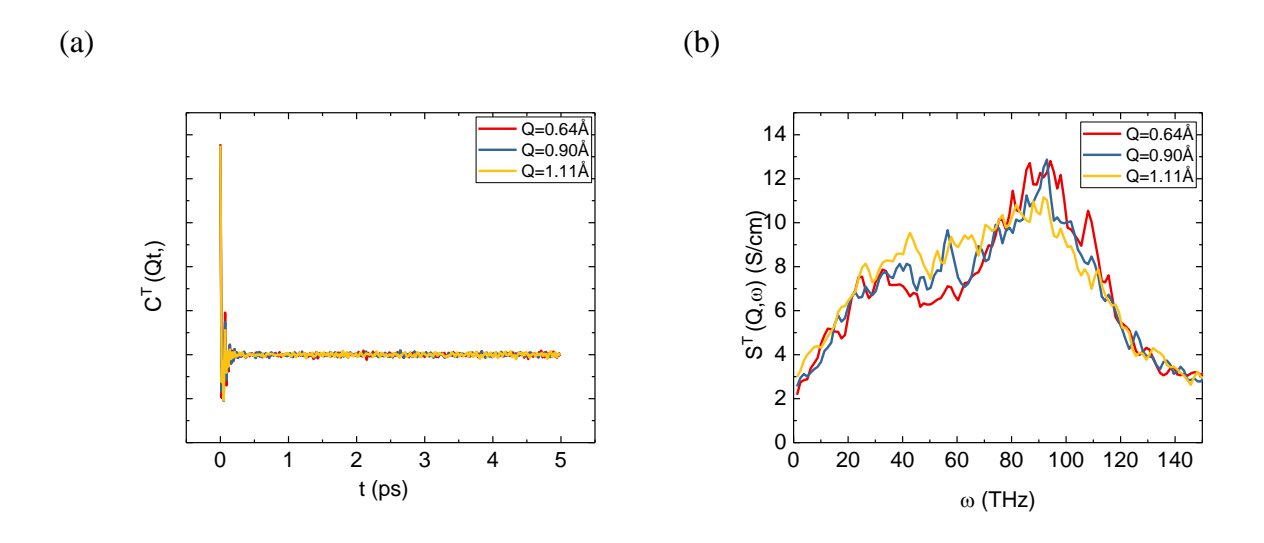


Figure 6.11: (a) Time and (b) frequency domain for the transverse component of coherent charge current density function for three smallest Q at 1400 K for a-LiPON.

Simulated results were summarized in Figure 6.12, including several experimental data for comparison. The ionic conductivity of a-Li<sub>3</sub>PO<sub>4</sub> was comparable to the experimental results from Kuwata et al<sup>235</sup> and Yu et al<sup>91</sup>, except that the E<sub>a</sub> of 0.27 eV was slightly lower. Dyre et al.<sup>239</sup> proposed a shoving model for 'flowing solids' to explain the temperature dependence of activation energy, stating that the activation energy increased as temperature decreased, which might be accommodated in this case and need further demonstration. Although Yu's experimental data showed that a-Li<sub>2</sub>PO<sub>N</sub> had one order magnitude higher ionic conductivity than a-Li<sub>3</sub>PO<sub>4</sub> at lower temperature range, at higher temperatures (700 K to 1400 K), ionic conductivity of a-Li<sub>2</sub>PO<sub>N</sub> and a-Li<sub>3</sub>PO<sub>4</sub> were close according to our DFTB calculation results. This can be ascribed to the highly disorder of both structures, or the lack of charge carriers (Li<sup>+</sup>), since a-Li<sub>2</sub>PO<sub>N</sub> had lower Li

concentration than a-Li<sub>3</sub>PO<sub>4</sub>. The excess Li concentration was proven to be effective by previous measurements and reached a maximum conductivity at 2.94 Li:P ratio<sup>91, 140, 217, 220, 240</sup>. Ionic conductivity of a-LiPON at 1400 K from DFT and DFTB showed good consistency, further validating the reliability of our DFTB calculation. Experimental data from a similar composition Li<sub>2.88</sub>PO<sub>3.73</sub>N<sub>0.14</sub> conducted by Wang et al.<sup>79</sup> were plotted here for comparison. c-LiPON revealed higher ionic conductivity and higher activation energy than c-Li<sub>3</sub>PO<sub>4</sub>, which was consistent with previous discussion in Figure 6.7, that only Li was diffusing in c-Li<sub>3</sub>PO<sub>4</sub> while all atomic groups were mobile in c-LiPON.

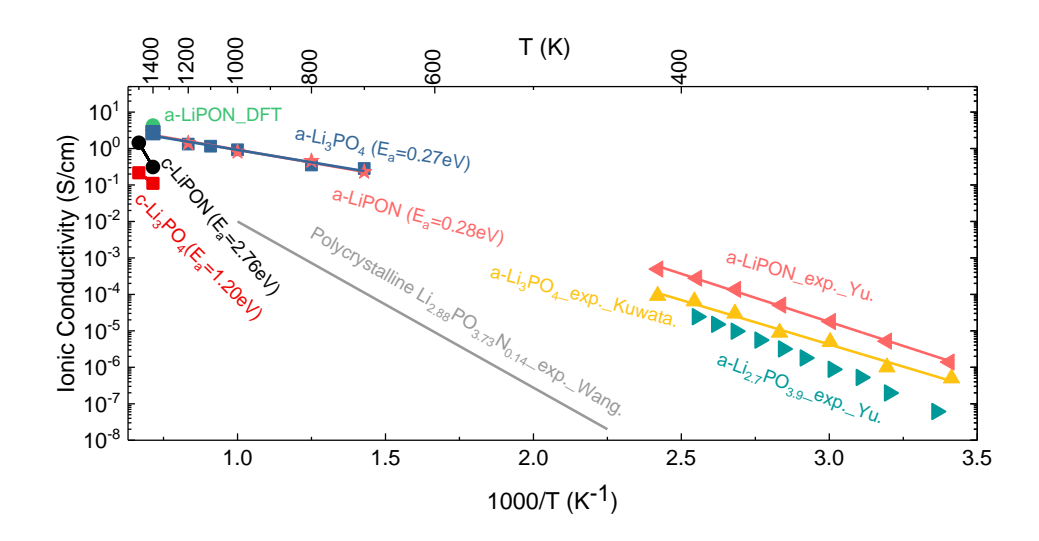


Figure 6.12: Calculated ionic conductivity of various structures as a function of temperature comparing to experimental data.

# **6.4 Summary**

DFTB is proven to be a powerful tool to deal with large-scale MD simulation. In this work we firstly applied DFTB with new parameters for Li-P-O-N interactions to generate crystalline and amorphous LiPON structure and investigate the structural and dynamical properties of Li<sub>3</sub>PO<sub>4</sub> and LiPON. Both N<sub>a</sub> and N<sub>d</sub> can be observed in a-LiPON, but only in c-LiPON at higher

temperature, whereas no evidence of  $N_t$  existed. The bond order calculation indicated that  $N_d$  incorporated with P in the form of P=N<sub>d</sub>-P, and Li interacted with  $N_a$  more strongly than O or  $N_d$ . In addition, self-diffusivity and ionic conductivity calculated by DFTB had been investigated here. The addition of N atoms increased the mobility of P and O in crystalline phase. Li self-diffusivity of a-Li<sub>3</sub>PO<sub>4</sub> was in good agreement with experimental data, but less than one magnitude higher than results from other computational work. Jump length and residence time of Li diffusion from all four structures have been investigated. From our calculation, a-Li<sub>3</sub>PO<sub>4</sub> shared similar ionic conductivity with a-LiPON at the high temperature range, which is likely due to the highly disordered structures for both. Further works need to be accomplished to verify some hypothesis raised by this work such as adjusting the N doping population and Li concentration in LiPON. The capability of DFTB demonstrated in this work also enable the feasibility of more complicated computational works, e.g., LiPON/Li metal interface study.

# CHAPTER 7: Preliminary study on LiPON/Li interphase

#### 7.1 Introduction

The nobility of LiPON electrolyte comes from its electrochemical stability contacting with Li metal, however, the origin remains inconclusive. Schwobel et al.<sup>241</sup> proposed the reaction at LiPON/Li interface with decomposition of LiPON and formation of Li<sub>2</sub>O, Li<sub>3</sub>N and Li<sub>3</sub>P, by X-ray photoemission spectroscopy (XPS). Another research by Zhu et al.<sup>242</sup> indicated that the stability between electrolytes (LiPON and Li<sub>3</sub>PS<sub>4</sub>) and Li metal is due to the above side reaction products. DFTB is proven to be powerful dealing with larger unit cell, as well as modeling and predicting structural and dynamical properties of LiPON in the previous chapter. Here in this chapter we will present some preliminary study on LiPON/Li interphase using DFTB method, in order to monitor the reaction between LiPON/Li.

#### 7.2 Computational details

Amorphous LiPON with composition Li<sub>2.83</sub>PO<sub>3.67</sub>N<sub>0.17</sub> obtained from Chapter 6 is applied as the bulk LiPON phase. Surface energies  $\sigma$  of a, b and c direction of the a-LiPON with vacuum are calculated using the following equation by DFT:

$$\sigma = \frac{1}{2} \left( E_{surf} - N_{atoms} \times E_{bulk} \right), \tag{43}$$

where  $E_{surf}$  is the total energy of the simulation box with the surface,  $N_{atoms}$  the number of atoms and  $E_{bulk}$  the energy per atom of bulk structure. Surface energies  $\sigma$  of a, b and c direction are obtained as 39.41 eV, 49.49 eV and 22.52 eV, respectively, indicating that c direction has the lowest surface energy and thus be chosen as the contact surface with metallic Li. 3x3x8 metallic Li slab is selected contacting with the LiPON phase. In order to accommodate the lattice parameters of 10.47 Å (a and b direction) of metallic Li slab, a stretched 1x1x4 LiPON cell (10.47)

Å on a, b direction and keep c direction unstretched) with vacuum on c direction is equilibrated at 450 K for 20 ps using NVT ensemble. The initial simulation supercell is composed by the equilibrated LiPON cell and a 3x3x8 metallic Li (100) slab with 511 atoms in total, as shown in Figure 7.1. Metallic Li atoms are manually colored as dark green in order to distinguish against the Li atoms from LiPON, while color coding for other atoms are the same as Figure 6.1. 2 Å vacuum layer is added between LiPON and metallic Li on both sides. It is notable that a Li vacancy is created on purpose to mimic the realistic case. DFTB parameters for the Li-P-O-N chemical space were obtained using TANGO method. Then NVT ensemble is implemented to LiPON/Li supercell for 80 ps at 450 K to model the reaction and dynamics using cp2k<sup>243</sup>. Nose-Hoover thermostat is employed.

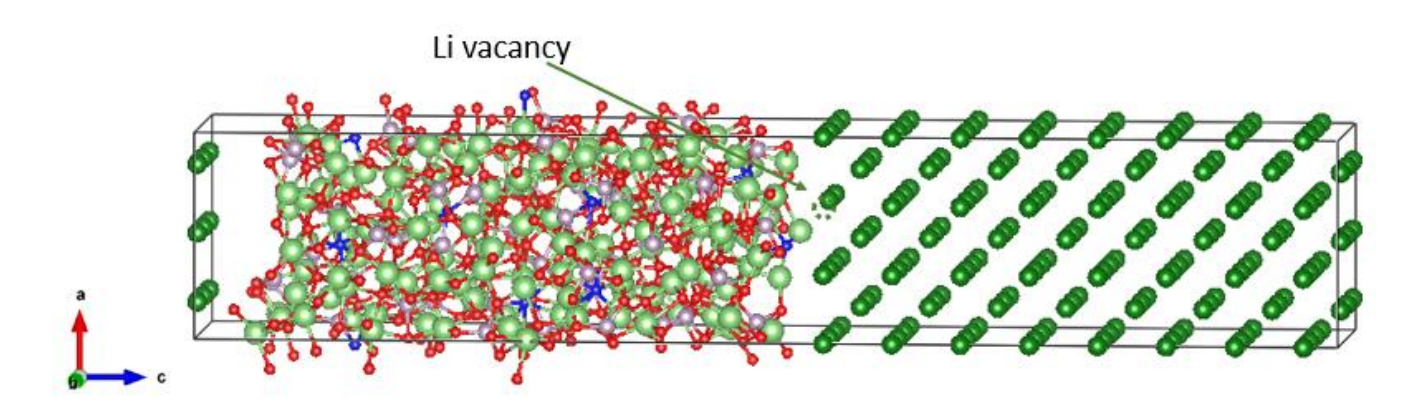


Figure 7.1: Initial supercell of LiPON/Li interface.

### 7.3 Results and discussion

## **7.3.1** Average structure

Average structure of the LiPON/Li supercell over 10 to 80 ps during the NVT run is shown in Figure 7.2 in order to evaluate the metallic Li layers. Additional simulation on metallic Li suggests that Li is bcc structure at 450 K under our computational setup. From Figure 7.2, it is

notable that 3 layers of disordered metallic Li exist due to the reaction with LiPON on both sides, while the middle layers are maintained as bcc structure.

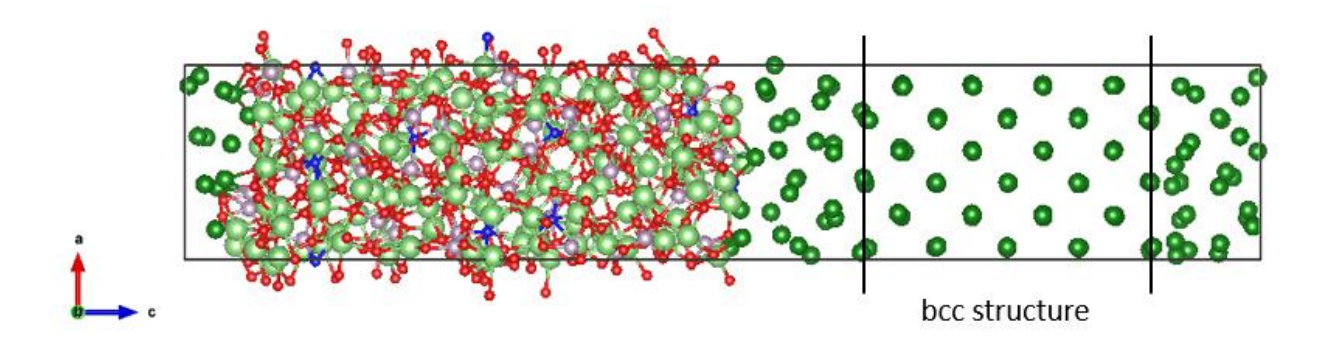


Figure 7.2: Average structure over 10 to 80 ps during the NVT run.

## 7.3.2 Reaction at the interface

Figure 7.3 depicts the MD simulation snapshots at 10 ps, 20 ps and 80 ps. No enormous change occurs during these periods, suggesting the reaction is accomplished with 10 ps, as well as the stability of the interface. It can be noted that the metallic Li atoms, which are close to interface, are attracted by the surface O atoms. No decomposition of LiPON, or formation of Li<sub>2</sub>O, Li<sub>3</sub>N and Li<sub>3</sub>P can be observed. In addition, no Li ions exchange between these two phases can be identified during our simulation time. Sicolo et al.<sup>224</sup> proposed that rupture of P-N and P-O bonds occurred when using the model of amorphous Li<sub>5</sub>P<sub>4</sub>O<sub>8</sub>N<sub>3</sub>/Li metal, while in our case we cannot observe the rupture.

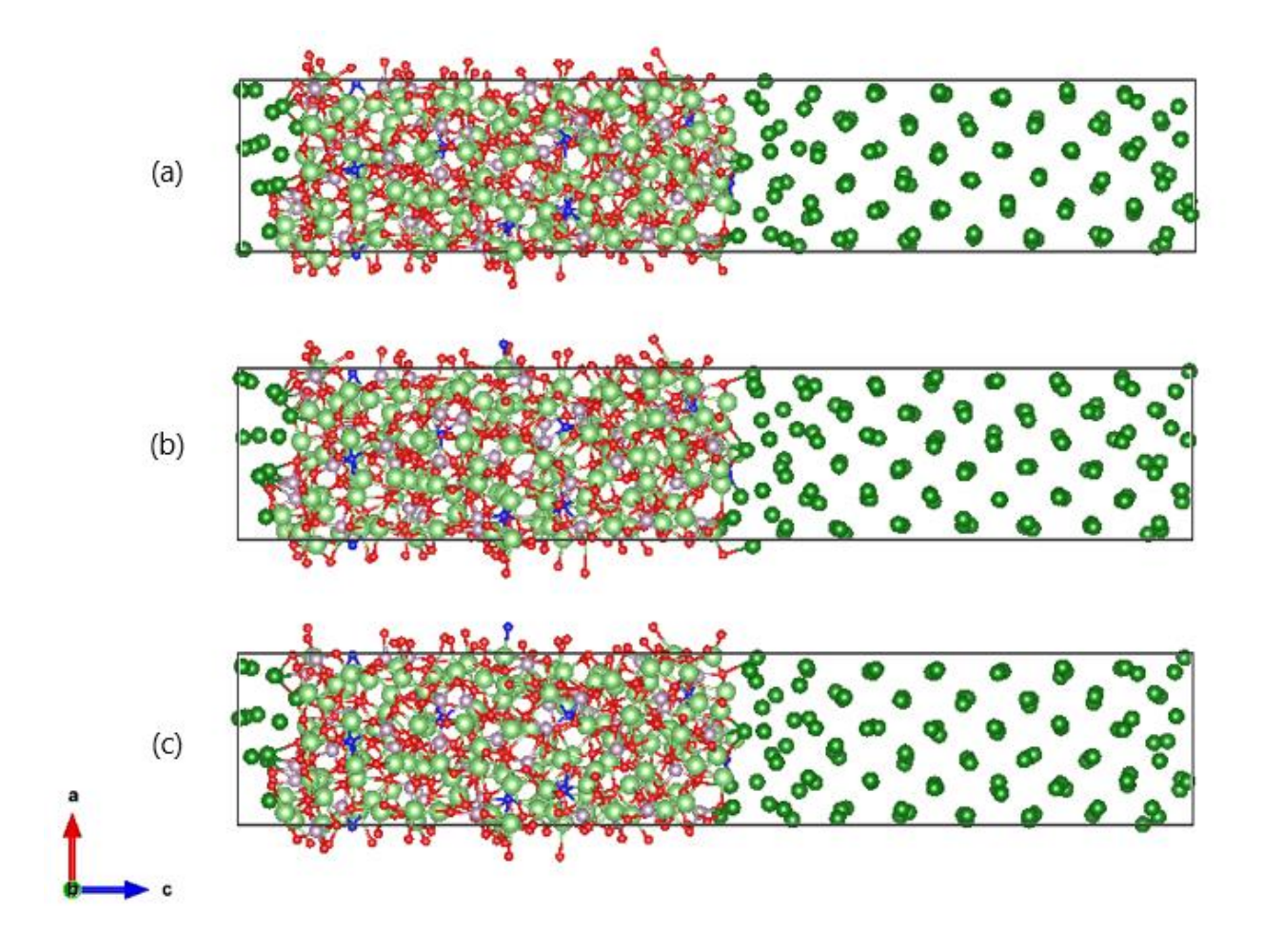


Figure 7.3: Snapshots of LiPON/Li interphase at (a) 10 ps, (b) 20 ps and (c) 80 ps.

# 7.3.3 Li charge distribution

In order to investigate the charge states of Li atoms in the model, we apply DDEC charge analysis <sup>151</sup> along the c axis, as shown in Figure 7.4. Since there is not much structural change during 10 to 80 ps from above, the snapshot structure at 20 ps is selected for the change analysis and the following DOS calculation. The charge of Li atoms shows around 0.8 in the LiPON bulk phase and 0 in the metallic layer, which is consistent with our previous observation that the middle of metallic Li maintains its origin. While at the interface from 29 Å to 35 Å, the interface effect on the Li charge distribution can be identified, where Li charge differ from -0.17 to 0.8, depending on the local environment and the distance from interface. At the interface region, the Li atoms

closer to interface show higher charges. The charge distribution suggests that interface effect is confined into a 6 Å region between two phases. P (~1.3), O (~ -0.9),  $N_a$  (~ -1.55) and  $N_d$  (~ -1.1) atoms do not show charge difference between the bulk and interface region.

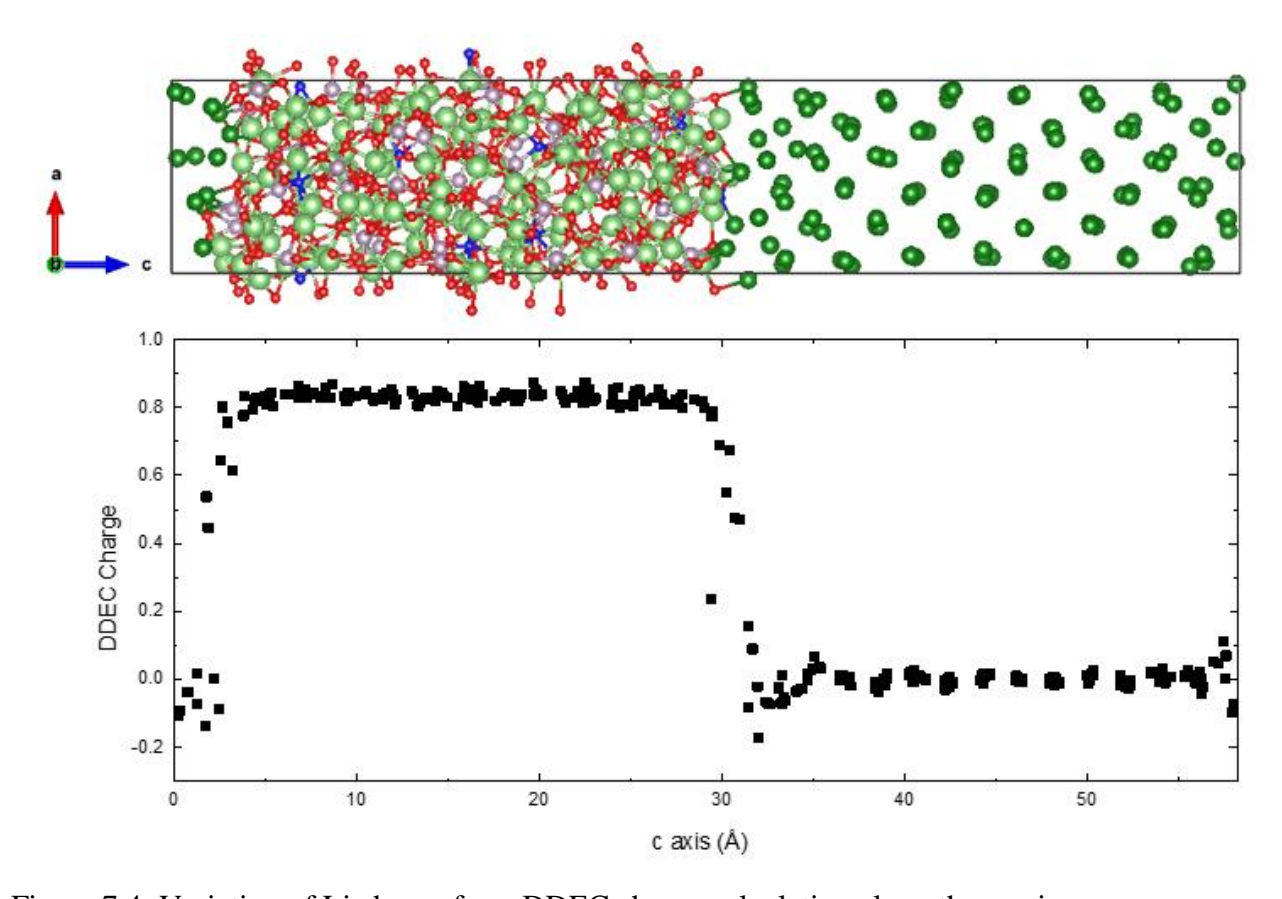


Figure 7.4: Variation of Li charge from DDEC charge calculation along the c axis.

## 7.3.4 Projected density of states

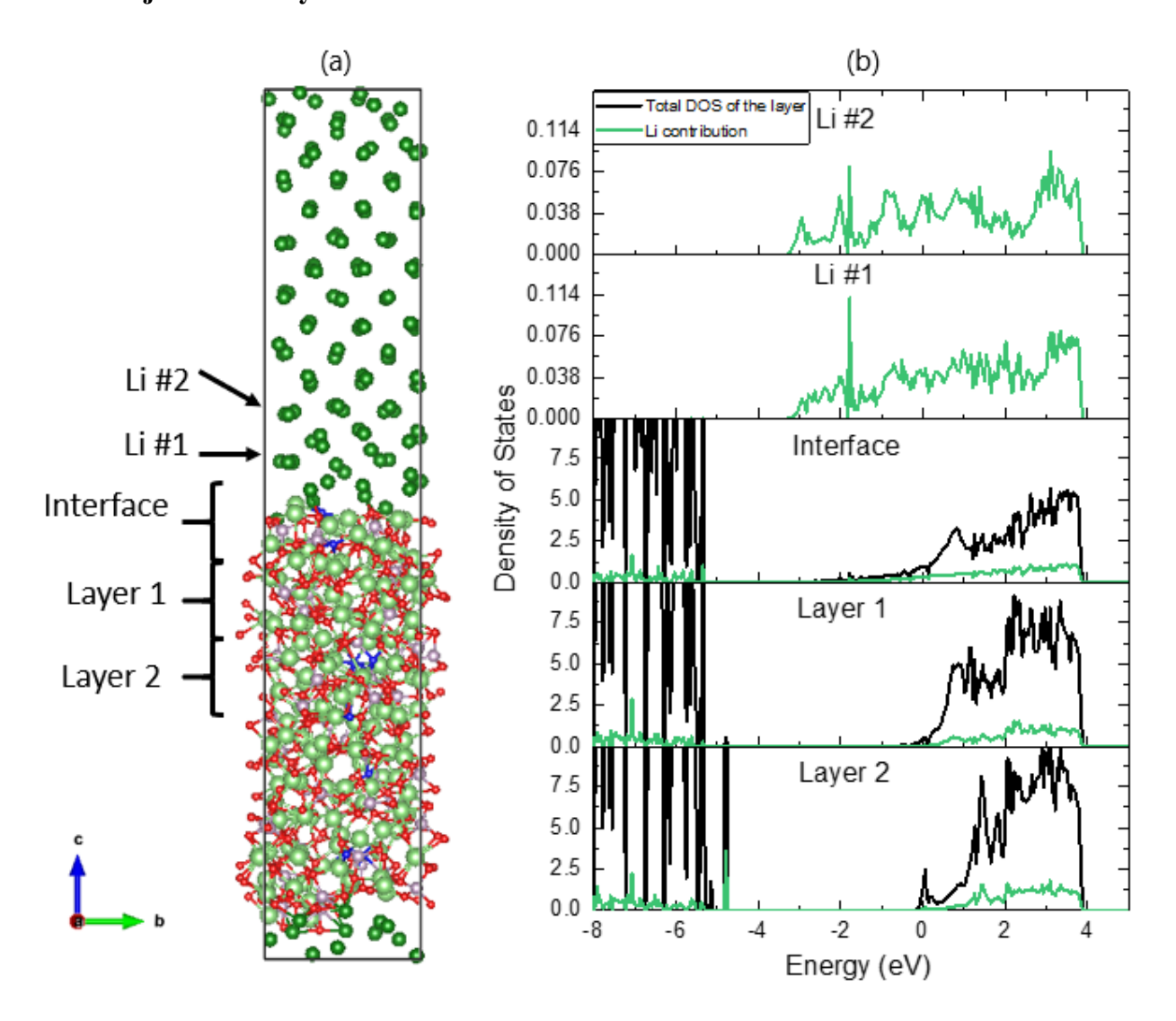


Figure 7.5: (a) A snapshot from MD at 20 ps with 3 selected layers (thickness of 6 Å) and two chosen Li atoms from metallic Li phase. (b) Projected density of states at selected layers and atoms. Fermi energy level is located at zero energy.

The density of states projected at different layers and selected Li atoms and atoms are shown in Figure 7.5(b) by DFT. Li #1 and Li #2 are two metallic Li atoms with different distances from interface. Interface layer is chosen based on the previous charge analysis with thickness of 6 Å, and layer 1 and layer 2 are two electrolyte layers with the same thickness, as shown in Figure

7.5(a). The Fermi level is located at zero energy. The metallic origin of Li #1 and Li #2 can be clearly identified regarding the states at Fermi energy level. It is notable that the projected DOS of interface also has states at the Fermi level, suggesting its metallic character. The metallic behavior of interface is likely due to the states induced by metallic Li. The electronic states at Fermi energy level reduce significantly beyond the interface in layer 1 and layer 2, however, small amounts of states can be recorded, which is likely due to the limitation of this method as we take the whole supercell as unit cell and thus a uniform Fermi energy is obtained for the whole cell.

### **CHAPTER 8 : Future work and conclusions**

### 8.1 Future work

### 8.1.1 Further investigation on thermoelectric material tetrahedrite

In this dissertation, we investigated thermoelectric material tetrahedrites on various aspects including their structures, low-temperature thermoelectric properties, origin of low lattice thermal conductivity and Cu movement in Cu-rich tetrahedrite. However, there are still a lot that remains unknown for the tetrahedrite family which require further investigation. For instance, there are various possible dopants for Cu and Sb sites that have not been explored for tetrahedrite. Moreover, the origin of metal to semiconductor (MST), accompanied with thermoelectric properties change, remains inconclusive. In addition, our study revealed the Cu movement in Cu-rich tetrahedrite, suggesting its potential as an ionic conductor, however, the optimized composition and temperature is not well-understood yet. These future investigations might improve the performance of tetrahedrite and provide insight of materials design.

## 8.1.2 Understanding the origin of LiPON/Li interphase

Although the previous chapter provides some insights on the reaction of LiPON/LI interphase, the origin of good electrochemical stability between the electrolyte-electrode remains unknown. Detailed analysis on the structural and dynamic properties on the interface, such as Li ion migration and charge transfer across the interface, can help us understand the interface better. In addition, optimization of N composition is critical to the performance of LiPON electrolyte. Experimental techniques such as surface morphology characterization, impedance spectroscopy are also helpful to extend our understandings and provide validation of our computational methods. Further study is needed on the reaction at the interface to provide research direction of improving battery applications.

## **8.1.3** Exploration in cathode materials

In addition to electrolyte materials we discussed above, the selection and regulation of cathode materials are critical to the performance of Li-ion battery, especially in the application of electrical vehicles (EV). The number of EV has continued to increase rapidly around the world, which is estimated to be more than 125 million by the year of 2030<sup>244</sup>. Figure 1.7 shows some of the promising candidates for cathode materials. Among them, LiFePO<sub>4</sub> (LFP), Li(Ni<sub>1-x-</sub> <sub>v</sub>Mn<sub>x</sub>Co<sub>v</sub>)O<sub>2</sub> (NMC), and Li(Ni<sub>1-x-v</sub>Co<sub>x</sub>Al<sub>v</sub>)O<sub>2</sub> (NCA) are demonstrated to be outstanding and currently in commercial use. LFP (~170 Ah kg<sup>-1</sup>, ~3.45 V vs. Li/Li<sup>+</sup>) has good electrochemical performance with low resistance, high current rating and long cycle life, while phosphate structure provides stability against overcharging and heat, leads to a wide operating temperature range between -30 °C to 60 °C<sup>245</sup>. NMC (150-180 Ah kg<sup>-1</sup> depending on composition) is another successful option due to its good performance by combing Ni and Mn, where Ni contributes to high specific energy and Mn offers the low internal resistance structure. Optimization of the percentages of Ni, Mn and Co are attracting a lot of interests. NCA (~200 Ah kg<sup>-1</sup>, ~3.8 V vs. Li/Li<sup>+</sup>) shares some similarities as NMC, but offers even higher specific energy, power densities and long life span<sup>245</sup>, however, safety concern exists. Improvement and regulation of current cathode materials, and exploration of new materials with advanced methods, are critical to further development of Li-ion batteries and EV industry.

### **8.2 Conclusions**

In this thesis, structure and properties of two energy materials: tetrahedrite Cu<sub>12</sub>S<sub>13</sub>Sb<sub>4</sub> and LiPON have been investigated by experimental and computational techniques, such as DFT and DFTB, together with MD simulations. These advanced modeling techniques and analysis methods employed in this thesis, are proven to be capable to explore the mechanism and predict materials

properties, which can be introduced to other material systems and provides insight on design of future energy materials.

Low-temperature properties of Cu<sub>12</sub>Sb<sub>4</sub>S<sub>13</sub> attract many research interests due to the abrupt change of structural, electrical and thermoelectric properties at a specific metal-semiconductor transition (MST) temperature at around 85 K. In order to investigate the structural properties of Cu<sub>12</sub>Sb<sub>4</sub>S<sub>13</sub>, we use DFT-based molecular dynamics simulation along with neutron diffraction measurement. Cu<sub>12</sub>Sb<sub>4</sub>S<sub>13</sub> maintains as cubic structure according to our computational and experimental results. However, negative thermal expansion below 50 K can be identified due to the interaction between Cu*12e* and coordinated Sb atom. Low energy phonon vibrational mode can be observed. Thermoelectric properties such as electrical resistivity, Seebeck coefficient and electronic thermal conductivity are also examined below and above MST temperature comparing to experimental data.

To understand the atomic dynamics of tetrahedrite, DFT-based first-principle molecular dynamics simulation is applied to investigate the Ni and Zn co-doped tetrahedrite Cu<sub>10.5</sub>NiZn<sub>0.5</sub>Sb<sub>4</sub>S<sub>13</sub>. The agreement between computed vibrational density of states and experimental inelastic neutron diffraction data at 300 K validate our simulation work. Anomalous phonon softening upon cooling can be explained by anharmonic rattling of Cu between two Sb atoms inside the Sb[CuS<sub>3</sub>]Cu atomic cage. The dynamic structure factors in the longitudinal and transverse direction obtained from coherent dynamics analysis suggest that the acoustic modes are confined in a small region of the scattering space, leading to the small thermal conductivity.

Cu-rich tetrahedrite with composition  $Cu_{14}Sb_4S_{13}$  is investigated in this thesis as well, focusing on the Cu transport properties. Structural instability can be speculated from the large fluctuation of lattice parameters during NPT run. Incoherent density correlation  $I_{inc,\alpha}(Q,t)$  at 700

K indicates that part of Cu atoms in the structure keep vibrating, while the others are diffusing between different Cu sites. Transport properties of mobile Cu, such as self-diffusivity, residence time and mean square jump length can be extracted by applying Fickian model and SS model fit. Additionally, to visualize the actual motions of Cu atoms, nuclear density map is employed, which allows us to identify the Cu diffusion pathways. Migration energy barriers  $E_m$  of different pathways can be estimated by "nudged elastic band" (NEB) calculation.  $E_m$  for 24g - 12d and 24g - 12e diffusion paths are 1.32 eV and 1.56 eV, respectively, suggesting that when Cu atom locates at 24g site, it is more energetic favorable to jump to a 12d site than to a 12e site.

Effect of simulation cell size and basis sets on the DFT-based molecular dynamics simulation is examined using tetrahedrite Cu<sub>10</sub>Zn<sub>2</sub>Sb<sub>4</sub>S<sub>13</sub> thermoelectric as a model material. Three simulations, 1x1x1 cell with plane wave (PW) basis, 1x1x1 cell with atomic orbital (AO) basis, and 2x2x2 cell with AO basis, are performed at 300 K to investigate the effect. Various structural and dynamic properties are extracted from three simulations, such as lattice parameters, partial and total vibrational density of states, phonon dispersion, heat capacity, and EXAFS spectra. Comparison of these properties shows good agreement among these three simulations. We also investigate the 2x2x2 cell, which allows us to access the smaller Q range, where longitudinal and transverse sound/acoustic modes with linear dispersion can be identified. Sound velocities, bulk modulus and shear modulus can be extracted, showing good agreement with experimental data. Two low-energy quasi-localized vibrational modes can be observed from the coherent velocity correlation, which could scatter heat-carrying acoustic modes by reducing their lifetime instead of reducing their speeds, leading to a small thermal diffusivity.

With respect to LiPON electrolyte, we implemented advance DFTB method to investigate the structural and ionic conduction of Li<sub>3</sub>PO<sub>4</sub> and LiPON. New parameters for Li-P-O-N

interactions are applied to generate crystalline (c-) and amorphous (a-) Li<sub>3</sub>PO<sub>4</sub> and LiPON. Both apical N (N<sub>a</sub>) and doubly-bridge N (N<sub>d</sub>) can be observed in a-LiPON, but only in c-LiPON at higher temperature, whereas no evidence of triply-bridge N (N<sub>t</sub>) exists. Bond order calculation suggests that N<sub>d</sub> incorporated with P in the form of P=N<sub>d</sub>-P, and Li atoms have larger bond order with N<sub>a</sub> than with O or N<sub>d</sub>. Moreover, we examined the self-diffusivity of different atomic groups. With the addition of N, P and O atoms become more mobile in c-LiPON. The Li self-diffusivity of a-Li<sub>3</sub>PO<sub>4</sub> reveals good agreement with experimental data. Jump length and residence time of Li diffusion from all four structures have been investigated as well. From the ionic conductivity calculation, we show that c-LiPON has one order magnitude higher ionic conductivity than c-Li<sub>3</sub>PO<sub>4</sub>, while a-Li<sub>3</sub>PO<sub>4</sub> shared similar ionic conductivity with a-LiPON, which we ascribe to the highly disorder of both amorphous phases. This work provides insights of the amorphous structure of a-LiPON and the effect of N doping.

In order to understand the origin of electrochemical stability between LiPON electrolyte and Li metal, we implement DFTB method to generate a LiPON/Li interface supercell and perform MD simulation on the supercell. From our simulation, only 3 layers of metallic Li involve the reaction with LiPON. Beyond the 3 surface layers, the middle of metallic Li atoms maintain as bcc structure based on our average structure analysis. It's notable that 3 layers of disordered metallic Li are involving the reaction with LiPON on both sides, while the middle layers are maintained as bcc structure. The reaction at the interface occur within 10 ps, and no decomposition of LiPON, or formation of Li<sub>2</sub>O, Li<sub>3</sub>N and Li<sub>3</sub>P can be observed. Li charge distribution is investigated, showing the thickness of interface is about 6 Å. The charges of P, O and N do not reveal difference between bulk and interface. Projected density of states of different layers and Li atoms are also

included. Metallic behavior of the interface can be identified by the numbers of electronic states at Fermi energy level.

**BIBLIOGRAPHY** 

#### **BIBLIOGRAPHY**

- 1. Petroleum, B., BP Statistical Review of World Energy Report. BP: London, UK 2019.
- 2. Energy, G., Global Energy & CO2 Status Report. *International Energy Agency: Paris, France* **2019**.
- 3. Change, I. C., The Physical Science Basis Cambridge, United Kingdom and New York, NY. *USA: Cambridge University Press* **2007**, 2007, 748-845.
- 4. Jenkinson, D. S.; Adams, D.; Wild, A., Model estimates of CO2 emissions from soil in response to global warming. *Nature* **1991**, *351* (6324), 304.
- 5. Cherubini, F.; Peters, G. P.; Berntsen, T.; Strømman, A. H.; Hertwich, E., CO2 emissions from biomass combustion for bioenergy: atmospheric decay and contribution to global warming. *Gcb Bioenergy* **2011**, *3* (5), 413-426.
- 6. Rosa, L. P.; Ribeiro, S. K., The present, past, and future contributions to global warming of CO2 emissions from fuels. *Climatic Change* **2001**, *48* (2-3), 289-307.
- 7. Dessler, A. E.; Parson, E. A., *The science and politics of global climate change: A guide to the debate.* Cambridge University Press: 2019.
- 8. Forman, C.; Muritala, I. K.; Pardemann, R.; Meyer, B., Estimating the global waste heat potential. *Renewable and Sustainable Energy Reviews* **2016**, *57*, 1568-1579.
- 9. Elsheikh, M. H.; Shnawah, D. A.; Sabri, M. F. M.; Said, S. B. M.; Hassan, M. H.; Bashir, M. B. A.; Mohamad, M., A review on thermoelectric renewable energy: Principle parameters that affect their performance. *Renewable and sustainable energy reviews* **2014**, *30*, 337-355.
- 10. Thackeray, M. M.; Wolverton, C.; Isaacs, E. D., Electrical energy storage for transportation—approaching the limits of, and going beyond, lithium-ion batteries. *Energy & Environmental Science* **2012**, *5* (7), 7854-7863.
- 11. Snyder, G. J.; Toberer, E. S., Complex thermoelectric materials. In *materials for sustainable energy: a collection of peer-reviewed research and review articles from Nature Publishing Group*, World Scientific: 2011; pp 101-110.
- 12. Chen, G.; Dresselhaus, M.; Dresselhaus, G.; Fleurial, J.-P.; Caillat, T., Recent developments in thermoelectric materials. *International Materials Reviews* **2003**, *48* (1), 45-66.
- 13. Tritt, T. M.; Subramanian, M., Thermoelectric materials, phenomena, and applications: a bird's eye view. *MRS bulletin* **2006**, *31* (3), 188-198.
- 14. Alam, H.; Ramakrishna, S., A review on the enhancement of figure of merit from bulk to nano-thermoelectric materials. *Nano energy* **2013**, *2* (2), 190-212.

- 15. Price, S., The Peltier Effect and Thermoelectric Cooling. WWW-dokumentti. Saatavilla: <a href="http://ffden-2">http://ffden-2</a>. phys. uaf. edu/212\_spring2007. web. dir/sedona\_price/phys\_212\_webproj\_peltier. html [viitattu 20.5. 2017] **2007**.
- 16. Seebeck, T., Magnetische polarisation der metalle und erze durck temperatur-differenz, Abh. K. *Akad. Wiss. Berlin* **1823**, *265*, 1823.
- 17. Riffat, S. B.; Ma, X., Thermoelectrics: a review of present and potential applications. *Applied thermal engineering* **2003**, *23* (8), 913-935.
- 18. Nolas, G.; Morelli, D.; Tritt, T. M., Skutterudites: A phonon-glass-electron crystal approach to advanced thermoelectric energy conversion applications. *Annual Review of Materials Science* **1999**, *29* (1), 89-116.
- 19. Zhao, L.-D.; Lo, S.-H.; Zhang, Y.; Sun, H.; Tan, G.; Uher, C.; Wolverton, C.; Dravid, V. P.; Kanatzidis, M. G., Ultralow thermal conductivity and high thermoelectric figure of merit in SnSe crystals. *Nature* **2014**, *508* (7496), 373.
- 20. Heremans, J. P.; Jovovic, V.; Toberer, E. S.; Saramat, A.; Kurosaki, K.; Charoenphakdee, A.; Yamanaka, S.; Snyder, G. J., Enhancement of thermoelectric efficiency in PbTe by distortion of the electronic density of states. *Science* **2008**, *321* (5888), 554-557.
- 21. Slack, G. A.; Rowe, D., CRC handbook of thermoelectrics. CRC press Boca Raton, FL: 1995.
- 22. Yang, J.; Stabler, F. R., Automotive Applications of Thermoelectric Materials. *Journal of electronic materials* **2009**, *38* (7).
- 23. Matsubara, K. In *Development of a high efficient thermoelectric stack for a waste exhaust heat recovery of vehicles*, Twenty-First International Conference on Thermoelectrics, 2002. Proceedings ICT'02., IEEE: 2002; pp 418-423.
- 24. Fleurial, J.-P., Thermoelectric power generation materials: Technology and application opportunities. *Jom* **2009**, *61* (4), 79-85.
- 25. Hendricks, T. J., Integrated thermoelectric—thermal system resistance optimization to maximize power output in thermoelectric energy recovery systems. *MRS Online Proceedings Library Archive* **2014**, *1642*.
- 26. Tritt, T. M.; Böttner, H.; Chen, L., Thermoelectrics: Direct solar thermal energy conversion. *MRS bulletin* **2008**, *33* (4), 366-368.
- 27. Min, G.; Rowe, D., Experimental evaluation of prototype thermoelectric domestic-refrigerators. *Applied Energy* **2006**, *83* (2), 133-152.
- 28. Vián, J.; Astrain, D., Development of a thermoelectric refrigerator with two-phase thermosyphons and capillary lift. *Applied Thermal Engineering* **2009**, *29* (10), 1935-1940.

- 29. Dai, Y.; Wang, R.; Ni, L., Experimental investigation and analysis on a thermoelectric refrigerator driven by solar cells. *Solar energy materials and solar cells* **2003**, *77* (4), 377-391.
- 30. Phelan, P. E.; Chiriac, V. A.; Lee, T.-Y., Current and future miniature refrigeration cooling technologies for high power microelectronics. *IEEE Transactions on Components and Packaging Technologies* **2002**, *25* (3), 356-365.
- 31. Putra, N.; Sukyono, W.; Johansen, D.; Iskandar, F. N., The characterization of a cascade thermoelectric cooler in a cryosurgery device. *Cryogenics* **2010**, *50* (11-12), 759-764.
- 32. Choi, H.-S.; Yun, S.; Whang, K.-i., Development of a temperature-controlled car-seat system utilizing thermoelectric device. *Applied Thermal Engineering* **2007**, *27* (17-18), 2841-2849.
- 33. Riffat, S.; Qiu, G., Comparative investigation of thermoelectric air-conditioners versus vapour compression and absorption air-conditioners. *Applied Thermal Engineering* **2004**, *24* (14-15), 1979-1993.
- 34. Lu, X.; Morelli, D. T.; Xia, Y.; Ozolins, V., Increasing the Thermoelectric Figure of Merit of Tetrahedrites by Co-Doping with Nickel and Zinc. *Chemistry of Materials* **2015**, 27 (2), 408-413.
- 35. Lu, X.; Morelli, D. T.; Xia, Y.; Zhou, F.; Ozolins, V.; Chi, H.; Zhou, X.; Uher, C., High performance thermoelectricity in earth abundant compounds based on natural mineral tetrahedrites. *Advanced Energy Materials* **2013**, *3* (3), 342-348.
- 36. Heo, J.; Laurita, G.; Muir, S.; Subramanian, M. A.; Keszler, D. A., Enhanced Thermoelectric Performance of Synthetic Tetrahedrites. *Chemistry of Materials* **2014**, *26* (6), 2047-2051.
- 37. Momma, K.; Izumi, F., VESTA 3 for three-dimensional visualization of crystal, volumetric and morphology data. *Journal of Applied Crystallography* **2011**, *44* (6), 1272-1276.
- 38. Pfitzner, A.; Evain, M.; Petricek, V., Cu12Sb4S13: A temperature-dependent structure investigation. *Acta Crystallographica Section B: Structural Science* **1997**, *53* (3), 337-345.
- 39. Lai, W.; Wang, Y.; Morelli, D. T.; Lu, X., From bonding asymmetry to anharmonic rattling in Cu12Sb4S13 tetrahedrites: When lone-pair electrons are not so lonely. *Advanced Functional Materials* **2015**, 25 (24), 3648-3657.
- 40. Suekuni, K.; Tomizawa, Y.; Ozaki, T.; Koyano, M., Systematic study of electronic and magnetic properties for Cu12–x TM x Sb4S13 (TM= Mn, Fe, Co, Ni, and Zn) tetrahedrite. *Journal of Applied Physics* **2014**, *115* (14), 143702.
- 41. Bouyrie, Y.; Candolfi, C.; Ohorodniichuk, V.; Malaman, B.; Dauscher, A.; Tobola, J.; Lenoir, B., Crystal structure, electronic band structure and high-temperature thermoelectric properties of Te-substituted tetrahedrites Cu 12 Sb 4– x Te x S 13 ( $0.5 \le x \le 2.0$ ). *Journal of Materials Chemistry C* **2015**, *3* (40), 10476-10487.

- 42. Tablero, C., Electronic and Optical Property Analysis of the Cu-Sb-S Tetrahedrites for High-Efficiency Absorption Devices. *Journal of Physical Chemistry C* **2014**, *118* (28), 15122-15127.
- 43. Tippireddy, S.; Chetty, R.; Naik, M. H.; Jain, M.; Chattopadhyay, K.; Mallik, R. C., Electronic and thermoelectric properties of transition metal substituted tetrahedrites. *The Journal of Physical Chemistry C* **2018**, *122* (16), 8735-8749.
- 44. Suekuni, K.; Kim, F.; Takabatake, T., Tunable electronic properties and low thermal conductivity in synthetic colusites Cu26-x Zn x V2M6S32 ( $x \le 4$ , M=Ge, Sn). *Journal of Applied Physics* **2014**, *116* (6), 063706.
- 45. Suekuni, K.; Tsuruta, K.; Kunii, M.; Nishiate, H.; Nishibori, E.; Maki, S.; Ohta, M.; Yamamoto, A.; Koyano, M., High-performance thermoelectric mineral Cu12– x Ni x Sb4S13 tetrahedrite. *Journal of Applied Physics* **2013**, *113* (4), 043712.
- 46. Suekuni, K.; Tsuruta, K.; Ariga, T.; Koyano, M., Thermoelectric properties of mineral tetrahedrites Cu10Tr2Sb4S13 with low thermal conductivity. *Applied Physics Express* **2012**, *5* (5), 051201.
- 47. Lu, X.; Morelli, D., The effect of Te substitution for Sb on thermoelectric properties of tetrahedrite. *Journal of Electronic Materials* **2014**, *43* (6), 1983-1987.
- 48. Bouyrie, Y.; Candolfi, C.; Dauscher, A.; Malaman, B.; Lenoir, B., Exsolution Process as a Route toward Extremely Low Thermal Conductivity in Cu12Sb4-x Te x S13 Tetrahedrites. *Chemistry of Materials* **2015**, *27* (24), 8354-8361.
- 49. Kumar, D. P.; Chetty, R.; Femi, O.; Chattopadhyay, K.; Malar, P.; Mallik, R., Thermoelectric properties of Bi doped tetrahedrite. *Journal of Electronic Materials* **2017**, *46* (5), 2616-2622.
- 50. Chetty, R.; DS, P. K.; Rogl, G.; Rogl, P.; Bauer, E.; Michor, H.; Suwas, S.; Puchegger, S.; Giester, G.; Mallik, R. C., Thermoelectric properties of a Mn substituted synthetic tetrahedrite. *Physical Chemistry Chemical Physics* **2015**, *17* (3), 1716-1727.
- 51. Weller, D. P.; Morelli, D. T., Rapid synthesis of zinc and nickel co-doped tetrahedrite thermoelectrics by reactive spark plasma sintering and mechanical alloying. *J. Alloys Compd.* **2017**, 710, 794-799.
- 52. Lu, X.; Morelli, D. T., Rapid synthesis of high-performance thermoelectric materials directly from natural mineral tetrahedrite. *Mrs Communications* **2013**, *3* (3), 129-133.
- 53. Barbier, T.; Rollin-Martinet, S.; Lemoine, P.; Gascoin, F.; Kaltzoglou, A.; Vaqueiro, P.; Powell, A. V.; Guilmeau, E., Thermoelectric Materials: A New Rapid Synthesis Process for Nontoxic and High-Performance Tetrahedrite Compounds. *Journal of the American Ceramic Society* **2016**, *99* (1), 51-56.

- 54. Meinel, A. B.; Meinel, M. P., Applied solar energy: an introduction. *NASA STI/Recon Technical Report A* **1977**, *77*.
- 55. Boyle, G., Renewable energy. *Renewable Energy, by Edited by Godfrey Boyle, pp. 456.* Oxford University Press, May 2004. ISBN-10: 0199261784. ISBN-13: 9780199261789 **2004**, 456.
- 56. Kenisarin, M.; Mahkamov, K., Solar energy storage using phase change materials. *Renewable and sustainable energy reviews* **2007**, *11* (9), 1913-1965.
- 57. Zhao, H.; Wu, Q.; Hu, S.; Xu, H.; Rasmussen, C. N., Review of energy storage system for wind power integration support. *Applied energy* **2015**, *137*, 545-553.
- 58. Korpaas, M.; Holen, A. T.; Hildrum, R., Operation and sizing of energy storage for wind power plants in a market system. *International Journal of Electrical Power & Energy Systems* **2003**, 25 (8), 599-606.
- 59. Association, E. W. E., *The economics of wind energy*. EWEA: 2009.
- 60. Chum, H.; Faaij, A.; Moreira, J.; Junginger, H., Bioenergy. **2011**.
- 61. Bioenergy, I., Bioenergy–a sustainable and reliable energy source. *International Energy Agency Bioenergy, Paris, France* **2009**.
- 62. Rittmann, B. E., Opportunities for renewable bioenergy using microorganisms. *Biotechnology and bioengineering* **2008**, *100* (2), 203-212.
- 63. Goodenough, J. B.; Kim, Y., Challenges for rechargeable Li batteries. *Chemistry of materials* **2009**, 22 (3), 587-603.
- 64. Zaghib, K.; Guerfi, A.; Hovington, P.; Vijh, A.; Trudeau, M.; Mauger, A.; Goodenough, J. B.; Julien, C., Review and analysis of nanostructured olivine-based lithium recheargeable batteries: Status and trends. *Journal of Power Sources* **2013**, *232*, 357-369.
- 65. Lu, Z.; Beaulieu, L.; Donaberger, R.; Thomas, C.; Dahn, J., Synthesis, Structure, and Electrochemical Behavior of Li [Ni x Li1/3- 2x/3Mn2/3- x/3] O 2. *Journal of The Electrochemical Society* **2002**, *149* (6), A778-A791.
- 66. Bruce, P. G.; Freunberger, S. A.; Hardwick, L. J.; Tarascon, J.-M., Li–O 2 and Li–S batteries with high energy storage. *Nature materials* **2012**, *11* (1), 19.
- 67. Xu, J.; Dou, S.; Liu, H.; Dai, L., Cathode materials for next generation lithium ion batteries. *Nano Energy* **2013**, 2 (4), 439-442.
- 68. Taracson, J.; Armand, M., Issues and challenges facing lithium ion batteries. *nature* **2001**, *414*, 359-367.
- 69. Sawai, K.; Iwakoshi, Y.; Ohzuku, T., Carbon materials for lithium-ion (shuttlecock) cells. *Solid State Ionics* **1994**, *69* (3-4), 273-283.

- 70. Sandhya, C.; John, B.; Gouri, C., Lithium titanate as anode material for lithium-ion cells: a review. *Ionics* **2014**, *20* (5), 601-620.
- 71. Goward, G.; Taylor, N.; Souza, D.; Nazar, L., The true crystal structure of Li17M4 (M=Ge, Sn, Pb)–revised from Li22M5. *Journal of alloys and compounds* **2001**, *329* (1-2), 82-91.
- 72. Kamaya, N.; Homma, K.; Yamakawa, Y.; Hirayama, M.; Kanno, R.; Yonemura, M.; Kamiyama, T.; Kato, Y.; Hama, S.; Kawamoto, K., A lithium superionic conductor. *Nature materials* **2011**, *10* (9), 682.
- 73. Thangadurai, V.; Narayanan, S.; Pinzaru, D., Garnet-type solid-state fast Li ion conductors for Li batteries: critical review. *Chemical Society Reviews* **2014**, *43* (13), 4714-4727.
- 74. Gwon, H.; Hong, J.; Kim, H.; Seo, D.-H.; Jeon, S.; Kang, K., Recent progress on flexible lithium rechargeable batteries. *Energy & Environmental Science* **2014**, *7* (2), 538-551.
- 75. Zhang, S.; Ervin, M.; Xu, K.; Jow, T., Microporous poly (acrylonitrile-methyl methacrylate) membrane as a separator of rechargeable lithium battery. *Electrochimica Acta* **2004**, *49* (20), 3339-3345.
- 76. QIU, W.-l.; YANG, Q.-h.; MA, X.-h.; FU, Y.-b.; ZONG, X.-f., Research on PEO-based dry solid polymer electrolytes for rechargeable lithium batteries [J]. *Chinese Journal of Power Sources* **2004**, 7.
- 77. Morata-Orrantia, A.; García-Martín, S.; Morán, E.; Alario-Franco, M. Á., A New La2/3Li x Ti1-x Al x O3 Solid Solution: Structure, Microstructure, and Li+ Conductivity. *Chemistry of materials* **2002**, *14* (7), 2871-2875.
- 78. Bates, J.; Dudney, N.; Gruzalski, G.; Zuhr, R.; Choudhury, A.; Luck, C.; Robertson, J., Electrical properties of amorphous lithium electrolyte thin films. *Solid state ionics* **1992**, *53*, 647-654.
- 79. Wang, B.; Chakoumakos, B.; Sales, B.; Kwak, B.; Bates, J., Synthesis, crystal structure, and ionic conductivity of a polycrystalline lithium phosphorus oxynitride with the  $\gamma$ -Li3PO4 structure. *Journal of Solid State Chemistry* **1995**, *115* (2), 313-323.
- 80. Schnick, W.; Luecke, J., Synthesis and crystal structure of lithium phosphorus nitride Li7PN4: the first compound containing isolated PN4-tetrahedra. *Journal of Solid State Chemistry* **1990,** 87 (1), 101-106.
- 81. Daidouh, A.; Veiga, M.; Pico, C.; Martinez-Ripoll, M., A new polymorph of Li4P2O7. *Acta Crystallographica Section C: Crystal Structure Communications* **1997**, *53* (2), 167-169.
- 82. Hermansen, C.; Mauro, J. C.; Yue, Y., A model for phosphate glass topology considering the modifying ion sub-network. *The Journal of Chemical Physics* **2014**, *140* (15), 154501.
- 83. Du, Y. A.; Holzwarth, N., First-principles study of LiPON and related solid electrolytes. *Physical Review B* **2010**, *81* (18), 184106.

- 84. Bunker, B. C.; Tallant, D. R.; Balfe, C. A.; Kirkpatrick, R. J.; Turner, G. L.; Reidmeyer, M. R., Structure of phosphorus oxynitride glasses. *Journal of the American Ceramic Society* **1987**, 70 (9), 675-681.
- 85. Marchand, R.; L'Haridon, P.; Laurent, Y., Etude cristallochimique de LiPN2: Une structure derivée de la cristobalite. *Journal of Solid State Chemistry* **1982**, *43* (2), 126-130.
- 86. Horstmann, S.; Irran, E.; Schnick, W., Phosphor (V)-nitrid α-P3N5: Synthese ausgehend von Tetraaminophosphoniumiodid und Kristallstrukturaufklärung mittels Synchrotron-Pulver-Röntgenbeugung. *Zeitschrift für anorganische und allgemeine Chemie* **1998**, *624* (4), 620-628.
- 87. West, W.; Whitacre, J.; Lim, J., Chemical stability enhancement of lithium conducting solid electrolyte plates using sputtered LiPON thin films. *Journal of power sources* **2004**, *126* (1-2), 134-138.
- 88. Sagane, F.; Ikeda, K.-i.; Okita, K.; Sano, H.; Sakaebe, H.; Iriyama, Y., Effects of current densities on the lithium plating morphology at a lithium phosphorus oxynitride glass electrolyte/copper thin film interface. *Journal of Power Sources* **2013**, *233*, 34-42.
- 89. Albertus, P.; Babinec, S.; Litzelman, S.; Newman, A., Status and challenges in enabling the lithium metal electrode for high-energy and low-cost rechargeable batteries. *Nature Energy* **2018**, *3* (1), 16.
- 90. Bates, J.; Lubben, D.; Dudney, N.; Hart, F., 5 Volt Plateau in LiMn2 O 4 Thin Films. *Journal of the electrochemical society* **1995**, *142* (9), L149-L151.
- 91. Yu, X.; Bates, J.; Jellison, G.; Hart, F., A stable thin-film lithium electrolyte: lithium phosphorus oxynitride. *Journal of the electrochemical society* **1997**, *144* (2), 524-532.
- 92. Dudney, N. J., Addition of a thin-film inorganic solid electrolyte (Lipon) as a protective film in lithium batteries with a liquid electrolyte. *Journal of Power Sources* **2000**, 89 (2), 176-179.
- 93. Hohenberg, P.; Kohn, W., Inhomogeneous electron gas. *Physical review* **1964**, *136* (3B), B864.
- 94. Kohn, W.; Sham, L. J., Self-consistent equations including exchange and correlation effects. *Physical review* **1965**, *140* (4A), A1133.
- 95. Klenk, M. J.; Lai, W., Finite-size effects on the molecular dynamics simulation of fast-ion conductors: A case study of lithium garnet oxide Li7La3Zr2O12. *Solid State Ionics* **2016**, 289, 143-149.
- 96. Sarmiento-Perez, R.; Botti, S.; Marques, M. A., Optimized exchange and correlation semilocal functional for the calculation of energies of formation. *Journal of chemical theory and computation* **2015**, *11* (8), 3844-3850.
- 97. Christopher, J. C., Essentials of Computational Chemistry. *Theories and Models* **2002**.

- 98. Bylander, D.; Kleinman, L., Good semiconductor band gaps with a modified local-density approximation. *Physical Review B* **1990**, *41* (11), 7868.
- 99. Painter, G., Improved correlation corrections to the local-spin-density approximation. *Physical Review B* **1981**, *24* (8), 4264.
- 100. Perdew, J. P.; Burke, K.; Ernzerhof, M., Generalized gradient approximation made simple. *Physical review letters* **1996**, *77* (18), 3865.
- 101. Stephens, P. J.; Devlin, F.; Chabalowski, C.; Frisch, M. J., Ab initio calculation of vibrational absorption and circular dichroism spectra using density functional force fields. *The Journal of physical chemistry* **1994**, *98* (45), 11623-11627.
- 102. Pribram-Jones, A.; Gross, D. A.; Burke, K., Dft: A theory full of holes? *Annual review of physical chemistry* **2015**, *66*, 283-304.
- 103. Zeng, Q.; Yu, A.; Lu, G., Multiscale modeling and simulation of polymer nanocomposites. *Progress in polymer science* **2008**, *33* (2), 191-269.
- 104. Perdew, J. P.; Ziesche, P.; Eschrig, H., Electronic structure of solids' 91. Akademie Verlag, Berlin: 1991.
- 105. Fulde, P., *Electron correlations in molecules and solids*. Springer Science & Business Media: 2012; Vol. 100.
- 106. Dai, J. In *Investigation of Li Ion Dynamics in Garnet Oxide Li6. 5La3Zr1. 5Ta0. 5O12 Using Molecular Dynamics Simulation*, Meeting Abstracts, The Electrochemical Society: 2019; pp 174-174.
- 107. Klenk, M. J.; Boeberitz, S. E.; Dai, J.; Jalarvo, N. H.; Peterson, V. K.; Lai, W., Lithium self-diffusion in a model lithium garnet oxide Li 5 La 3 Ta 2 O 12: A combined quasi-elastic neutron scattering and molecular dynamics study. *Solid State Ionics* **2017**, *312*, 1-7.
- 108. Besenbacher, F.; Chorkendorff, I.; Clausen, B.; Hammer, B.; Molenbroek, A.; Nørskov, J. K.; Stensgaard, I., Design of a surface alloy catalyst for steam reforming. *Science* **1998**, *279* (5358), 1913-1915.
- 109. Kolmogorov, A.; Shah, S.; Margine, E.; Bialon, A.; Hammerschmidt, T.; Drautz, R., New superconducting and semiconducting Fe-B compounds predicted with an ab initio evolutionary search. *Physical review letters* **2010**, *105* (21), 217003.
- 110. Blouin, N.; Michaud, A.; Gendron, D.; Wakim, S.; Blair, E.; Neagu-Plesu, R.; Belletete, M.; Durocher, G.; Tao, Y.; Leclerc, M., Toward a rational design of poly (2, 7-carbazole) derivatives for solar cells. *Journal of the American Chemical Society* **2008**, *130* (2), 732-742.
- 111. Jain, A.; Shin, Y.; Persson, K. A., Computational predictions of energy materials using density functional theory. *Nature Reviews Materials* **2016**, *I* (1), 15004.

- 112. Cohen, A. J.; Mori-Sánchez, P.; Yang, W., Challenges for density functional theory. *Chemical reviews* **2011**, *112* (1), 289-320.
- 113. Elstner, M.; Porezag, D.; Jungnickel, G.; Elsner, J.; Haugk, M.; Frauenheim, T.; Suhai, S.; Seifert, G., Self-consistent-charge density-functional tight-binding method for simulations of complex materials properties. *Physical Review B* **1998**, *58* (11), 7260.
- 114. Frauenheim, T.; Seifert, G.; Elstner, M.; Niehaus, T.; Köhler, C.; Amkreutz, M.; Sternberg, M.; Hajnal, Z.; Di Carlo, A.; Suhai, S., Atomistic simulations of complex materials: ground-state and excited-state properties. *Journal of Physics: Condensed Matter* **2002**, *14* (11), 3015.
- 115. Gaus, M.; Cui, Q.; Elstner, M., DFTB3: extension of the self-consistent-charge density-functional tight-binding method (SCC-DFTB). *Journal of chemical theory and computation* **2011**, 7 (4), 931-948.
- 116. Eschrig, H.; Bergert, I., An optimized LCAO version for band structure calculations application to copper. *physica status solidi* (b) **1978,** 90 (2), 621-628.
- 117. Porezag, D.; Frauenheim, T.; Köhler, T.; Seifert, G.; Kaschner, R., Construction of tight-binding-like potentials on the basis of density-functional theory: Application to carbon. *Physical Review B* **1995**, *51* (19), 12947.
- 118. Foulkes, W. M. C.; Haydock, R., Tight-binding models and density-functional theory. *Physical review B* **1989**, *39* (17), 12520.
- 119. Frauenheim, T.; Seifert, G.; Elsterner, M.; Hajnal, Z.; Jungnickel, G.; Porezag, D.; Suhai, S.; Scholz, R., A self-consistent charge density-functional based tight-binding method for predictive materials simulations in physics, chemistry and biology. *physica status solidi* (b) **2000**, 217 (1), 41-62.
- 120. Seifert, G.; Porezag, D.; Frauenheim, T., Calculations of molecules, clusters, and solids with a simplified LCAO-DFT-LDA scheme. *International journal of quantum chemistry* **1996**, 58 (2), 185-192.
- 121. Allen, M. P.; Tildesley, D. J., *Computer simulation of liquids*. Oxford university press: 2017.
- 122. LeSar, R., *Introduction to computational materials science: fundamentals to applications*. Cambridge University Press: 2013.
- 123. Tee, L. S.; Gotoh, S.; Stewart, W. E., Molecular parameters for normal fluids. Lennard-Jones 12-6 Potential. *Industrial & Engineering Chemistry Fundamentals* **1966**, *5* (3), 356-363.
- 124. Wood, W.; Parker, F., Monte Carlo Equation of State of Molecules Interacting with the Lennard-Jones Potential. I. A Supercritical Isotherm at about Twice the Critical Temperature. *The Journal of Chemical Physics* **1957**, *27* (3), 720-733.

- 125. Haftel, M. I., Surface reconstruction of platinum and gold and the embedded-atom model. *Physical Review B* **1993**, *48* (4), 2611.
- 126. Stillinger, F. H.; Weber, T. A., Computer simulation of local order in condensed phases of silicon. *Physical review B* **1985**, *31* (8), 5262.
- 127. Carmesin, I.; Kremer, K., The bond fluctuation method: a new effective algorithm for the dynamics of polymers in all spatial dimensions. *Macromolecules* **1988**, *21* (9), 2819-2823.
- 128. Van Gunsteren, W.; Berendsen, H., Algorithms for Brownian dynamics. *Molecular Physics* **1982**, *45* (3), 637-647.
- 129. Hoogerbrugge, P.; Koelman, J., Simulating microscopic hydrodynamic phenomena with dissipative particle dynamics. *EPL* (*Europhysics Letters*) **1992**, *19* (3), 155.
- 130. Chen, S.; Doolen, G. D., Lattice Boltzmann method for fluid flows. *Annual review of fluid mechanics* **1998**, *30* (1), 329-364.
- 131. Lee, B. P.; Douglas, J. F.; Glotzer, S. C., Filler-induced composition waves in phase-separating polymer blends. *Physical Review E* **1999**, *60* (5), 5812.
- 132. Altevogt, P.; Evers, O. A.; Fraaije, J. G.; Maurits, N. M.; van Vlimmeren, B. A., The MesoDyn project: software for mesoscale chemical engineering. *Journal of Molecular Structure: THEOCHEM* **1999**, *463* (1-2), 139-143.
- 133. Tucker III, C. L.; Liang, E., Stiffness predictions for unidirectional short-fiber composites: review and evaluation. *Composites science and technology* **1999**, *59* (5), 655-671.
- 134. Burnett, D. S., Finite element analysis: from concepts to applications. **1987**.
- 135. Guo, G.; Long, B.; Cheng, B.; Zhou, S.; Xu, P.; Cao, B., Three-dimensional thermal finite element modeling of lithium-ion battery in thermal abuse application. *Journal of Power Sources* **2010**, *195* (8), 2393-2398.
- 136. Nasonova, D. I.; Verchenko, V. Y.; Tsirlin, A. A.; Shevelkov, A. V., Low-Temperature structure and thermoelectric properties of pristine synthetic tetrahedrite Cu12Sb4S13. *Chemistry of Materials* **2016**, 28 (18), 6621-6627.
- 137. Tanaka, H. I.; Suekuni, K.; Umeo, K.; Nagasaki, T.; Sato, H.; Kutluk, G.; Nishibori, E.; Kasai, H.; Takabatake, T., Metal–Semiconductor Transition Concomitant with a Structural Transformation in Tetrahedrite Cu12Sb4S13. *Journal of the Physical Society of Japan* **2015**, *85* (1), 014703.
- 138. May, A. F.; Delaire, O.; Niedziela, J. L.; Lara-Curzio, E.; Susner, M. A.; Abernathy, D. L.; Kirkham, M.; McGuire, M. A., Structural phase transition and phonon instability in Cu 12 Sb 4 S 13. *Physical Review B* **2016**, *93* (6), 064104.

- 139. Vaqueiro, P.; Guélou, G.; Kaltzoglou, A.; Smith, R. I.; Barbier, T.; Guilmeau, E.; Powell, A. V., The influence of mobile copper ions on the glass-like thermal conductivity of copper-rich tetrahedrites. *Chemistry of Materials* **2017**, *29* (9), 4080-4090.
- 140. Bates, J.; Dudney, N.; Gruzalski, G.; Zuhr, R.; Choudhury, A.; Luck, C.; Robertson, J., Fabrication and characterization of amorphous lithium electrolyte thin films and rechargeable thin-film batteries. *Journal of power sources* **1993**, *43* (1-3), 103-110.
- 141. Di Benedetto, F.; Bernardini, G.; Cipriani, C.; Emiliani, C.; Gatteschi, D.; Romanelli, M., The distribution of Cu (II) and the magnetic properties of the synthetic analogue of tetrahedrite: Cu 12 Sb 4 S 13. *Physics and chemistry of minerals* **2005**, *32* (3), 155-164.
- 142. Kresse, G.; Hafner, J., Ab initio molecular dynamics for liquid metals. *Physical Review B* **1993,** 47 (1), 558.
- 143. Kresse, G.; Furthmüller, J., Efficiency of ab-initio total energy calculations for metals and semiconductors using a plane-wave basis set. *Computational materials science* **1996**, *6* (1), 15-50.
- 144. Kresse, G.; Furthmüller, J., Efficient iterative schemes for ab initio total-energy calculations using a plane-wave basis set. *Physical review B* **1996**, *54* (16), 11169.
- 145. Kresse, G.; Hafner, J., Ab initio molecular-dynamics simulation of the liquid-metal–amorphous-semiconductor transition in germanium. *Physical Review B* **1994**, *49* (20), 14251.
- 146. Pizzi, G.; Volja, D.; Kozinsky, B.; Fornari, M.; Marzari, N., BoltzWann: A code for the evaluation of thermoelectric and electronic transport properties with a maximally-localized Wannier functions basis. *Computer Physics Communications* **2014**, *185* (1), 422-429.
- 147. Pizzi, G.; Volja, D.; Kozinsky, B.; Fornari, M.; Marzari, N., An updated version of BoltzWann: A code for the evaluation of thermoelectric and electronic transport properties with a maximally-localized Wannier functions basis. *Computer Physics Communications* **2014**, *185* (8), 2311-2312.
- 148. Mostofi, A. A.; Yates, J. R.; Lee, Y.-S.; Souza, I.; Vanderbilt, D.; Marzari, N., wannier90: A tool for obtaining maximally-localised Wannier functions. *Computer physics communications* **2008**, *178* (9), 685-699.
- 149. Weller, D. P.; Stevens, D. L.; Kunkel, G. E.; Ochs, A. M.; Holder, C. F.; Morelli, D. T.; Anderson, M. E., Thermoelectric performance of tetrahedrite synthesized by a modified polyol process. *Chemistry of Materials* **2017**, *29* (4), 1656-1664.
- 150. Petříček, V.; Dušek, M.; Palatinus, L., Crystallographic computing system JANA2006: general features. *Zeitschrift für Kristallographie-Crystalline Materials* **2014**, 229 (5), 345-352.
- 151. Manz, T. A.; Sholl, D. S., Improved atoms-in-molecule charge partitioning functional for simultaneously reproducing the electrostatic potential and chemical states in periodic and nonperiodic materials. *Journal of chemical theory and computation* **2012**, *8* (8), 2844-2867.

- 152. Lai, W.; Wang, Y.; Morelli, D. T.; Lu, X., From Bonding Asymmetry to Anharmonic Rattling in Cu12Sb4S13Tetrahedrites: When Lone-Pair Electrons Are Not So Lonely. *Advanced Functional Materials* **2015**, *25* (24), 3648-3657.
- 153. Bouyrie, Y.; Candolfi, C.; Pailhes, S.; Koza, M.; Malaman, B.; Dauscher, A.; Tobola, J.; Boisron, O.; Saviot, L.; Lenoir, B., From crystal to glass-like thermal conductivity in crystalline minerals. *Physical Chemistry Chemical Physics* **2015**, *17* (30), 19751-19758.
- 154. Li, J.; Zhu, M.; Abernathy, D. L.; Ke, X.; Morelli, D. T.; Lai, W., First-principles studies of atomic dynamics in tetrahedrite thermoelectrics. *APL Materials* **2016**, *4* (10), 104811.
- 155. Bullett, D.; Dawson, W., Bonding relationships in some ternary and quarternary phosphide and tetrahedrite structures:(Ag6M4P12) M6', Cu12+ xSb4S13 and Cu14-xSb4S13, Ln6Ni6P17. *Journal of Physics C: Solid State Physics* **1986**, *19* (29), 5837.
- 156. Bullett, D. W., Applications of atomic-orbital methods to the structure and properties of complex transition-metal compounds. *Physics and Chemistry of Minerals* **1987**, *14* (6), 485-491.
- 157. Madsen, G. K.; Singh, D. J., BoltzTraP. A code for calculating band-structure dependent quantities. *Computer Physics Communications* **2006**, *175* (1), 67-71.
- 158. Ziman, J. M., *Principles of the Theory of Solids*. Cambridge university press: 1979.
- 159. Kresse, G.; Hafner, J., Ab initiomolecular dynamics for liquid metals. *Physical Review B* **1993,** 47 (1), 558-561.
- 160. Kresse, G.; Hafner, J., Ab initiomolecular-dynamics simulation of the liquid-metal–amorphous-semiconductor transition in germanium. *Physical Review B* **1994**, *49* (20), 14251-14269.
- 161. Kresse, G.; Joubert, D., From ultrasoft pseudopotentials to the projector augmented-wave method. *Physical Review B* **1999**, *59* (3), 1758.
- 162. Blöchl, P. E., Projector augmented-wave method. *Physical review B* **1994**, *50* (24), 17953.
- 163. Fernandez-Alonso, F.; Price, D. L., Neutron Scattering. Academic Press: 2013; Vol. 44.
- 164. Lu, X.; Morelli, D. T.; Xia, Y.; Zhou, F.; Ozolins, V.; Chi, H.; Zhou, X.; Uher, C., High Performance Thermoelectricity in Earth-Abundant Compounds Based on Natural Mineral Tetrahedrites. *Advanced Energy Materials* **2013**, *3* (3), 342-348.
- 165. Baumert, J.; Gutt, C.; Shpakov, V.; Tse, J.; Krisch, M.; Müller, M.; Requardt, H.; Klug, D.; Janssen, S.; Press, W., Lattice dynamics of methane and xenon hydrate: Observation of symmetry-avoided crossing by experiment and theory. *Physical Review B* **2003**, *68* (17), 174301.
- 166. Tse, J.; Li, Z.; Uehara, K., Phonon band structures and resonant scattering in Na8Si46 and Cs8Sn44 clathrates. *EPL* (*Europhysics Letters*) **2001**, *56* (2), 261.

- 167. Lara-Curzio, E.; May, A. F.; Delaire, O.; McGuire, M. A.; Lu, X.; Liu, C.-Y.; Case, E. D.; Morelli, D. T., Low-temperature heat capacity and localized vibrational modes in natural and synthetic tetrahedrites. *Journal of Applied Physics* **2014**, *115* (19), 193515.
- 168. Fan, X.; Case, E. D.; Lu, X.; Morelli, D. T., Room temperature mechanical properties of natural-mineral-based thermoelectrics. *J. Mater. Sci.* **2013**, *48* (21), 7540-7550.
- 169. Johnson, M. L.; Jeanloz, R., A Brillouin-zone model for compositional variation in tetrahedrite. *American Mineralogist* **1983**, *68* (1-2), 220-226.
- 170. Vaqueiro, P.; Guélou, G.; Kaltzoglou, A.; Smith, R. I.; Barbier, T.; Guilmeau, E.; Powell, A. V., The Influence of Mobile Copper Ions on the Glass-Like Thermal Conductivity of Copper-Rich Tetrahedrites. *Chemistry of Materials* **2017**, *29* (9), 4080-4090.
- 171. Makovicky, E.; Skinner, B. J., Studies of the sulfosalts of copper; VII, Crystal structures of the exsolution products Cu (sub 12.3) Sb 4 S 13 and Cu (sub 13.8) Sb 4 S 13 of unsubstituted synthetic tetrahedrite. *The Canadian Mineralogist* **1979**, *17* (3), 619-634.
- 172. Grimme, S.; Ehrlich, S.; Goerigk, L., Effect of the damping function in dispersion corrected density functional theory. *Journal of computational chemistry* **2011**, *32* (7), 1456-1465.
- 173. Tran, F.; Stelzl, J.; Blaha, P., Rungs 1 to 4 of DFT Jacob's ladder: Extensive test on the lattice constant, bulk modulus, and cohesive energy of solids. *The Journal of chemical physics* **2016**, *144* (20), 204120.
- 174. Williams, G.; Watts, D. C., Non-symmetrical dielectric relaxation behaviour arising from a simple empirical decay function. *Transactions of the Faraday society* **1970**, *66*, 80-85.
- 175. Singwi, K.; Sjölander, A., Diffusive motions in water and cold neutron scattering. *Physical Review* **1960**, *119* (3), 863.
- 176. Jobic, H.; Theodorou, D. N., Quasi-elastic neutron scattering and molecular dynamics simulation as complementary techniques for studying diffusion in zeolites. *Microporous and mesoporous materials* **2007**, *102* (1-3), 21-50.
- 177. Wang, Y.; Klenk, M.; Page, K.; Lai, W., Local Structure and Dynamics of Lithium Garnet Ionic Conductors: A Model Material Li5La3Ta2O12. *Chemistry of Materials* **2014**, *26* (19), 5613-5624.
- 178. Jónsson, H.; Mills, G.; Jacobsen, K. W., Nudged elastic band method for finding minimum energy paths of transitions. **1998**.
- 179. Henkelman, G.; Uberuaga, B. P.; Jónsson, H., A climbing image nudged elastic band method for finding saddle points and minimum energy paths. *The Journal of chemical physics* **2000**, *113* (22), 9901-9904.

- 180. Henkelman, G.; Jónsson, H., Improved tangent estimate in the nudged elastic band method for finding minimum energy paths and saddle points. *The Journal of chemical physics* **2000**, *113* (22), 9978-9985.
- 181. Palmer, D.; Conley, M., CrystalMaker. CrystalMaker Software, Bicester, England 2007.
- 182. Kohn, W.; Sham, L. J., SELF-CONSISTENT EQUATIONS INCLUDING EXCHANGE AND CORRELATION EFFECTS. *Phys. Rev.* **1965**, *140* (4A), 1133-&.
- 183. Tran, F.; Stelzl, J.; Blaha, P., Rungs 1 to 4 of DFT Jacob's ladder: Extensive test on the lattice constant, bulk modulus, and cohesive energy of solids. *J. Chem. Phys.* **2016**, *144* (20).
- 184. Spiekermann, G.; Wilke, M.; Jahn, S., Structural and dynamical properties of supercritical H2O-SiO2 fluids studied by ab initio molecular dynamics. *Chem. Geol.* **2016**, *426*, 85-94.
- 185. Miceli, G.; Hutter, J.; Pasquarello, A., Liquid Water through Density-Functional Molecular Dynamics: Plane-Wave vs Atomic-Orbital Basis Sets. *J. Chem. Theory Comput.* **2016**, *12* (8), 3456-3462.
- 186. Ulian, G.; Tosoni, S.; Valdre, G., Comparison between Gaussian-type orbitals and plane wave ab initio density functional theory modeling of layer silicates: Talc Mg3Si4O10(OH)(2) as model system. *J. Chem. Phys.* **2013**, *139* (20).
- 187. Suekuni, K.; Tsuruta, K.; Kunii, M.; Nishiate, H.; Nishibori, E.; Maki, S.; Ohta, M.; Yamamoto, A.; Koyano, M., High-performance thermoelectric mineral Cu12-xNixSb4S13 tetrahedrite. *J. Appl. Phys.* **2013**, *113* (4).
- 188. Lai, W.; Wang, Y.; Morelli, D. T.; Lu, X., From bonding asymmetry to anharmonic rattling: when lone-pair electrons are not so lonely. *Adv. Funct. Mater.* **2015**, *25* (24), 3648-3657.
- 189. Li, J. C.; Zhu, M. Z.; Abernathy, D. L.; Ke, X. L.; Morelli, D. T.; Lai, W., First-Principles Studies of Atomic Dynamics in Tetrahedrite Thermoelectrics. *APL Materials* **2016**, *4*, 104811.
- 190. Zhou, F.; Nielson, W.; Xia, Y.; Ozolins, V., Lattice Anharmonicity and Thermal Conductivity from Compressive Sensing of First-Principles Calculations. *Phys. Rev. Lett.* **2014**, *113* (18).
- 191. Suekuni, K.; Tomizawa, Y.; Ozaki, T.; Koyano, M., Systematic study of electronic and magnetic properties for Cu12-xTMxSb4S13 (TM=Mn, Fe, Co, Ni, and Zn) tetrahedrite. *J. Appl. Phys.* **2014**, *115* (14).
- 192. Lu, X.; Morelli, D. T.; Wang, Y.; Lai, W.; Xia, Y.; Ozolins, V., Phase Stability, Crystal Structure, and Thermoelectric Properties of Cu12Sb4S13-xSex Sex Solid Solutions. *Chem. Mater.* **2016**, *28* (6), 1781-1786.
- 193. Kresse, G.; Hafner, J., Abinitio molecular-dynamics for liquid-metals. *Phys. Rev. B* **1993**, 47 (1), 558-561.

- 194. Kresse, G.; Furthmuller, J., Efficiency of ab-initio total energy calculations for metals and semiconductors using a plane-wave basis set. *Comput. Mater. Sci.* **1996**, *6* (1), 15-50.
- 195. Kresse, G.; Furthmuller, J., Efficient iterative schemes for ab initio total-energy calculations using a plane-wave basis set. *Phys. Rev. B* **1996,** *54* (16), 11169-11186.
- 196. Kresse, G.; Hafner, J., Ab-initio molecular-dynamics simulation of the liquid-metal amorphous-semiconductor transition in Germanium. *Phys. Rev. B* **1994**, *49* (20), 14251-14269.
- 197. Kresse, G.; Joubert, D., From ultrasoft pseudopotentials to the projector augmented-wave method. *Phys. Rev. B* **1999**, *59* (3), 1758-1775.
- 198. Blochl, P. E., Projector augmented-wave method. *Phys. Rev. B* **1994**, *50* (24), 17953-17979.
- 199. VandeVondele, J.; Krack, M.; Mohamed, F.; Parrinello, M.; Chassaing, T.; Hutter, J., QUICKSTEP: Fast and accurate density functional calculations using a mixed Gaussian and plane waves approach. *Comput. Phys. Commun.* **2005**, *167* (2), 103-128.
- 200. Hutter, J.; Iannuzzi, M.; Schiffmann, F.; VandeVondele, J., CP2K: atomistic simulations of condensed matter systems. *Wiley Interdisciplinary Reviews-Computational Molecular Science* **2014**, *4* (1), 15-25.
- 201. Goedecker, S.; Teter, M.; Hutter, J., Separable dual-space Gaussian pseudopotentials. *Phys. Rev. B* **1996**, *54* (3), 1703-1710.
- 202. Krack, M., Pseudopotentials for H to Kr optimized for gradient-corrected exchange-correlation functionals. *Theor. Chem. Acc.* **2005**, *114* (1-3), 145-152.
- 203. VandeVondele, J.; Hutter, J., Gaussian basis sets for accurate calculations on molecular systems in gas and condensed phases. *J. Chem. Phys.* **2007**, *127* (11).
- 204. Perdew, J. P.; Burke, K.; Ernzerhof, M., Generalized gradient approximation made simple. *Phys. Rev. Lett.* **1996,** 77 (18), 3865-3868.
- 205. Perdew, J. P.; Burke, K.; Ernzerhof, M., Generalized gradient approximation made simple (vol 77, pg 3865, 1996). *Phys. Rev. Lett.* **1997,** 78 (7), 1396-1396.
- 206. Martyna, G. J.; Tobias, D. J.; Klein, M. L., CONSTANT-PRESSURE MOLECULAR-DYNAMICS ALGORITHMS. *J. Chem. Phys.* **1994**, *101* (5), 4177-4189.
- 207. Webb, S. M., SIXpack: a graphical user interface for XAS analysis using IFEFFIT. *Phys. Scr.* **2005**, *T115*, 1011-1014.
- 208. Ravel, B.; Newville, M., ATHENA, ARTEMIS, HEPHAESTUS: data analysis for X-ray absorption spectroscopy using IFEFFIT. *Journal of Synchrotron Radiation* **2005**, *12*, 537-541.
- 209. Johnson, N. E., X-Ray Powder Diffraction Data for Synthetic Varieties of Tetrahedrite. *Powder Diffr.* **1991**, *6* (1), 43-47.

- 210. Lara-Curzio, E.; May, A. F.; Delaire, O.; McGuire, M. A.; Lu, X.; Liu, C.-Y.; Case, E. D.; Morelli, D. T., Low-temperature heat capacity and localized vibrational modes in natural and synthetic tetrahedrites. *J. Appl. Phys.* **2014**, *115* (19).
- 211. Rehr, J. J.; Kas, J. J.; Vila, F. D.; Prange, M. P.; Jorissen, K., Parameter-free calculations of X-ray spectra with FEFF9. *Phys. Chem. Chem. Phys.* **2010**, *12* (21), 5503-5513.
- 212. Hansen, J. P.; McDonald, I. R., Theory of Simple Liquids. Elsevier Ltd: 2013.
- 213. Shintani, H.; Tanaka, H., Universal link between the boson peak and transverse phonons in glass. *Nat. Mater.* **2008**, *7* (11), 870-877.
- 214. Marchand, R., Nitrogen-containing phosphate glasses. *Journal of Non-Crystalline Solids* **1983,** *56* (1-3), 173-178.
- 215. Day, D. E., Structural role of nitrogen in phosphate glasses. *Journal of Non-Crystalline Solids* **1989**, *112* (1-3), 7-14.
- 216. Jacke, S.; Song, J.; Dimesso, L.; Brötz, J.; Becker, D.; Jaegermann, W., Temperature dependent phosphorous oxynitride growth for all-solid-state batteries. *Journal of Power Sources* **2011**, *196* (16), 6911-6914.
- 217. Fleutot, B.; Pecquenard, B.; Martinez, H.; Letellier, M.; Levasseur, A., Investigation of the local structure of LiPON thin films to better understand the role of nitrogen on their performance. *Solid State Ionics* **2011**, *186* (1), 29-36.
- 218. Wang, B.; Kwak, B.; Sales, B.; Bates, J., Ionic conductivities and structure of lithium phosphorus oxynitride glasses. *Journal of non-crystalline solids* **1995**, *183* (3), 297-306.
- 219. Lacivita, V.; Westover, A. S.; Kercher, A.; Phillip, N. D.; Yang, G.; Veith, G.; Ceder, G.; Dudney, N. J., Resolving the amorphous structure of lithium phosphorus oxynitride (Lipon). *Journal of the American Chemical Society* **2018**, *140* (35), 11029-11038.
- 220. Lacivita, V.; Artrith, N.; Ceder, G., Structural and Compositional Factors That Control the Li-Ion Conductivity in LiPON Electrolytes. *Chemistry of Materials* **2018**, *30* (20), 7077-7090.
- 221. Parr, R. G., Density functional theory of atoms and molecules. In *Horizons of Quantum Chemistry*, Springer: 1980; pp 5-15.
- 222. Sicolo, S.; Albe, K., First-principles calculations on structure and properties of amorphous Li5P4O8N3 (LiPON). *Journal of Power Sources* **2016**, *331*, 382-390.
- 223. Al-Qawasmeh, A.; Holzwarth, N., Li14P2O3N6 and Li7PN4: Computational study of two nitrogen rich crystalline LiPON electrolyte materials. *Journal of Power Sources* **2017**, *364*, 410-419.

- 224. Sicolo, S.; Fingerle, M.; Hausbrand, R.; Albe, K., Interfacial instability of amorphous LiPON against lithium: A combined density functional theory and spectroscopic study. *Journal of Power Sources* **2017**, *354*, 124-133.
- 225. Leung, K.; Pearse, A. J.; Talin, A. A.; Fuller, E. J.; Rubloff, G. W.; Modine, N. A., Kinetics Controlled Degradation Reactions at Crystalline LiPON/LixCoO2 and Crystalline LiPON/Li-Metal Interfaces. *ChemSusChem* **2018**, *11* (12), 1956-1969.
- 226. Seifert, G., Tight-binding density functional theory: an approximate Kohn– Sham DFT scheme. *The Journal of Physical Chemistry A* **2007**, *111* (26), 5609-5613.
- 227. Aradi, B.; Hourahine, B.; Frauenheim, T., DFTB+, a sparse matrix-based implementation of the DFTB method. *The Journal of Physical Chemistry A* **2007**, *111* (26), 5678-5684.
- 228. Van den Bossche, M.; Grönbeck, H.; Hammer, B., Tight-binding approximation-enhanced global optimization. *Journal of chemical theory and computation* **2018**, *14* (5), 2797-2807.
- 229. Cromie, S.; Elena, A.; Pashov, D.; Norman, S.; Forero-Martinez, N.; Smyth, M., Aten v1. 8 User Manual Last Updated Tuesday, 03 December 2013.
- 230. Becke, A. D.; Edgecombe, K. E., A simple measure of electron localization in atomic and molecular systems. *The Journal of chemical physics* **1990,** *92* (9), 5397-5403.
- 231. Coles, J.; Long, J., An ion-microprobe study of the self-diffusion of Li+ of lithium fluoride. *Philosophical Magazine* **1974**, 29 (3), 457-471.
- 232. Takai, S.; Yoshioka, K.; Iikura, H.; Matsubayashi, M.; Yao, T.; Esaka, T., Tracer diffusion coefficients of lithium ion in LiMn2O4 measured by neutron radiography. *Solid State Ionics* **2014**, 256, 93-96.
- 233. Jambon, A.; Semet, M. P., Lithium diffusion in silicate glasses of albite, orthoclase, and obsidian composition: an ion-microprobe determination. *Earth and Planetary Science Letters* **1978**, *37* (3), 445-450.
- 234. Anderson, O.; Stuart, D., Calculation of activation energy of ionic conductivity in silica glasses by classical methods. *Journal of the American Ceramic Society* **1954,** *37* (12), 573-580.
- 235. Kuwata, N.; Lu, X.; Miyazaki, T.; Iwai, Y.; Tanabe, T.; Kawamura, J., Lithium diffusion coefficient in amorphous lithium phosphate thin films measured by secondary ion mass spectroscopy with isotope exchange methods. *Solid State Ionics* **2016**, *294*, 59-66.
- 236. Li, W.; Ando, Y.; Minamitani, E.; Watanabe, S., Study of Li atom diffusion in amorphous Li3PO4 with neural network potential. *The Journal of chemical physics* **2017**, *147* (21), 214106.
- 237. Hansen, J. P.; McDonald, I. R., Theory of simple liquids. *Physics Today* **1988**, *41*, 89.

- 238. Dai, J.; Chen, Q.; Glossmann, T.; Lai, W., Comparison of interatomic potential models on the molecular dynamics simulation of fast-ion conductors: A case study of a Li garnet oxide Li7La3Zr2O12. *Computational Materials Science* **2019**, *162*, 333-339.
- 239. Dyre, J. C.; Christensen, T.; Olsen, N. B., Elastic models for the non-Arrhenius viscosity of glass-forming liquids. *Journal of non-crystalline solids* **2006**, *352* (42-49), 4635-4642.
- 240. Roh, N.-S.; Lee, S.-D.; Kwon, H.-S., Effects of deposition condition on the ionic conductivity and structure of amorphous lithium phosphorus oxynitrate thin film. *Scripta materialia* **1999**, *42* (1).
- 241. Schwöbel, A.; Hausbrand, R.; Jaegermann, W., Interface reactions between LiPON and lithium studied by in-situ X-ray photoemission. *Solid State Ionics* **2015**, *273*, 51-54.
- 242. Zhu, Y.; He, X.; Mo, Y., Origin of outstanding stability in the lithium solid electrolyte materials: insights from thermodynamic analyses based on first-principles calculations. *ACS applied materials & interfaces* **2015**, *7* (42), 23685-23693.
- 243. Hutter, J.; Iannuzzi, M.; Schiffmann, F.; VandeVondele, J., cp2k: atomistic simulations of condensed matter systems. *Wiley Interdisciplinary Reviews: Computational Molecular Science* **2014**, *4*(1), 15-25.
- 244. Miao, Y.; Hynan, P.; von Jouanne, A.; Yokochi, A., Current Li-ion battery technologies in electric vehicles and opportunities for advancements. *Energies* **2019**, *12* (6), 1074.
- 245. Hannan, M. A.; Hoque, M. M.; Hussain, A.; Yusof, Y.; Ker, P. J., State-of-the-art and energy management system of lithium-ion batteries in electric vehicle applications: Issues and recommendations. *Ieee Access* **2018**, *6*, 19362-19378.